UNIVERSITÀ DEGLI STUDI DI MILANO

Scuola di Dottorato in Fisica, Astrofisica e Fisica Applicata
Dipartimento di Fisica

Corso di Dottorato in Fisica, Astrofisica e Fisica Applicata
Ciclo XXVI

Wave energy flux and absorption of Electron Cyclotron Gaussian beams in tokamak plasmas

Settore Scientifico Disciplinare FIS/03

Supervisore: Dott.ssa Daniela FARINA

Coordinatore: Prof. Marco BERSANELLI

Tesi di Dottorato di:
Alberto MARIANI

Anno Accademico 2012-2013

Commission of the final examination:

Dott. Gerardo GIRUZZI, Commissariat à l'Energie Atomique, Cadarache
Prof. Giuseppe GORINI, Università degli Studi di Milano-Bicocca, Dip. di Fisica
Prof. Piero MARTIN, Università degli Studi di Padova, Dip. di Fisica e Astronomia
Dott. Massimiliano ROMÉ, Università degli Studi di Milano, Dip. di Fisica

Final examination:

Monday, February 17, 2014
Università degli Studi di Milano, Dipartimento di Fisica, Milano, Italy

Cover illustration:

Joint European Torus vessel equipped with the ITER-Like wall, with a plasma superimposed (Courtesy of European Fusion Development Agreement, www.efda.org)

MIUR subjects:

FIS/03 - Fisica della materia

PACS:

52.25.Os Emission, absorption, and scattering of electromagnetic radiation
52.35.Hr Electromagnetic waves (e.g., electron-cyclotron, Whistler, Bernstein, upper hybrid, lower hybrid)
52.50.Sw Plasma heating by microwaves; ECR, LH, collisional heating
52.55.Fa Tokamaks, spherical tokamaks
52.55.Wq Current drive; helicity injection

Contents

Introduction

0.1 Magnetic confinement nuclear fusion and the ITER project

If two light nuclei are put together overcoming the Coulomb repulsion between them, they fuse and during this reaction an amount of energy is released. This process is called "nuclear fusion". Amongst all the possible reactions (cf. Fig. 1 for some example), the one that has been chosen for the actual fusion experiments is the deuterium-tritium:

$$D + T \rightarrow \alpha(3.5\ \mathrm{MeV}) + n(14.1\ \mathrm{MeV})\ . \tag{1}$$

This reaction releases 17.6 MeV, in the form of kinetic energy of the reaction products, one α particle and a neutron.
To overcome the Coulomb force, the reacting particles have to collide with sufficient initial kinetic energy. The most promising way to supply this energy is to heat the deuterium-tritium mixture until the thermal energy is sufficient to produce the fusion reaction. This method is called "thermonuclear fusion". Unless the maximum of the reaction cross section is at about $60 - 70\ \mathrm{keV}$ (cf. Fig. 1) of centre-of-mass energy of the reagents, it is sufficient to reach the much lower energy of about $10\ \mathrm{keV}$ (corresponding to about 100 millions K), because the required reactions occur in the high energy tail of the Maxwellian velocity distribution. At this temperature the fuel is completely ionized, being in the neutral plasma state, in which the nuclei charge is globally neutralized by the electron charge.

In order to reach "ignition" (self-susteined fusion process) the product of the plasma density n and the energy confinement time τ_E must exceed a value that depends on the temperature, on the efficiency η of reconversion of a fraction of the fusion energy into thermal energy of the fuel and on the particular reaction. This relation is called "Lawson criterion" and takes the form:

$$n\tau_E \geq f(\eta, T)\ , \tag{2}$$

where f depends principally on η and T, but also on some parameters related to the specific fusion reaction. For the deuterium-tritium reaction, in the $10\ \mathrm{keV} < T < 20\ \mathrm{keV}$ temperature range of interest, it can be written in the following simple form:

$$nT\tau_E \geq 3 \times 10^{21} \mathrm{m}^{-3}\ \mathrm{keV\ s}\ , \tag{3}$$

In order to obtain so high values of the triple product $nT\tau_E$ there are two main strategies, based principally on density increase or energy confinement time increase respectively.

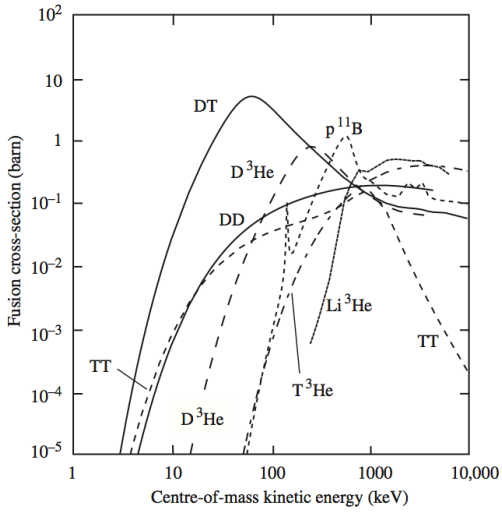

Figure 1: Fusion cross sections versus centre-of-mass energy for reactions of interest to controlled fusion energy. The curve labelled DD represents the sum of the cross sections of the various branches of the reaction.

The first way, followed by the "inertial fusion" experiments, aims to reach fusion conditions by heating and compressing with laser beams a small fuel target, typically in the form of a pellet that usually contains a dense mixture of deuterium and tritium. The second way, called "magnetic confinement fusion", adopts particular magnetic field configurations to contain for a sufficient time a warm plasma with low density ($n \sim 10^{20}\mathrm{m}^{-3}$). In this thesis I will deal with this second approach.
In present experiments the ignition condition can not be achieved and some power must be supplied from outside the plasma to maintain the energy balance. Even if they can not make the plasma work in self-sustained conditions, researchers try to maximize the efficiency of the reactors. The efficiency of a fusion reactor is measured by the gain factor Q, defined by

$$Q = \frac{\text{net thermal power out}}{\text{heating power in}} = \frac{P_{\text{out}} - P_{\text{in}}}{P_{\text{in}}} \,. \tag{4}$$

If the fusion process is self sustained ("ignition" condition, i.e. $P_{\text{in}} = 0$), the gain factor tends to infinity.

The present most promising project about magnetic confinement fusion is ITER (International Thermonuclear Experimental Reactor), that involves the construction of a machine which should be able to reach values of Q greater than 10. ITER is an international project that aims to demonstrate in the following years that it is possible to produce energy on a large scale by the process of controlled nuclear fusion.
ITER machine will be a tokamak, that is one of the most promising and most studied devices with toroidal magnetic field configuration. This axisymmetric device, whose acronym comes form the russian "TOroidal'naya KAmera s MAgnitnymi Katushkami" (Toroidal chamber with magnetic coils), developed around 1970 in Moscow, is practically a toroidal electrical transformer, in which the primary winding is made by the "poloidal field coils", twisted around the axis of the torus, and the secondary wind-

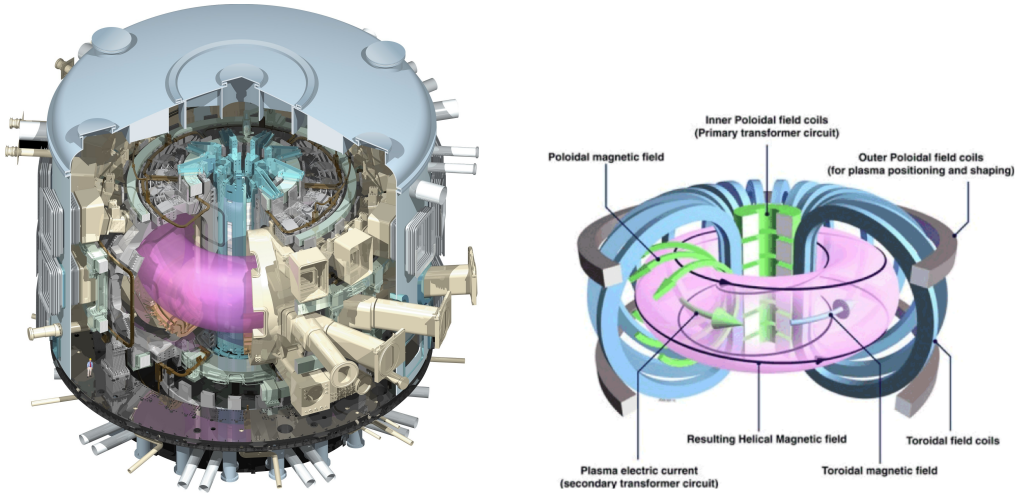

Figure 2: (Left) ITER machine; (Right) tokamak structure.

ing is constituted by a deuterium-tritium mixture, contained in a vacuum chamber, in which a toroidal magnetic field is generated by azimutally equally distributed "toroidal field coils". The plasma is made up by the electric discharge due to the high toroidal electric field generated by the transformer in the deuterium-tritium mixture. Moreover, the toroidal current so produced ("plasma current") builds up a poloidal magnetic field component, that results in a total helical magnetic field twisted around almost-concentric nested toroidal surfaces (cf. Fig. 2). Finally, some toroidal coils generate an additional magnetic field, needed for the plasma ring equilibrium. During the plasma discharge, the plasma current is forced to have a ramp up and a ramp down, separated by a plateau region where the plasma temperature reaches its maximum value.

The total magnetic field B satisfies the balance equation

$$J \times B = \nabla p \,, \tag{5}$$

between the magnetic force and the force due to the plasma pressure p, where J is the total current [1]. Equation (5) implies: $B \cdot \nabla p = 0$, so that the magnetic surfaces are surfaces of constant pressure. A magnetic surface can be labeled by a function that like the plasma pressure is constant on that surface, as for example the poloidal magnetic field flux ψ per radian in the toroidal angle (called "poloidal magnetic flux function"). These functions are called "flux functions" [2].

In order to reach the temperatures needed for fusion reactions to take place, in a tokamak a part of the required heating comes from the plasma current itself, via Joule heating. Unfortunately, this is not sufficient. In fact, the plasma resistivity scales with temperature as

[1] Along all this thesis, in order to have a light notation and to match with the notation used in the published paper that includes the major results of my PhD (cf. Maj et al. [1]), I will not use any bold character or particular superscript/subscript to distinguish between scalars, vectors and tensors. The identification relies on the context.

[2] For a detailed list of these functions with a rigorous introduction, we refer to the book by D'haeseleer et al. [2].

$T^{-3/2}$ and therefore this method is not efficient at high temperatures. Moreover, there is an upper limit to the current that can be carried by the plasma, related to magnetoidrodinamic (MHD) instabilities. The collection of the different methods of external heating adopted to overcome this drawback, is called "additional heating", and it divides between methods based on the injection of neutral particles and methods based on the injection of radio frequency waves. Within the second group, I will discuss the Electron Cyclotron Resonance Heating (ECRH), based on the injection of waves with a frequency equal to the cyclotron frequency of the plasma electrons (the electron cyclotron angular frequency is defined in the S.I. by $\Omega_e = e|B|/m_e$, where e is the electron charge, $|B|$ is the module of the magnetic field and m_e is the electron mass), heating the plasma by means of a resonant interaction.

In a tokamak the energy confinement time τ_E can be considerably shortened by many kinds of plasma instabilities, leading eventually to the total loss of plasma confinement and the consequent particles collision with the wall of the vacuum chamber (this event is called "disruption"). Many methods have been proposed to avoid the formation and growing of this instabilities, and for the particular case of the Neoclassical Tearing Modes (NTM), a particularly dangerous kind, the injection of EC beams can play a fundamental role, through the method called Electron Cyclotron Current Drive (ECCD), that consists in the generation of localized strips of current that neutralize the mechanism that makes the instability grow up.

In the following section ECRH and ECCD methods will be introduced in some more detail.

0.2 Heating and plasma instability control: electron cyclotron resonance heating and current drive

Electron cyclotron resonant interaction

The electron cyclotron resonant interaction is the process by which a wave with frequency close to the local cyclotron frequency of the plasma electrons interchanges energy and momentum with the plasma particles. The resonance condition for a plane wave propagating in a homogeneous infinite plasma with uniform background magnetic field, is given by

$$\omega - k_\parallel v_\parallel - n\Omega_e/\gamma = 0 \,, \tag{6}$$

where ω is the wave angular frequency, $k_\parallel$ and $v_\parallel$ are the parallel components of the wave vector and the electron velocity respectively with respect to the equilibrium magnetic field B, n is a positive integer, Ω_e is the electron cyclotron angular frequency and γ is the Lorentz factor

$$\gamma = \frac{1}{\sqrt{1 - \frac{v^2}{c^2}}} \,, \tag{7}$$

where c is the speed of light. The principal resonance occurs with $n = 1$, while the $n \geq 2$ resonances are the high order harmonics. Condition (6) is satisfied when an electron, with parallel velocity $v_\parallel$, "sees" the wave angular frequency ω, modified by the Doppler shift term $k_\parallel v_\parallel$, as an integer multiple of the realtivistically-corrected electron cyclotron angular frequency Ω_e/γ. As a consequence, the wave interacts with the plasma in a neighborhood of the surface $\omega = \Omega_e(x)$ (cold resonance surface), with the width of the

interaction region depending on the electrons velocity distribution. In a tokamak device, the frequency $f_{EC} = \omega/2\pi$ of the EC beam is chosen so that the cold resonance surface $\Omega_e(x)/2\pi = f_{EC}$ intersects the plasma volume (in ITER the EC system will have $f_{EC} = 170$ Ghz, with vacuum wavelenght of almost $\lambda \simeq 1.8$ mm). It is worth noting that the cold electron cyclotron resonance surfaces in a tokamak are almost cylindric, with the cylinder axis coinciding with the torus axis. This is a consequence of the fact that the B field in a tokamak is almost completely toroidal and its toroidal component is inversely proportional to the major radius R of the torus, while it is independent from the azimuthal (the tokamak is an axisymmetric device) and vertical coordinates. As a consequence, since Ω_e is proportional to B, the $\Omega_e(x) = \omega$ surfaces are almost cylindric.

If we restrict ourselves to the usual case of $|N_\parallel| < 1$, the resonance condition describes a semi-ellipse in the space of the parallel and perpendicular components of the normalized relativistic momentum $u = p/mc = \gamma v/c$:

$$\frac{(u_\parallel - u_{\parallel 0})^2}{\delta_\parallel^2} + \frac{u_\perp^2}{\delta_\perp^2} = 1 \,, \tag{8}$$

where the expressions for the centre of the ellipse and its semi-axis are given by

$$\begin{aligned} u_{\parallel 0} &= \frac{N_\parallel}{1 - N_\parallel^2} Y_n \,, \\ \delta_\parallel &= \frac{\sqrt{Y_n^2 - (1 - N_\parallel^2)}}{1 - N_\parallel^2} \,, \\ \delta_\perp &= \sqrt{1 - N_\parallel^2}\,\delta_\parallel \,, \end{aligned} \tag{9}$$

where $Y_n \equiv nY$ and $Y \equiv \Omega_e/\omega$ (cf. Fig. 3).

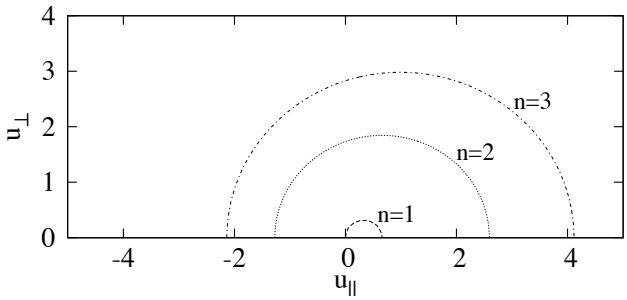

Figure 3: Resonance curves in the $(u_\parallel, u_\perp)$ space, with parameters $Y = 1, N_\parallel = 0.3$, consistent with EC beam propagation at the cold resonance for a beam launch from the top of the tokamak vacuum chamber. The curve with $n = 1$ represents the principal resonance, while $n = 2, 3$ are the first two harmonics.

The wave-plasma interaction results in a energy transfer to the electrons (in a plasma close to the equilibrium). As a consequence a general plasma heating is achieved through electron-electron and electron-ion collisions. This process is called Electron Cyclotron Resonance Heating (ECRH).

If a wave is injected with a non-vanishing wave vector parallel component $k_{\parallel}$, it can transfer a net parallel momentum to the electrons, resulting in the generation of current in the B direction, and therefore approximately in the toroidal direction (since the B field in a tokamak is almost completely toroidal). This process is called Electron Cyclotron Current Drive (ECCD). The mechanism underlying the current drive is a superposition of two principal effects. The Fisch-Boozer process, which generates a net current in the direction opposite to B, and the Ohkawa process, which generates a net current in the B direction. The Fisch-Boozer process can be summarized as follows: if there is a strong damping so that the waves are fully absorbed by electrons with a single sign of $v_{\parallel}$, a group of electrons with positive $v_{\parallel}$ is accelerated to higher energy and hence to a less collisional location in velocity space, since the collision rate declines as v^{-3}. As a consequence the collisional relaxation process symmetrizes the high energy electrons more slowly than it fills the lower energy location they came from resulting, in the limit of a steady-state process, in the formation of an excess of electrons with positive $v_{\parallel}$, and hence a current in the direction opposite to B. For the Ohkawa process explanation we refer to [3]. The description of the ECCD has to balance correctly the two contributions.

Neoclassical tearing modes and their control with electron cyclotron current drive

Amongst the various causes of deterioration of plasma confinement, one of the worst is constituted by the Neoclassical Tearing Modes (NTM). They are a particular type of MHD plasma instabilities that manifest themselves as tearing of nearby magnetic surfaces that reconnect changing their topology resulting in magnetic islands that grow, leading to a decrease of the energy confinement time and eventually to disruptions.

In order to characterize this instability, it is needed to introduce the safety factor q. Considering a magnetic field line that starts at a given position in the poloidal plane and after a toroidal angle $\Delta\phi$, m toroidal rotations and n poloidal rotations recovers the initial position, q is defined by

$$q \equiv \frac{\Delta\phi}{2\pi} = \frac{m}{n} \,. \tag{10}$$

The safety factor is a flux function, i.e. it is a quantity that is constant over a magnetic flux surface. In Fig. 4, the variation of q with the flux coordinate ρ (normalized toroidal radius defined as the square root of the toroidal flux normalized to its edge value) in a typical ITER scenario at the end of the plasma current flat-top is shown. Around the magnetic surfaces with rational values of q ("rational surfaces"), magnetic reconnection occurs, resulting in magnetic islands formation (Tearing Modes). Magnetic islands can be stable if there is not a deficiency in the local bootstrap current, an additional toroidal current due to the effects related with passing and trapped particles (toroidal effects related to passing and trapped particles are referred to as "neoclassical" effects). The NTM are the magnetic islands whose instability is driven by a helical perturbation of the bootstrap current.

It is possible to control these instabilities by restoring the unperturbed bootstrap current. This can be done by the interaction of narrow focalized EC beams with non-vanishing toroidal component of the wave vector, with small volume regions around the intersection of the considered magnetic surface and the cold cyclotron resonance "cylindrical" surface. By means of the Electron Cyclotron Current Drive (ECCD) process, an helical

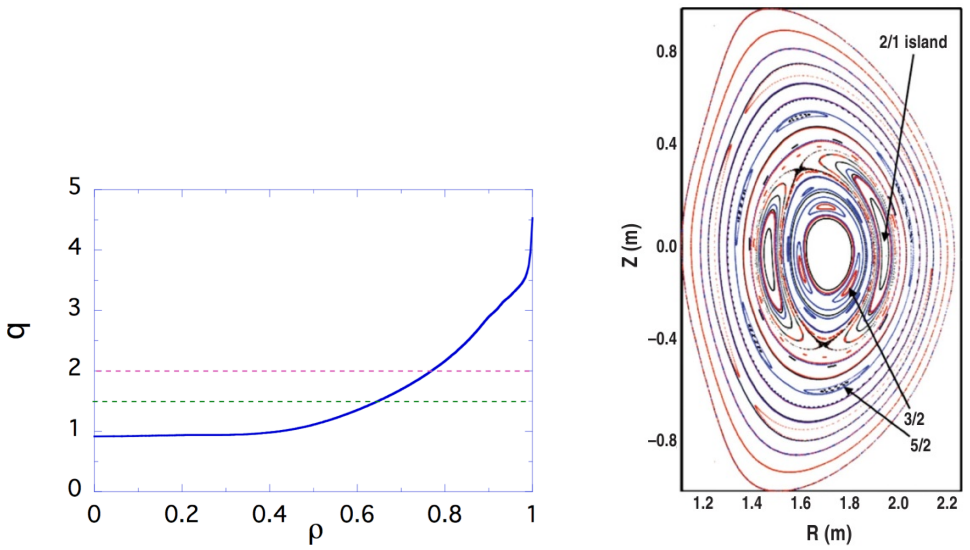

Figure 4: (Left) q profile of a typical ITER scenario at the end of the flat top. The $q = 3/2$ and $q = 2$ rational surfaces are traced in green and red respectively; (Right) formation of magnetic islands by magnetic reconnection around rational surfaces in the DIII-D tokamak, currently operating (poloidal plane view).

strip of current is generated that balances the "neoclassical" perturbation of the bootstrap current. Power deposition can be performed by continuous wave injection or by modulated injection. The modulated injection may overcome the drawback caused by the fact that a magnetic island position varies periodically with time, and consists in making the wave launcher operate in finite time intervals, in order to deposit power only in the inner region of the islands improving the stabilization efficiency.

The description of the propagation of these focalized EC beams in the tokamak anisotropic magnetized plasma and their EC resonant interaction resulting in the required current generation is the main topic of this PhD thesis.

0.3 The ITER Electron Cyclotron Power System

In order to perform heating and current drive (H&CD), in the ITER tokamak it will be provided a system capable to deliver 24 MW of power to the plasma by Electron Cyclotron wave injection, 20 MW by Ion Cyclotron wave injection and 33 MW by neutral beam injection.

The ITER EC H&CD system interface with the tokamak vacuum chamber will be constituted by an Equatorial Launcher (EL, cf. Fig. 5), placed near the equatorial plane of the torus, which will be able to inject beams toward the axis of the plasma, principally with ECRH&CD purposes (central heating and current profile tailoring), and four Upper Launchers (UL, cf. Fig. 6), placed at different toroidal angles, that will be able to inject beams from the upper region of the vacuum vessel toward the rational surfaces of interest in a region close to the cold electron cyclotron resonance surface, principally for

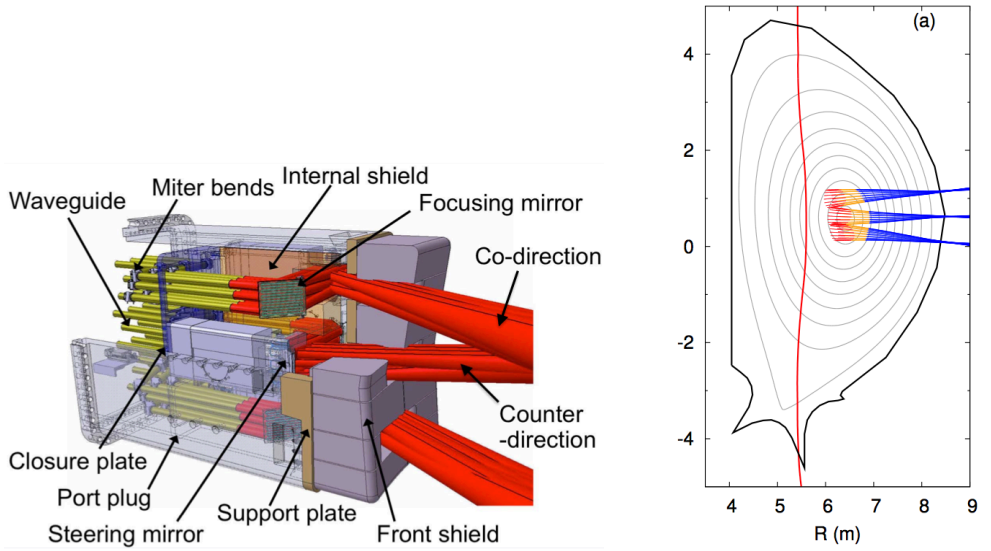

Figure 5: (Left) Equatorial Launcher scheme; (Right) Equatorial Launcher beams directed toward the plasma axis for central heating purposes (poloidal plane view).

ECCD purposes.

During the ITER discharge, the EC power will be used for different purposes at various time stages. In Fig. 7 the total EC power time variation planned in the actual design is shown, compared to the time variation of the plasma current. The central heating, principal purpose of the EL, will be carried during the current ramp-up and flat-top, while the MHD instabilities control, principal purpose of the UL, will be performed mainly during the flat-top ("burn" phase). Moreover, the EC system will be active also for other tasks, like for example the assisted startup of the plasma discharge, and during current ramp-up and ramp-down in order to assist the transitions between the Low confinement mode (L-mode) and the High confinement mode (H-mode), that is is a particular high-confinement regime that can be achieved in most of the present tokamaks.

The EC power will be generated by the Gyrotrons, that are a particular kind of masers capable of delivering high power at millimeter wavelengths. 24 Gyrotrons will be hosted in a dedicated building (Radio Frequency building, cf. Fig. 8 for a top view of the whole ITER EC system). The waves will be transmitted to the tokamak interface by a power distribution system made of 24 transmission waveguides. 24 Beams of 1 MW power each will be produced by the gyrotrons in the RF building and be switched among the launchers by the waveguides. The output from the waveguides will consist in almost pure Gaussian beams.

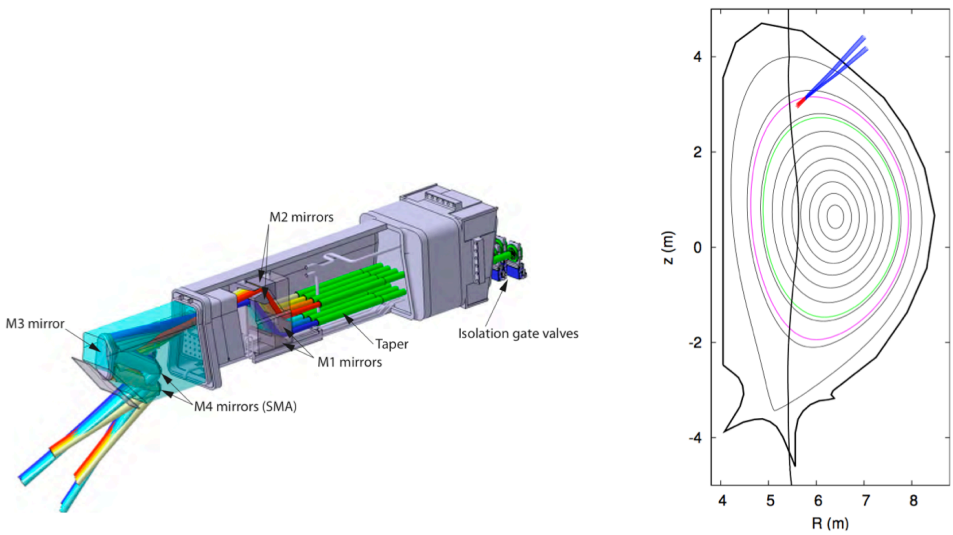

Figure 6: (Left) Upper Launcher scheme; (Right) Upper Launcher beams directed toward the $q = 2$ rational surface for ECCD purposes (poloidal plane view).

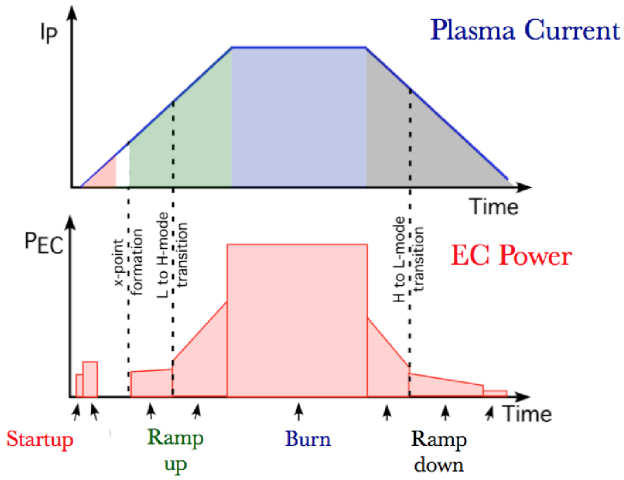

Figure 7: Distribution of the EC H&CD during an ITER plasma discharge. EC power versus time (bottom), compared with the plasma current time variation (top).

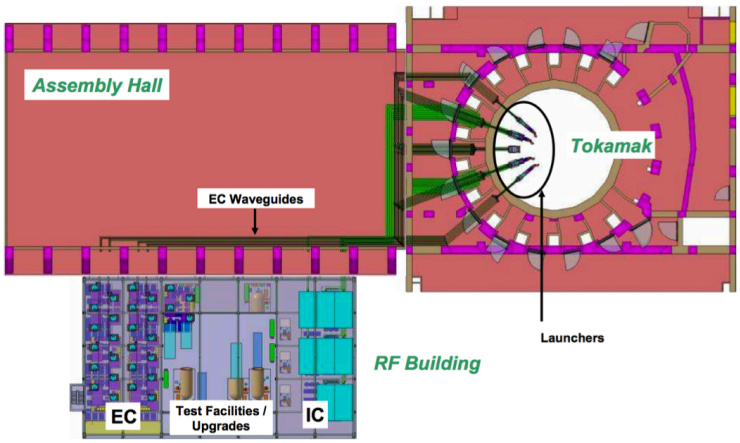

Figure 8: ITER EC system scheme (top view).

The Upper Launcher

Now a brief introduction to the ITER Upper Launcher is given. For a detailed description, we refer to Henderson et al. [4].

In Fig. 9 an Upper Launcher cross-section is presented, showing its inner optical system. Inside each one of the four launchers, eight Gaussian beams of 1 MW power each coming from the transmission waveguides can be reflected and focalized on two final mirrors, the Upper Steering Mirror (USM) and the Lower Steering Mirror (LSM). From either USM or LSM four beams are reflected toward the plasma, aiming to the selected rational surface.

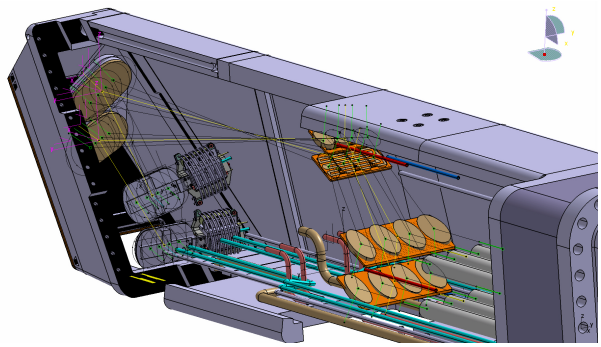

Figure 9: cross-section of the Upper Launcher, showing how the eight incoming beams are reflected on the two final mirrors, the Upper Steering Mirror (USM) and the Lower Steering Mirror (LSM).

The beams can be launched with different poloidal angles, with a non-vanishing toroidal angle, thanks to a steering system that allows the USM and LSM to rotate about an axis. The poloidal and toroidal injection angles α and β are defined as the angle between the launching wave vector and the horizontal plane and the angle between the launching wave vector and the toroidal direction respectively, that is $N_{0R}\tan\alpha = N_{0z}$ and $N_{o\varphi} = \sin\beta$, where $(N_{0R}, N_{o\varphi}, N_{0z})$ are the cylindrical coordinates of the launching index of refraction vector $N_0 = k_0 c/\omega$. As a result the beams can cross the cold electron cyclotron resonance surface in a wide range of flux coordinate ρ (cf. section 0.2), aiming at the $q = 2$ and $q = 3/2$ rational surfaces, around which the NTM modes develop, down to the $q = 1$ surface, where the sawtooth MHD instability occurs.

In order to achieve narrow power deposition profiles, needed for NTM stabilization, the present optical layout of the UL focuses each of the four beams (being $w \sim 5$ cm the beam size, that is the radius of the beam where the E field is $1/\mathrm{e}$ times the peak value, at the final mirror surface) to a small beam waist $w_0 \sim 2$ cm at a distance of almost 1.6 m into the plasma (LSM parameters; USM parameters are similiar). Moreover, for each steering mirror (USM or LSM), in order to obtain a high peak in the total power deposition profile, sum of the power profiles of the the four beams reflected by the mirror, the beams have to superpose with high precision in the plasma absorption zone. To obtain this result it is needed to do in parallel a set up of the inner optical system and a work consisting in performing numerical simulations of propagation and absorption of beams starting from either the USM or the LSM. In this thesis we will focus on the propagation

and absorption of single beams starting from the center of either the USM or the LSM ("virtual beams"), instead of describing the four beams superposition.

The UL design is actually in progress, and I worked on this subject during the PhD.

0.4 Numerical simulations of EC H&CD and complex geometrical optics

To optimize the design of EC devices like ITER UL and EL or to prepare experimental campaigns on existing machines, it is needed to make predictions of the propagation and interaction of the EC beams with the anisotropic plasmas under consideration. The beam propagation and resonant interaction has to be correctly described in order to develop simulation codes capable of making predictions on trajectories and absorption profiles. Because of the complexity of the 3D propagation and H&CD calculation, it is in general impossible to recover analytical solutions. For low frequency waves it is possible to solve the full wave equation numerically, discretizing space coordinates with a grid which step width is of the order of the wavelength. On the contrary, for EC waves in large magnetic confinement devices the wavelength to plasma size ratio λ/L is extremely small, thus hampering the direct numerical solution of the relevant wave equation (in ITER $\lambda \sim 2$ mm, $L \sim 2$ m). In fact, since the computational time increases with the number of nodes of the space grid, if the ratio λ/L is too small, it is needed an huge amount of time to perform a full-wave simulation of the wave propagation.

Therefore, the description of high-frequency waves in inhomogeneous media is usually dealt with by means of asymptotic methods that greatly simplify the computational problem. One such method is geometrical optics (GO), that relies on the approximation $\lambda/L \to 0$, giving a description of the wave in terms of rays tangent in every point to the wave energy flux vector field. Geometrical optics, thanks to the $\lambda/L \to 0$ approximation, has the useful feature of transforming a difficult non-linear problem in a simple integration of a system of ordinary differential equations.

This description, however, fails to take into account the diffraction effects that become important in the caustic regions, where the GO rays intersect. The correct description of the wave field in these regions is required to make predictions on applications that involve focused beams, like ITER UL beam injection. In order to overcome this drawback, a series of alternative asymptotic methods that take into account diffraction effects was developed. Among them, I will focus on the "complex geometrical optics" (CGO) methods. These methods share the same ansatz for the electric field, which is built upon the standard WKB ansatz of GO by replacing the real-valued eikonal with a complex-valued function referred to as complex eikonal. Moreover, while the GO method is based on the smallness of the ratio λ/L, in CGO a new intermediate length scale w_0 appears, given by the waist size of the beam, satisfying $\lambda \ll \mathrm{w}_0 \ll L$ (Quasi-Optical approximation).
The two main CGO branches are the "complex ray theory" and the "complex eikonal theory". The first method relies on the complexification of GO rays, while the second is based on the construction of a new set of rays in the real space, obtained as perturbation of the GO rays due to diffraction effects. When we will write "CGO" in this thesis, we will refer to "complex eikonal theory" CGO method.

The "complex eikonal theory" , first applied to fusion plasmas by Mazzucato [5] and

then exploited by some other authors, was used to implement the beam tracing code GRAY (cf. Farina [6]), employed to make predictions on beam propagation and H&CD performances for many fusion devices, ITER included.

In addition to CGO methods, other theoretical approaches were developed. The "paraxial WKB method", in particular, led to the implementation of the beam tracing code TORBEAM (cf. Poli et al. [7]).

All the numerical results shown in this thesis are obtained with the GRAY code, except for the comparison between GRAY and TORBEAM results contained in section 2.2.

0.5 Thesis overview

I spent the PhD period working at the "Istituto di Fisica del Plasma" (IFP) of the "Consiglio Nazionale delle Ricerche" (CNR), in Milan. This Thesis is the result of the work done in collaboration with my PhD supervisor Daniela Farina and Lorenzo Figini, within a research group that studies the propagation and the absorption of high power Gaussian beams in plasmas of magnetic nuclear fusion interest. Part of the work was done in collaboration with Omar Maj (Max Planck Institut für Plasmaphysik, Garching, Germany), with a two week collaboration on site in Garching.

The work done is divided in two principal branches: a theoretical one concerning the description of the propagation and absorption of high frequency beams in anisotropic media, with original results obtained in collaboration with Omar Maj that led to the publication of a paper on an international scientific journal [1], and a numerical-applicative one consisting in doing simulations of the propagation and absorption of Electron Cyclotron beams in conditions of interest for the ITER project by using and optimizing the beam tracing code GRAY, including the optimizations resulting from the theoretical work.

Within the theoretical work, the main part is constituted by the analysis of the propagation of high frequency Gaussian beams in anisotropic media, within the CGO framework. While the CGO solution of the wave equation for the electric field at the dominant order in the λ/L parameter is well known (cf. Mazzucato [5], for example), leading to a description of the wave by a bundle of rays that take into account the diffraction effects due to the beam finite width, the rigorous solution of the first order wave equation and the consequent derivation of the wave energy flux can not be found in literature. This gap has been filled developing a new approach at the CGO ordering of the wave equation that simplifies significantly the analysis of the transport equation for the wave field amplitude and leads to the wave energy flux derivation. Moreover, we obtained as additional results the mathematical derivation of the GRAY code ray equations and the demonstration that GRAY rays correctly describe the wave energy flow in the CGO approximation. This results, together with two numerical tests made with GRAY and TORBEAM codes in order to have an estimate of the theory in ITER-like conditions, are published on Physics of Plasmas [1], and presented in chapters 1 and 2 of this thesis.

Besides the description of EC beams propagation in CGO framework, leading to the described results, the related problem of the EC beam resonant interaction with the plasma has been dealt with. This process, well described for plane waves interacting with a infinite homogeneous plasma with uniform equilibrium magnetic field, has not a

full solution for the more complicated case of the propagation of finite width beams in anisotropic plasmas with non-uniform equilibrium magnetic field, like fusion plasmas. The effects related to the spatial finiteness of both the wave and the plasma, resulting in a finite time wave-plasma interaction, together with the effects due to the anisotropy of the plasma and the non-uniformty of the equilibrium magnetic field, lead to a broadening of the interaction region and a subsequent broader and less-peaked deposition of power by the beams. The papers actually present in literature on the subject (cf. Demeio-Engelmann [8] , for example) give a global solution of the problem, that has to be matched with the ray description of the wave adopted in the beam tracing codes like GRAY. In order to develop an approximate model that describes the wave absorption along the single ray, the effects of the finite width of the beam and the non-uniformity of the equilibrium magnetic field have been treated separately, leading to the implementation of a new version of the GRAY code that takes into account these corrections. The foregoing results are presented in chapter 3.

Finally, in chapter 4, the results of the analysis of the propagation and absorption of EC beams in a typical ITER scenario using the GRAY code are presented, in order to give an example of the numerical work performed during the PhD. These results are of interest for the ITER Upper Launcher design.

Part I

Beam propagation

CHAPTER 1

High frequency diffracting beams propagation in a magnetized plasma in complex geometrical optics

This chapter contains the main theoretical results obtained during my PhD. It is composed almost completely of the results published in [1]. Sections 1.4 and 1.5 show the theoretical core of the work, which mainly consists in a new rigorous derivation of the wave energy flux in the complex geometrical optics framework, that up to now was not obtained in the literature.

In the first two introductory sections 1.1 and 1.2 we fix the notation and review basic results and ideas, upon which the geometrical optics and the complex geometrical optics methods rely. In section 1.3 some results concerning the paraxial character of the beams, obtained independently by Pereverzev [9] and Maslov [10], are reviewed, because they are pivotal in the wave energy flux derivation. In section 1.4 the solution of the wave equation at the dominant orders in the GO parameter λ/L is presented, leading eventually to the rigorous derivation of the ray equations used in the GRAY beam tracing code [6]. Finally, in section 1.5 the wave energy flux derivation within the complex eikonal theory is shown, with the additional result that the ray description of a EC beam made by the GRAY code correctly describes the wave energy flow in the CGO framework.

For sake of simplicity, we consider spatially non-dispersive media for which the constitutive relation between the electric displacement D and the electric field E is local, namely, $D = \epsilon E$, where ϵ is a matrix referred to as the dielectric tensor (see Appendix A).

1.1 Review of standard geometrical optics

In this section it is presented the review material about standard geometrical optics. The focus is pointed on the rigorous presentation of the ansatz and the main results of this method, instead of dwelling on the details of the derivation, which can be inferred by specializing the complex eikonal theory described in section 1.4.

Every arbitrary wave such that the λ/L ratio is sufficiently small can be regarded as a plane wave in every sufficiently small region of space. In this approximation the "phase surfaces" can be introduced and in every little portion of space the direction of propagation is defined as the normal unit vector to the phase surface. Moreover, the "rays" can be introduced as the lines whose tangent in every point coincide with the direction of propagation of the wave. The study of the wave propagation in this context is the subject of the geometrical optics.

1.1.1 Wave equation and electric field ansatz

The equation for the electric field of a monochromatic electromagnetic wave beam in a stationary spatially non-dispersive medium is

$$\nabla \times (\nabla \times E(\kappa, x)) - \kappa^2 \epsilon(\kappa, x) E(\kappa, x) = 0 \, . \tag{1.1}$$

Equation (1.1) is written in the dimensionless form adopted by Pereverzev, where the coordinates $[x]_i \, , \; i = 1, 2, 3$ are normalized to the scale L of typical spatial variations of the medium, and the large parameter

$$\kappa = k_0 L \, , \tag{1.2}$$

where $k_0 = \omega/c$ is the vacuum wavenumber, appears naturally. In addition, $[\nabla]_i = \partial/\partial x^i$ and c is the speed of light in free space. The dependence of the solution $E(\kappa, x)$ on the parameter κ is explicitly indicated, whereas the additional dependence on the beam frequency ω is implied in the dielectric tensor ϵ of the medium and

$$E(\kappa, x, t) = E(\kappa, x) e^{-i\omega t} \, . \tag{1.3}$$

Asymptotic solutions of (1.1) in the limit $\kappa \to \infty$ can be constructed by modest computational means, and yet provide excellent approximations of the exact wave field for many applications as far as the parameter κ is large. Asymptotic solutions offer an effective alternative to the major computational problem of direct numerical integration of (1.1) for very high frequencies in large three-dimensional domains.

In geometrical optics, a solution of Eq. (1.1) is sought in the form (eikonal ansatz)

$$E_{\mathrm{GO}}(\kappa, x) = a(\kappa, x) e^{i\kappa S(x)} \, , \tag{1.4}$$

with $a(\kappa, x)$ defined in the limit $\kappa \to \infty$ by the asymptotic sum

$$a(\kappa, x) \sim \sum_{j=0}^{\infty} \kappa^{-j} a_j(x) \, , \tag{1.5}$$

where $S(x)$ is a real-valued smooth function representing the short-scale oscillations of the field and referred to as the eikonal, while $a_j(x)$ are vector-valued complex smooth functions that will be generically referred to as amplitudes.
It is assumed that the amplitudes are bounded, that is there exist a sequence of real numbers C_j so that $|a_j(x)| \leq C_j \; \forall \; j$, and as a consequence it is easy to prove that the asymptotic sum $a(\kappa, x)$ is bounded too, that is there exist two constants $C_0 > 0$ and $\kappa_0 > 0$ so that

$$|a(\kappa, x)| \leq C_0 \; for \; \kappa \geq \; \kappa_0 \, . \tag{1.6}$$

The dielectric tensor is assumed to be smooth and have the asymptotic expansion

$$\epsilon(\kappa, x) = \epsilon_0(x) + \kappa^{-1} \epsilon_1(x) + O(\kappa^{-2}) \, . \tag{1.7}$$

The medium is considered weakly dissipative. As a consequence the dominant order term ϵ_0 of the dielectric tensor is Hermitian, i.e. , $\epsilon_0 = \epsilon_0^*$, where ϵ_0^* is the Hermitian conjugate of ϵ_0, i.e., the transpose of the complex-conjugate of ϵ_0 ($[\epsilon_0^*]_{ij} = [\epsilon_0]_{ji}^*$). The absorption coefficient, related to the anti-Hermitian part $\epsilon^a = \kappa^{-1}\epsilon_1^a + O(\kappa^{-2})$, is vanishingly small as $\kappa \to \infty$. Moreover, we will disregard the possible κ^{-1} order residual

Hermitian part, that is $\epsilon^h = \epsilon_0 + O(\kappa^{-2})$. Here and in throughout the thesis the Hermitian part and the anti-Hermitian part of a matrix M are denoted respectively by

$$M^h = \frac{M + M^*}{2} , \qquad (1.8)$$
$$M^a = \frac{M - M^*}{2i} ,$$

and $M = M^h + iM^a$.

After substituting the electric field ansatz (1.4) into the wave equation (1.1), we obtain as a result some terms multiplied to different integer powers of κ^{-1}. This fact leads to separate equations that can be solved individually.

1.1.2 Solution of the dominant order wave equation: ray tracing equations

In order to solve the dominant order wave equation, it is needed to introduce the dispersion tensor of the medium, that is the matrix-valued smooth function defined by

$$D_{0,ij}(x, N) = N^2\delta_{ij} - N_iN_j - \epsilon_{0,ij}(x) . \qquad (1.9)$$

This tensor appears naturally testing the wave operator, i.e., the left-hand side of Eq. (1.1), with a plane wave $e^{i\kappa N\cdot x}$ and separating the leading order in κ. This is defined on a domain in the $x - N$ space, which is referred to as the wave phase space. In view of the definition of κ and the normalization of spatial coordinates x, the conjugate variable N has the physical meaning of the refractive index vector.

The real eigenvalues λ_i of D_0 give the local dispersion functions of wave modes supported by the medium. Here it is assumed that the eigenvalues λ_i are well separated, namely, there exists a strictly positive constant $C > 0$ such that $|\lambda_i(x, N) - \lambda_j(x, N)| \geq C$ for $i \neq j$ and for (x, N) in the relevant domain in the wave phase-space. This implies that the dispersion surface of one mode does not get close to that of the other modes, and linear mode conversion is excluded, that is, no energy exchange can take place among different modes. Hence under such hypothesis, each mode is independent of the others and the wave equation (1.1) in the limit $\kappa \to \infty$ can be reduced to decoupled scalar equations describing the various modes. Let us denote by $H(x, N)$ the eigenvalue of $D_0(x, N)$ relevant to the considered mode, and let $e(x, N)$ be the corresponding unit eigenvector. For simplicity, we consider the case of simple eigenvalues, i.e., the corresponding eigenspace is assumed to be one-dimensional. Upon substituting (1.4) into (1.1) and performing the asymptotic expansion in the limit $\kappa \to \infty$, one finds that multiple solutions exist, one for each propagation mode supported by the medium. Under the conditions stated above, each mode is independent. We consider the one which corresponds to the eigenvalue-eigenvector pair $H(x, N)$, $e(x, N)$.

The dominant order amplitude a_0 is found proportional to $e(x, \nabla S(x))$, namely

$$a_0(x) = A(x)e(x, \nabla S(x)) , \qquad (1.10)$$

where $A(x)$ is a scalar complex amplitude. Therefore the polarization of the leading order term in the geometrical optics solution is determined by the eigenvector $e(x, N)$ for $N = \nabla S$.

The eikonal $S(x)$ is determined by the standard eikonal equation

$$H(x, \nabla S(x)) = 0 \, . \tag{1.11}$$

This equation can be solved by the method of the characteristics, leading to the pair of Hamiltonian-like equations

$$\begin{aligned} \frac{dx(\tau)}{d\tau} &= \left. \frac{\partial H(x,N)}{\partial N} \right|_{H(x,N)=0} \, , \\ \frac{dN(\tau)}{d\tau} &= - \left. \frac{\partial H(x,N)}{\partial x} \right|_{H(x,N)=0} \, . \end{aligned} \tag{1.12}$$

where the parameter τ plays the role of time. The projection of a solution $(x(\tau), N(\tau))$, satisfying the local dispersion relation $H(x, N) = 0$, into the physical space is called a geometrical optics ray. The construction of a solution of (1.11) using rays is obtained as follows. Let us assume, as boundary conditions, that the wave field is prescribed in the form $E_0(\kappa, y) \propto e^{i\kappa S_0(y)}$ on a 2-dimensional surface

$$\Sigma_0 = \{x; \; x = x_0(y)\} \, , \tag{1.13}$$

parametrized by the variables $y = (y^1, y^2)$. One can think of Σ_0 as the surface of either a mirror or an antenna, where the launched wave field is known. The initial conditions $(x_0(y), N_0(y))$ for the Hamilton's Eqs. (1.12) are determined by the gradient of the initial phase $S_0(y)$, together with the local dispersion relation $H(x_0(y), N_0(y)) = 0$. Meaningful data must be such that the lifted surface,

$$\Lambda_0 = \{(x, N); \; x = x_0(y), \; N = N_0(y)\} \, , \tag{1.14}$$

is non-characteristic, i.e., the Hamiltonian orbits of the system (1.12) originating from points of Λ_0 are transversal (not necessarily orthogonal) to Λ_0 itself, so that orbits move away from the surface, and $\nabla_N H|_{\Lambda_0} \neq 0$. Then, the solution of Hamilton's Eqs. (1.12) can be readily found in the form $(x(\tau, y), N(\tau, y))$ depending on the initial point y on the launching surface Λ_0. This defines a 3-dimensional surface

$$\Lambda = \{(x, N); \; x = x(\tau, y), \; N = N(\tau, y)\} \, , \tag{1.15}$$

immersed into the 6-dimensional wave phase space, and parametrized by coordinates (τ, y^1, y^2). Indeed, Λ is the flow out of Λ_0 by the Hamiltonian flow. As a consequence of the non-characteristic hypothesis on Λ_0 , the relationship $x = x(\tau, y)$ defines a change of coordinates, at least locally near Λ_0. The new coordinates (τ, y) establish a one-to-one correspondence between a neighborhood of Σ_0 in the physical space and a neighborhood of Λ_0 in the surface Λ. it is possible to proof that, at least near Σ_0, there exists a real function $S(x)$ such that $N(\tau, y) = \nabla S(x(\tau, y))$ and $S|_{\Sigma_0} = S_0(y)$. It follows that $S(x)$ solves Eq. (1.11) with the appropriate boundary condition. Despite its rather abstract definition, the construction of S in Lagrangian coordinates is actually straightforward. Specifically, one has

$$\frac{\partial S}{\partial \tau} = \nabla S \cdot \frac{dx}{d\tau} = N \cdot \frac{\partial H}{\partial N} \, . \tag{1.16}$$

After solving the dominant order wave equation, $A(x)$ is still unknown.

1.1.3 Solution of the first order wave equation: amplitude transport equation

After solving the first order wave equation, it is found that $A(x)$ is determined by the amplitude transport equation

$$V(x) \cdot \nabla A(x) = [-\gamma_1(x) + i\delta_1(x) - \frac{1}{2}\nabla \cdot V(x)]A(x) \,, \tag{1.17}$$

where the vector field

$$V(x) = \frac{\partial H(x, \nabla S(x))}{\partial N} \tag{1.18}$$

plays the role of the group velocity,

$$\gamma_1 = e^* \cdot \epsilon_1^a e \tag{1.19}$$

accounts for wave damping, and

$$\delta_1 = ie^* \cdot \{H, e\} - \frac{i}{2}\sum_{i,j} D_{0,ij}\,\{e_i^*, e_j\} \tag{1.20}$$

accounts for a lower order shift in the phase, due to the effects of polarization transport. In both Eqs. (1.19) and (1.20), all phase space functions are evaluated at $N = \nabla S(x)$, e_i are the components of e, and Poisson brackets are defined by

$$\{f, g\} = \frac{\partial f}{\partial N_i}\frac{\partial g}{\partial x^i} - \frac{\partial f}{\partial x^i}\frac{\partial g}{\partial N_i} \,. \tag{1.21}$$

From (1.12) and (1.18) it follows that the amplitude is transported along the rays by the amplitude transport equation (1.17), and (1.17) can be rewritten in the following form

$$\frac{\partial A}{\partial \tau} = \left[-\gamma_1 + i\delta_1 - \frac{1}{2}\nabla \cdot V\right] A \,. \tag{1.22}$$

Eqs. (1.16) and (1.22) form a system of ordinary differential equations that can be conveniently integrated together with Hamilton's Eqs. (1.12) by standard numerical techniques, like for example Runge-Kutta methods.

1.1.4 Geometrical optics estimate of the residual

The geometrical optics estimate of the residual can now be stated: given a (sufficiently regular) classical solution $S(x)$ and $A(x)$ of Eqs. (1.11) and (1.17) in a bounded domain, and setting $a_0(x) = A(x)e(x, \nabla S(x))$, there exists a corrector $a_1(x)$, such that the geometrical optics solution,

$$E_{\mathrm{GO},1}(\kappa, x) = (a_0(x) + \kappa^{-1}a_1(x))e^{i\kappa S(x)} \,, \tag{1.23}$$

solves (1.1) with a residual

$$\left|\kappa^{-2}\nabla \times \nabla \times E_{\mathrm{GO},1}(\kappa, x) - \epsilon(\kappa, x)E_{\mathrm{GO},1}(\kappa, x)\right| \leq C\kappa^{-2} \,, \tag{1.24}$$

uniformly for x in the considered domain, $C > 0$ being a constant. The leading order term in (1.1) is $O(\kappa^2)$, hence the whole equation has been multiplied by κ^{-2}. The corrector $a_1(x)$ however is never evaluated in practice.

1.1.5 Wave energy flux

In addition to its computational advantages, geometrical optics allows us to extract relevant physical information. Within the limits of applicability, i.e., when the one-to-one correspondence between physical space and the Lagrangian manifold Λ makes possible to recover solutions $S(x)$ and $A(x)$, Eq. (1.17) implies that the wave energy density is transported along geometrical optics rays. More specifically, Eq. (1.17) can be recast in the form (after some algebra and restoring dimensional quantities)

$$\nabla_r \cdot [v_g W] = -\gamma W \,, \tag{1.25}$$

where ∇_r denotes the gradient in physical (dimensional) coordinates,

$$v_g = -\frac{\partial H/\partial k}{\partial H/\partial \omega} = c \left| \frac{\partial(\omega H)}{\partial \omega} \right|^{-1} V \tag{1.26}$$

is the group velocity, and

$$W = \left| \frac{\partial(\omega H)}{\partial \omega} \right| \frac{|A|^2}{16\pi} = \frac{1}{\omega} \left[e^* \cdot \frac{\partial(\omega^2 \epsilon_0)}{\partial \omega} e \right] \frac{|A|^2}{16\pi} \tag{1.27}$$

is the total wave energy density, comprising the electric, magnetic, and sloshing energy (related to the movement of the particles related to the wave transit). At last,

$$\gamma = \frac{c}{L} \left| \frac{\partial(\omega H)}{\partial \omega} \right|^{-1} 2\gamma_1 = \frac{2c}{L} \left| \frac{\partial(\omega H)}{\partial \omega} \right|^{-1} e^* \cdot \epsilon_1^a e \tag{1.28}$$

is the energy absorption coefficient. Here, all derivatives with respect to the frequency are taken at constant wave vector $k = \omega N/c$, and phase-space functions are evaluated at $N = \nabla S$.

1.2 Introduction to complex geometrical optics

The construction of the rays solution of Eqs. (1.11) however relies on the one-to-one correspondence between physical space and the manifold Λ, and this can be established only locally. Away from the surface Σ_0 geometrical optics rays can cross each other. Correspondingly, Λ turns vertical and fold onto itself so that, over a given point x in the physical space, multiple branches of Λ can exist. At such points, the value of $S(x)$ and $A(x)$ is not uniquely defined. This points are called "Caustics".
Caustics generated by light can be noticed in everyday life. A typical example is constituted by the bright stripes visible on the pool floor, generated by the light that shines through the waves on the water surface, being focused on the pool floor, but there are more complicated patterns resulting from light reflection or refraction by common items (cf. Fig. 1.1).

In order to correctly describe a focused Gaussian EC beam in the neighborhood of the waist, we have to deal with a focal caustic. In this region the GO ray description of the beam fails to describe it properly, because the rays obtained integrating (1.12) cross each other (cf. Fig. 1.2, left panel) and the value of $S(x)$ and $A(x)$ is not uniquely defined. In fact, if one tries to compute the amplitude integrating (1.22), the result diverges at the focus. This behavior is a consequence of the fact that the finite energy of the beam in

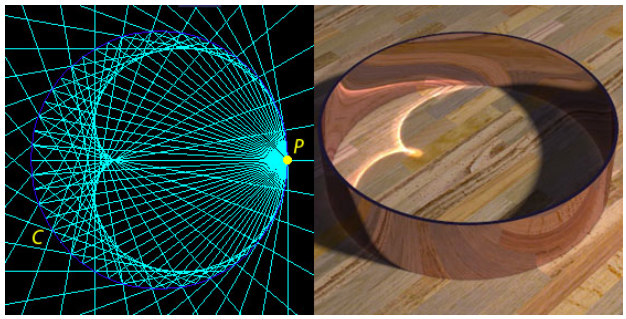

Figure 1.1: Caustic situation where light rays reflected by a metallic cylinder intersect showing a pattern with a cardioid envelope.

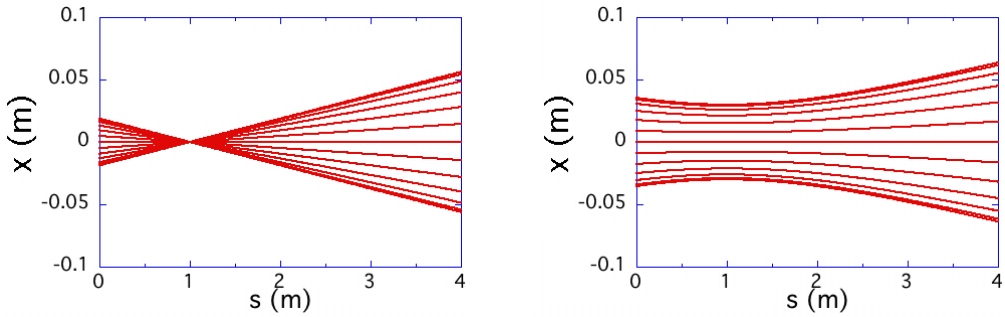

Figure 1.2: Gaussian beam near the focus, two alternative ray description: (Left) GO rays; (Right) CGO "extended rays".

this model is concentrated in a region of vanishing volume at the focus, with consequent blow up of the energy density, proportional to $|A|^2$. In reality, the plasma propagation introduces a deformation of the beam with the result that the rays do not intersect perfectly, but in the GO framework the energy is still concentrated in a region narrower that the real physical region in which it is seen experimentally, with consequent values of the energy density higher than the real physical values.
This fact is not an inconsistency of the GO model, because at the focus the GO approximation stops to apply. In fact, let us consider a beam propagating in vacuum in the z direction. At the focus the beam is transversally constricted in a null spatial region, and as a consequence the spread in the x and y components of the wave vector spectrum tends to infinity. Therefore the wavelength spread tends to infinity too:

$$\Delta\lambda = \left|\frac{\partial\lambda}{\partial k_x}\right|\Delta k_x + \left|\frac{\partial\lambda}{\partial k_y}\right|\Delta k_y = \frac{2\pi}{|k|^2}(k_x\Delta k_x + k_y\Delta k_y) \to \infty \,. \tag{1.29}$$

It follows that at the focus there are spectral components that violate the condition $\lambda/L \ll 1$.

In order to overcome this drawback the complex geometrical optics (CGO) method can be used. It is based on the introduction of a imaginary part in the eikonal function, to take into account the finite transversal extension of the beam. The CGO electric field form, substituted in the wave equation, gives at the dominant order an equation that can be solved with the method of characteristics obtaining a ray description different from GO in the focal region. The new rays, called "extended rays", do not intersect at the focus (cf. Fig. 1.2, right panel) and correctly describe the wave energy flow, as it will be demonstrated in this chapter. The CGO wave electric field ansatz is:

$$E_{\mathrm{CGO}}(\kappa, x, t) = E_{\mathrm{CGO}}(\kappa, x)e^{-i\omega t} \,, \tag{1.30}$$

with

$$E_{\mathrm{CGO}}(\kappa, x) = a(\kappa, x)e^{i\kappa\psi(x)} \,, \tag{1.31}$$

and

$$\psi(x) = S(x) + i\phi(x) \,, \tag{1.32}$$

where, with a slight abuse of notation, it is customary to denote by $S(x)$ both the GO eikonal and the CGO real part of the complex eikonal, although those are two different functions. The condition $\phi(x) \geq 0$ on the imaginary part of the eikonal is required by the boundedness of the wave field for $\kappa \to +\infty$.

This form of the electric field is suitable to describe Gaussian beams. Consider for simplicity the electric field expression of a non-astigmatic Gaussian beam propagating in free space in the z direction (cf. Appendix B for a review of the Gaussian beam E field form and a description of the relation between the QO approximation and the paraxial character of the beam):

$$E(x, y, z, t) = E(z)e^{-i\phi_{\mathrm{Gouy}}(z)}e^{-\frac{x^2+y^2}{w(z)^2}}e^{ik_0\left[\frac{x^2+y^2}{2R(z)}\right]}e^{ik_0 z - i\omega t} \,. \tag{1.33}$$

where $w(z)$ and $R(z)$ represent the beam size and the curvature radius of the phase fronts respectively, with z variation given by

$$w(z) = w_0 \sqrt{1 + \left(\frac{z}{z_R}\right)^2} , \tag{1.34}$$

$$R(z) = z \left[1 + \left(\frac{z_R}{z}\right)^2\right] , \tag{1.35}$$

and ϕ_{Gouy} is the Gouy phase shift

$$\phi_{\text{Gouy}} = \arctan \frac{z}{z_R} , \tag{1.36}$$

entirely due to diffraction effects, where

$$z_R = \frac{\pi w_0^2}{\lambda} \tag{1.37}$$

is the Rayleigh length, that is the length at which the beam size is $\sqrt{2}$ times w_0, the beam size at the waist, and λ is the wavelength.
The Gouy phase indicates that as a Gaussian beam passes through a focus, it acquires an additional phase shift of π, in addition to the usual $k_0 z$ phase shift that would be expected from a plane wave.

Comparing (1.30) and (1.33) and including the Gouy term in the amplitude $a(\kappa, x)$, the real and imaginary part of the eikonal are given by

$$S(x, y, z) = \left[z + \frac{x^2 + y^2}{2R(z)}\right] , \tag{1.38}$$

$$\phi(x, y, z) = \kappa^{-1} \frac{x^2 + y^2}{w(z)^2} ,$$

where also the curvature radius R and the beam size w are normalized respect to L like the spatial coordinates, that is $w = w_L/L$ and $R = R_L/L$.

The customary procedure in CGO consists in substituting the electric field ansatz (1.30) into the wave equation (1.1) and then separate the terms according to:

$$|\nabla \phi| \ll |\nabla S| . \tag{1.39}$$

This procedure can be justified and made precise taking into account the QO ordering

$$\lambda \ll w_L \ll L \text{ (or equivalently } 1 \ll \kappa w \ll \kappa) , \tag{1.40}$$

$$\frac{\lambda}{w_L} \sim \frac{w_L}{L} \sim \kappa^{-1/2} .$$

Estimate (1.39) can be readily justified considering for simplicity the non-astigmatic Gaussian beam expression (1.33) for which, neglecting the R and w dependence on the z coordinate, the $|\nabla \phi|/|\nabla S|$ ratio takes the form

$$\frac{|\nabla \phi|}{|\nabla S|} \simeq \kappa^{-1} \frac{2r}{w^2} \left[1 + \frac{r^2}{R^2}\right]^{-1/2} , \tag{1.41}$$

where $r = \sqrt{x^2 + y^2}$. If we consider the space region around the axis of the beam for which r is equal at most to w, we can obtain an upper boundary for the $|\nabla\phi|/|\nabla S|$ ratio taking $r \sim w$, obtaining

$$\frac{|\nabla\phi|}{|\nabla S|} \sim \frac{1}{\kappa w} = \frac{1}{k_0 w_L} \simeq \frac{\lambda}{w_L} \sim \kappa^{-1/2} \ll 1 \,. \tag{1.42}$$

As a consequence the results obtained with this method are valid only in a neighborhood of the beam axis. Moreover, this heuristic approach fails to give a rigorous estimate of the CGO residual of the wave equation.

In this PhD thesis a more rigorous way to take into account the paraxial character of the beam is presented, based on some inequalities obtained by Pereverzev and Maslov, exploited in order to give a rigorous estimate of the CGO residual of the wave equation and to greatly simplify the derivation of the wave energy flux. The obtained results are valid not only in a neighborhood of the beam axis, but in every compact region K in which the electric field has to be reconstructed.

In the next section, the Maslov-Pereverzev inequalities derivation is summarized, properly reformulating them in order to apply to our framework.

1.3 Maslov-Pereverzev estimates

In this section the pivotal inequalities derived by Pereverzev and Maslov in order to take into account the paraxial character of the beam are presented, giving only a sketch of the derivation. For the details of the derivation, we refer to Appendix C.

The module of the electric field, in the CGO framework, is proportional to $e^{-\kappa\phi}$, as follows from Eq. (1.31), that is

$$|E_{\mathrm{CGO}}(\kappa, x)| \propto e^{-\kappa\phi(x)} \,. \tag{1.43}$$

This fact, coupled with the $\mathrm{Im}\psi(x) = \phi(x) \geq 0$ condition on the imaginary part of the eikonal, results, in the $\kappa \to \infty$ limit, in the collapse of the wave on the zero-level set of $\phi(x)$, namely,

$$\mathcal{R} = \{x;\ \phi(x) = 0\} \,. \tag{1.44}$$

We consider the simple case where this set is constituted by a curve given parametrically by $x = \bar{x}(\tau)$. This curve is named "reference ray" in the paraxial WKB theory.
Moreover, we make a further assumption on the form of $\phi(x)$, that is:

$$w \cdot D^2\phi\big(\bar{x}(\tau)\big)w > 0, \tag{1.45}$$

where $[D^2\phi(x)]_{ij} = \partial^2\phi(x)/\partial x^i \partial x^j$ is the Hessian matrix of ϕ, for every vector w linearly independent of the tangent vector $e_t(\tau)$, i.e., the Hessian matrix of the imaginary part of the eikonal function is positive definite for vectors transversal to the reference ray $\mathcal{R}$.
Using this last condition, it is possible to show that in a neighborhood U of $\mathcal{R}$ a vector valued function $\xi(x)$ exists such that $\phi(x)$ can be put in the form

$$\phi(x) = \frac{1}{2}\xi(x)^2 = \frac{1}{2}\delta_{ij}\xi^i(x)\xi^j(x) \,. \tag{1.46}$$

From the fact that Eq. (1.43) holds in all space and Eq. (1.46) holds in a neighborhood U of the reference ray, it is possible to demonstrate that in every compact region K in which the electric field has to be reconstructed, the following inequalities are valid, if ϕ is a sufficiently smooth function:

$$|(\nabla\phi(x))^{\alpha} e^{i\kappa\psi(x)}| \leq C_{\alpha}\kappa^{-|\alpha|/2} , \tag{1.47}$$

where α is a three dimensional multiindex and C_{α} is a constant.

Roughly speaking, Eq. (1.47) implies that every time one multiplies the exponential $e^{i\kappa\psi(x)}$ by any component of $\nabla\phi$, the order is reduced by a factor $1/\sqrt{\kappa}$. As a consequence, in the wave equation, where $e^{i\kappa\psi(x)}$ is a common factor, the order of every term of the wave equation proportional to $(\nabla\phi)^{\alpha}$, with $|\alpha| \neq 0$, is reduced by a factor $\kappa^{-|\alpha|/2}$.

Eq. (1.47), obtained independently by Pereverzev and Maslov, constitutes the major tool adopted in the energy flux derivation presented in this PhD thesis.

1.4 Complex geometrical optics equations and their solution

In this section, the Maslov-Pereverzev inequalities, reviewed in the previous section, are exploited to estimate rigorously the dominant orders of the wave equation expansion in the GO parameter κ, allowing to neglect terms in the κ^{-1} order equation that in the standard formulation of the complex eikonal theory lead to difficulties in the wave energy flux derivation.

The κ^{0} and κ^{-1} order equations, thus obtained, are then solved and the GRAY code equations are rigorously derived.

In the following sections only the results are given, together with a summary of the main steps in their derivation. For a detailed presentation of the ordering of the wave equation and its solution at the dominant orders, we refer to Appendix D.

1.4.1 Wave equation ordering

After substituting the electric field ansatz (1.30), Maxwell's wave Eq. (1.1) takes the form

$$e^{i\kappa\psi}\left[\mathcal{A}(x,\nabla\psi)\kappa^{2} + \mathcal{B}(x,\nabla\psi)\kappa\right] + O(1) = 0 , \tag{1.48}$$

with

$$\mathcal{A}(x,\nabla\psi) \equiv D_0(x,\nabla\psi)a_0(x) , \tag{1.49}$$

$$\begin{aligned}\mathcal{B}(x,\nabla\psi) \equiv{}& D_0(x,\nabla\psi)a_1(x) - i\Big[\frac{\partial D_0}{\partial N_i}(x,\nabla\psi)\frac{\partial a_0}{\partial x^i}(x) \\ &+ \frac{1}{2}\frac{\partial^2\psi}{\partial x^i\partial x^j}(x)\frac{\partial^2 D_0}{\partial N_i\partial N_j}(x,\nabla\psi)a_0(x) - i\varepsilon_1(x)a_0(x)\Big] ,\end{aligned} \tag{1.50}$$

where Eq. (1.7) has been accounted for and $D_0(x,\nabla\psi)$ is the extension of the dispersion tensor D_0, defined in Eq. (1.9), to complex values of the refractive index $\tilde{N} = N + iN'$, evaluated at $\tilde{N} = \nabla\psi$. The same argument applies to the derivatives of D_0.

Equation (1.48) can be simplified taking into account the paraxial character of the beam, using the Pereverzev-Maslov estimates (1.47), reducing it to the form

$$e^{i\kappa\psi}\left[\mathcal{A}(x,\nabla\psi)\kappa^2+\mathcal{B}(x,\nabla S)\kappa\right]+O(\sqrt{\kappa})=0\,, \tag{1.51}$$

where $\mathcal{B}(x,\tilde{N})$ is now evaluated at $N=\nabla S$. The asymptotic expansion (1.51) of the wave equation is solved within an $O(\sqrt{\kappa})$ residual, which corresponds to an error of $\kappa^{-3/2}$ as the leading terms in the wave equation are quadratic in κ.
It is important to note that the imaginary part of the complex phase enters the $O(\kappa)$-term through the Hessian matrix $\partial^2\psi/\partial x^i\partial x^j$ only, fact that will simplify substantially the derivation of the energy flux.

Since (1.51) has to be valid $\forall\kappa$ sufficiently large, the independence of the powers κ^n is now exploited to separate the coefficients of κ^2 and κ that is, dividing Eq. (1.51) by κ^2, the wave equation at the dominant and first order in κ^{-1} becomes:

$$D_0(x,\nabla\psi)a_0(x)=\rho_0(x,\nabla\phi)\,, \tag{1.52}$$

$$\begin{aligned} &D_0(x,\nabla S)a_1(x)-i\left[\frac{\partial D_0}{\partial N_i}(x,\nabla S)\frac{\partial a_0}{\partial x^i}(x)\right. \\ &\left.+\frac{1}{2}\frac{\partial^2\psi}{\partial x^i\partial x^j}\frac{\partial^2 D_0}{\partial N_i\partial N_j}a_0(x)-i\varepsilon_1(x)a_0(x)\right]=\rho_1(x,\nabla\phi)\,, \end{aligned} \tag{1.53}$$

where ρ_0 and ρ_1 are allowed remainders in order to solve eq. (1.51) with the correct O($\sqrt{\kappa}$) residual. ρ_0 and ρ_1 must be at least cubic and linear in $\nabla\phi$, respectively, so that at least:

$$\begin{aligned} e^{-\kappa\phi}\rho_0(x,\nabla\phi)&=O(\kappa^{-3/2})\,,\\ e^{-\kappa\phi}\rho_1(x,\nabla\phi)&=O(\kappa^{-1/2})\,. \end{aligned} \tag{1.54}$$

Let us remark that this is not a perturbative argument in $\nabla\phi$: In general, the remainders are by no means small, except in a narrow strip around the reference ray, where the beam is localized.

1.4.2 Solution of the wave equation at the dominant order: extended rays and rigorous derivation of GRAY equations

Let us consider the dominant order of the wave equation (Eq. (1.52)).

Given a mode relative to the $D_0(x,\nabla S)$ eigenvalue $H(x,\nabla S)$ (and relative eigenvector $e(x,\nabla S)$), eq. (1.52) is solved by a complex eikonal $\psi(x)$ and an amplitude $a_0(x)$ such that

$$\tilde{H}(x,\nabla\psi)=\sigma_0(x,\nabla\phi)\,, \tag{1.55}$$

$$a_0(x)=A(x)\tilde{e}(x,\nabla\psi)\,, \tag{1.56}$$

where $\tilde{H}(x,\tilde{N})$ and $\tilde{e}(x,\tilde{N})$ are the extensions of the eigenvalue and eigenvector to complex values $\tilde{N} = N + iN^{'}$ of the refractive index, defined by

$$\begin{aligned}\tilde{H}(x,\tilde{N}) &= H(x,N) + i\frac{\partial H(x,N)}{\partial N_k}N_k^{'} - \frac{1}{2}\frac{\partial^2 H(x,N)}{\partial N_k \partial N_l}N_k^{'}N_l^{'}\ , \\ \tilde{e}(x,\tilde{N}) &= e(x,N) + i\frac{\partial e(x,N)}{\partial N_k}N_k^{'} - \frac{1}{2}\frac{\partial^2 e(x,N)}{\partial N_k \partial N_l}N_k^{'}N_l^{'}\ ,\end{aligned} \tag{1.57}$$

where $\sigma_0(x,\nabla\phi)$ is an arbitrary remainder, cubic in $\nabla\phi$, and $A(x)$ is an arbitrary complex scalar amplitude.

Eq. (1.55) depends on the arbitrary cubic remainder σ_0, and therefore it does not determine uniquely the complex eikonal ψ. The natural choice $\sigma_0 = 0$ (simplest possible choice) leads to the following set of equations:

$$\mathrm{Re}(\tilde{H})(x,\nabla S) \equiv H_\phi(x,\nabla S) = H(x,\nabla S) - \frac{1}{2}\frac{\partial^2 H(x,\nabla S)}{\partial N_k \partial N_l}\frac{\partial\phi}{\partial x^k}\frac{\partial\phi}{\partial x^l} = 0\ , \tag{1.58}$$

$$\mathrm{Im}(\tilde{H})(x,\nabla S) = \frac{\partial H(x,\nabla S)}{\partial N_k}\frac{\partial\phi}{\partial x^k} = 0\ . \tag{1.59}$$

These equations, called "extended rays equations", were derived by Mazzucato [5]. Hence, we have recovered the standard equations for extended rays, but without the need for the condition $|\nabla\phi| \ll |\nabla S|$. Eq. (1.58) can be solved with the method of characteristics leading to the Hamiltonian equations

$$\frac{dx(\tau)}{d\tau} = \left.\frac{\partial H_\phi(x,\nabla S)}{\partial N}\right|_{H_\phi(x,\nabla S)=0}\ , \tag{1.60}$$

$$\frac{dN(\tau)}{d\tau} = -\left.\frac{\partial H_\phi(x,\nabla S)}{\partial x}\right|_{H_\phi(x,\nabla S)=0}\ . \tag{1.61}$$

From (1.59) we see that ϕ is constant along the vector field

$$V(x) = \frac{\partial H}{\partial N}(x,\nabla S(x))\ , \tag{1.62}$$

while (1.60) implies that the extended rays have the tangent vector

$$V_\phi(x) = \frac{\partial H_\phi}{\partial N}(x,\nabla S(x)) = V(x) - \frac{1}{2}\frac{\partial\phi}{\partial x^k}\frac{\partial\phi}{\partial x^l}\frac{\partial^3 H}{\partial N \partial N_k \partial N_l}(x,\nabla S)\ . \tag{1.63}$$

Equations (1.58) and (1.59) can be summarized:

$$\begin{aligned}&H_\phi(x,\nabla S) = 0\ , \\ &V(x)\cdot\nabla\phi = 0\ .\end{aligned} \tag{1.64}$$

A special case of particular interest is that of Hamiltonians depending quadratically on momenta. Since the third derivatives $\partial^3 H/\partial N_i \partial N_j \partial N_k$ vanish identically, one has $V(x) = V_\phi(x)$ and ϕ is constant along extended rays. As an example, this is the case for vacuum and isotropic spatially non-dispersive media. Eq. (1.60), (1.61) and (1.59) take

the form

$$\frac{dx}{d\tau} = V_\phi\Big|_{H_\phi=0} , \tag{1.65}$$

$$\frac{dN}{d\tau} = -\frac{\partial H_\phi}{\partial x}\Big|_{H_\phi=0} , \tag{1.66}$$

$$V \cdot \nabla\phi = 0 . \tag{1.67}$$

In general, $\nabla\phi$ is small near the zero-level set $\mathcal{R}$ where the field is localized and the two vector fields are close one to the other, although differences can be present away from $\mathcal{R}$.

For an efficient numerical implementation of extended ray equations, the conservation of ϕ along rays is a major simplification. Fortunately, properly choosing the remainder σ_0 in eq. (1.55) an alternative set of equation can be derived, in which the imaginary part of the phase ϕ is conserved along V_ϕ, that is along the extended rays. Specifically, we can set

$$\sigma_0(x, \nabla\phi) = \frac{i}{2}\frac{\partial^3 H(x, \nabla S)}{\partial N_i \partial N_j \partial N_k}\frac{\partial\phi}{\partial x^i}\frac{\partial\phi}{\partial x^j}\frac{\partial\phi}{\partial x^k} , \tag{1.68}$$

which is cubic in $\nabla\phi$ as required. Then, after the separation of the real and imaginary parts, Eq. (1.55) takes the form

$$H_\phi(x, \nabla S) = 0 , \tag{1.69}$$

$$V_\phi(x) \cdot \nabla\phi = 0 . \tag{1.70}$$

In this form, extended rays are still determined by the Hamiltonian H_ϕ but now ϕ is exactly conserved by the extended ray flow. This provides a rigorous justification of the algorithm used in GRAY, which actually solves system (1.69)-(1.70).

1.4.3 Solution of the first order wave equation: amplitude transport

Let us consider the κ^{-1} order wave equation (Eq. (1.53)).

It can be shown, after a lengthy but straightforward derivation (cf. Appendix D.1.3), that Eq. (1.53) can be manipulated obtaining the CGO amplitude transport equation in the form

$$V(x) \cdot \nabla A(x) - [-\gamma_1(x) + i(\delta_1(x) - \delta_{\text{Gouy}}(x)) - \frac{1}{2}\nabla \cdot V(x)]A(x) = \sigma_1(x, \nabla\phi) , \tag{1.71}$$

where γ_1 and δ_1 are formally given by (1.19) and (1.20), respectively. Equation (1.71) is formally equivalent to GO equation (1.17). In complex eikonal theory, however, an additional phase shift is found, namely,

$$\delta_{\text{Gouy}} = \frac{1}{2}\frac{\partial^2 H(x, \nabla S)}{\partial N_k \partial N_l}\frac{\partial^2\phi}{\partial x^k \partial x^l} , \tag{1.72}$$

which is the generalization of the classical Gouy shift (1.36) and it is entirely due to diffraction effects. Again, an arbitrary remainder $\sigma_1(x, \nabla\phi)$ is allowed, which must be at least linear in $\nabla\phi$. Equation (1.71) describes the transport of the amplitude A that was left unspecified in Eqs. (1.56).

As for Eq. (1.55), the actual calculation of the amplitude depends on the choice of the remainder σ_1.
The natural choice $\sigma_1 = 0$ gives the amplitude transport equation

$$V \cdot \nabla A = [-\gamma_1 + i(\delta_1 - \delta_{\text{Gouy}}) - \frac{1}{2}\nabla \cdot V]A \,, \tag{1.73}$$

describing the transport of the amplitude along the field lines of the vector $V(x)$. This is formally the same as the standard geometrical optics transport Eq. (1.17), the only difference coming from the function S. In this case, the amplitude is not transported along extended rays.
The transport equation of the amplitude along the extended rays can be easily obtained with the following choice of the remainder:

$$\sigma_1 = (V - V_\phi) \cdot \nabla A + \frac{1}{2}\nabla \cdot (V - V_\phi)A \,. \tag{1.74}$$

This is at least linear in $\nabla\phi$ as required, as one can see by direct calculation:

$$\begin{aligned}\sigma_1 = &\underbrace{\frac{1}{2}\frac{\partial^3 H}{\partial N_k \partial N_l \partial N_n}\frac{\partial\phi}{\partial x^l}\frac{\partial\phi}{\partial x^n}\frac{\partial A}{\partial x^k}}_{O(|\nabla\phi|^2)} + \underbrace{\frac{1}{4}\frac{\partial}{\partial x^k}\left[\frac{\partial^2 H}{\partial N_l \partial N_n}\right]\frac{\partial\phi}{\partial x^l}\frac{\partial\phi}{\partial x^n}A}_{O(|\nabla\phi|^2)} \\ &+ \underbrace{\frac{1}{2}\frac{\partial^2 H}{\partial N_l \partial N_n}\frac{\partial\phi}{\partial x^k \partial x^l}\frac{\partial\phi}{\partial x^n}A}_{O(|\nabla\phi|)} \,,\end{aligned} \tag{1.75}$$

where the symmetry of $\partial^2 H/\partial N_l \partial N_n$ was taken into account and it was recalled that $\phi = \phi(x)$, $A = A(x)$ and $H = H(x, \nabla S)$. With the choice (1.74) of the remainder, the amplitude transport equation along the extended rays (along V_ϕ) is obtained:

$$V_\phi \cdot \nabla A = [-\gamma_1 + i(\delta_1 - \delta_{\text{Gouy}}) - \frac{1}{2}\nabla \cdot V_\phi]A \,, \tag{1.76}$$

that is the same as (1.73) with the substitution $V \to V_\phi$.

We shall see in section 1.5 that the energy fluxes obtained from Eqs. (1.73) and (1.76) tend to the same limit $\kappa \to \infty$, but they are different for finite values of κ.

1.4.4 Complex geometrical optics estimate of the residual

It can now be formulated the main result of the foregoing asymptotic construction as an estimate of the residual in the wave equation.

Once Eq. (1.71) has been solved for the amplitude $A(x)$, it can be proven that the algebraic equation for a_1 has a solution. As usual, such solution is never computed in practice, but its existence is important because it will be used in the following important statement.

Let $\psi = S + i\phi$ be a regular solution of Eq. (1.55), and let a_0 be given in (1.56), with

$A(x)$ a regular solution of the complex geometrical optics transport Eq. (1.71). Then, it is possible to find a corrector a_1 such that the complex eikonal wave

$$E_{CGO,1}(\kappa, x) = (a_0(x) + \kappa^{-1} a_1(x)) e^{i\kappa\psi(x)} \tag{1.77}$$

solves the wave Eq. (1.1) for the electric field within an error,

$$|\kappa^{-2}\nabla \times \nabla \times E_{\mathrm{CGO},1}(\kappa, x) - \epsilon(\kappa, x) E_{\mathrm{CGO},1}(\kappa, x)| \leq \kappa^{-3/2} \, . \tag{1.78}$$

Eq. (1.78) is the explicit form of the big O notation implicit in Eq. (1.51) (divided by κ^2). This estimate relies on the existence of regular solutions for the complex eikonal ψ and the amplitude A. On the other end, the coupling of the real phase S to the imaginary part ϕ successfully removes caustic singularities, at least, for the case of focalized beams. At last, the residual estimate (1.78) does not depend on the choice of the remainders σ_i, $i = 0, 1$, in Eqs. (1.55) and (1.71).

1.5 Wave energy flux

In this section our principal goal is described, that is the derivation of the approximated wave energy flux in the CGO framework. Moreover, it will be shown that the extended rays computed in the GRAY code represent the energy flow within the CGO approximation.

The details of the derivation of the presented results for the standard CGO formulation ($\sigma_0 = \sigma_1 = 0$) are available in Appedix D.2.

It can be shown that the time-averaged Poynting vector

$$\langle S \rangle = \frac{c}{8\pi} (E^* \times B) \, , \tag{1.79}$$

after eliminating B (Faraday Maxwell Eq.) and substituting the CGO electric filed ansatz (1.31), becomes

$$\langle S \rangle(\kappa, x) = v_g(x) W_{\mathrm{CGO}}(x) + O(1/\sqrt{\kappa}) \, , \tag{1.80}$$

with $W_{\mathrm{CGO}}(x)$ formally given by

$$W_{\mathrm{CGO}}(x) = e^{-2\kappa\phi(x)} W_{\mathrm{GO}}(x) \, , \tag{1.81}$$

where v_g is formally equivalent to (1.26) and the W_{GO} expression is given in (1.27).
As a consequence, at the dominant order, the only difference between the CGO wave energy flux and the GO one is a factor $e^{-2\kappa\phi(x)}$, that in CGO controls the localization of the beam around the reference ray.

Let us consider for simplicity the natural formulation of CGO ($\sigma_0 = \sigma_1 = 0$).
The energy transport equation can be obtained multiplying Eq. (1.73) by A^* and taking the real part of the result, taking into account Eq. (1.67), resulting in

$$\nabla_r \cdot [v_g W_{\mathrm{CGO}}] = -\gamma W_{\mathrm{CGO}} \, , \tag{1.82}$$

where the dimensional units have been restored, with an energy absorption coefficient γ formally equivalent to GO expression (1.28). As was expected, the argument of the

divergence at the LHS of Eq. (1.82) is the dominant order term of Eq. (1.80).
By noting that $v_g \propto V$, one can conclude that, with the natural choice of both remainders σ_i, the wave energy density flow is approximated by the flow of the vector field $V = \partial H(x, \nabla S)/\partial N$, and this can deviate from the corresponding geometrical optics quantity, due to diffraction effects. In general, the vector field V is not tangent to extended rays.

The mismatch between the approximated wave energy flow and the extended ray flow is removed in the optimized form of extended ray Eqs. (1.69)-(1.70) complemented with the transport Eq. (1.76). One can check that the above calculation holds true for the optimized formulation as well, yielding the energy transport equation in the form (1.82) with the substitution $v_g \to v_{g\phi}$, with the group velocity $v_{g\phi}$ given by

$$v_{g\phi} = c \left| \frac{\partial(\omega H)}{\partial \omega} \right|^{-1} V_\phi \,, \tag{1.83}$$

that is the same as v_g with V substituted by V_ϕ. In this formulation the energy flow is directed along the extended rays. This result shows that extended rays computed according to (1.69) provide an approximation of the energy flow of the complex geometrical optics solution. Let us remark that the energy continuity equation with either (1.26) or (1.83) is proven by making use of the condition $V \cdot \nabla\phi = 0$ and $V_\phi \cdot \nabla\phi = 0$, respectively. Therefore, the form (1.26) of the group velocity is appropriate to the standard formulation (Eq. (1.58) and Eq. (1.59)), while the form (1.83) is appropriate to the optimized formulation (Eq. (1.69) and Eq. (1.70)) and they cannot be exchanged.

In order to complete our analysis, we shall now show that, in both formulations, the quantity Wv_g converges to the same limit for $\kappa \to \infty$, as it should be, despite the vector field v_g is independent on κ. Then, we shall see that in both cases, Wv_g approximates the Poynting flux corresponding to the complex eikonal wave field.
The first claim is readily proven. In fact, in the $\kappa \to \infty$ limit, the energy density is non vanishing only on the reference ray, where $V(x)$ and V_ϕ coincide, because $\phi(x) = 0$. More precisely, given a complex eikonal $\psi = S + i\phi$, computed by either of the two formulations, let us consider the vector fields $V(x)$ and $V_\phi(x)$ computed via Eqs. (1.62) and (1.63) with the same complex eikonal ψ. Then estimate (1.47) implies that

$$|(V(x) - V_\phi(x))e^{-2\kappa\phi}| \leq C/\kappa \,, \tag{1.84}$$

where $C > 0$ is a generic constant. In fact, from (1.63), it follows that

$$\begin{aligned} |(V - V_\phi)e^{-2\kappa\phi}| &= \left| \sum_{k,l} \left(\frac{1}{2} \frac{\partial^3}{\partial N \partial N_k \partial N_l} \right) \left(\frac{\partial \phi}{\partial x^k} e^{-\kappa\phi} \right) \left(\frac{\partial \phi}{\partial x^l} e^{-\kappa\phi} \right) \right| \\ &\leq \sum_{k,l} \underbrace{\left| \frac{1}{2} \frac{\partial^3}{\partial N \partial N_k \partial N_l} \right|}_{O(1)} \underbrace{\left| \frac{\partial \phi}{\partial x^k} e^{-\kappa\phi} \right|}_{a} \underbrace{\left| \frac{\partial \phi}{\partial x^l} e^{-\kappa\phi} \right|}_{b} \,. \end{aligned} \tag{1.85}$$

where for clarity the summation notation is written explicitly, and the a,b terms can be evaluated using the Pereverzev-Maslov estimate ($a = O(\kappa^{-1/2})$, $b = O(\kappa^{-1/2})$), leading to (1.84).
Now the second claim, that is the fact that in the two formulations Wv_g approximates

the Poynting flux, follows from a comparison between Eq. (1.80) and Eq. (1.84). In Eq. (1.80) we notice that the order of the error term is larger than the order of the difference $(V - V_\phi)e^{-2\kappa\phi}$. Therefore, Eq. (1.80) holds true for v_g given by (1.83) as well.

Concluding, both formulations give an approximation of the wave energy flux of the same order in the limit $\kappa \to \infty$. The optimized formulation used in GRAY has the computational advantage that extended rays represent the approximated energy flow.

These new results, that constitute the major goal of my PhD, fill the gap in literature about the CGO derivation of the wave energy flux, showing as a corollary that the optimized extended rays (GRAY rays) describe the energy flow within the CGO approximation.

CHAPTER 2

The wave energy flux in CGO: numerical results

In this section the theoretical results about the wave energy flux in complex geometrical optics framework, reported in the previous chapter, are illustrated numerically for the case of electron cyclotron beams propagation in tokamak plasmas by using the GRAY code [6], which is based upon the complex eikonal theory. The results are compared to those of the paraxial beam tracing code TORBEAM [7], which provides an independent calculation of the energy flow.

Two numerical tests are reported in order to illustrate the theoretical results. The first consists in comparing the fields V and V_ϕ, defined in Eqs. (1.62) and (1.63) respectively, along the extended rays (V_ϕ rays), using the GRAY code, while the second consists in comparing the extended rays, generated by GRAY code, with the wave energy flux rays (V rays), generated by the paraxial WKB code TORBEAM. In section 1.5 it was pointed out that the difference $V - V_\phi$ weighted with the exponential $e^{-2\kappa\phi}$ vanishes for $\kappa \to \infty$. This formal result just means, for large but finite values of κ, that the two vector fields are close to each other near the reference ray $\mathcal{R}$ where the field is localized. These two numerical experiments allow us to estimate their difference for realistic values of physical parameters.

Henceforth for brevity we will turn to dimensional quantities without adding subscripts, that is the notation will change respect to the previous chapter according to: $Lx \to x$ and $\nabla/L \to \nabla$. Similarly the eikonal $\psi = S + i\phi$ will have the dimensions of a length, that is the electric field will be in the form

$$E \propto e^{ik_0\psi - i\omega t} \tag{2.1}$$

instead of

$$E \propto e^{i\kappa\psi - i\omega t}\,, \tag{2.2}$$

where we recall that $\kappa = k_0 L$. As a consequence $L\psi \to \psi$.

2.1 Comparison of extended rays and wave energy flux direction in GRAY

The GRAY code solves the set of equations (1.65), (1.66), (1.70), with effective Hamiltonian H_ϕ given by the real part of the complex extension of

$$H(x, N) = N^2 - n^2(x, N_\parallel)\,, \tag{2.3}$$

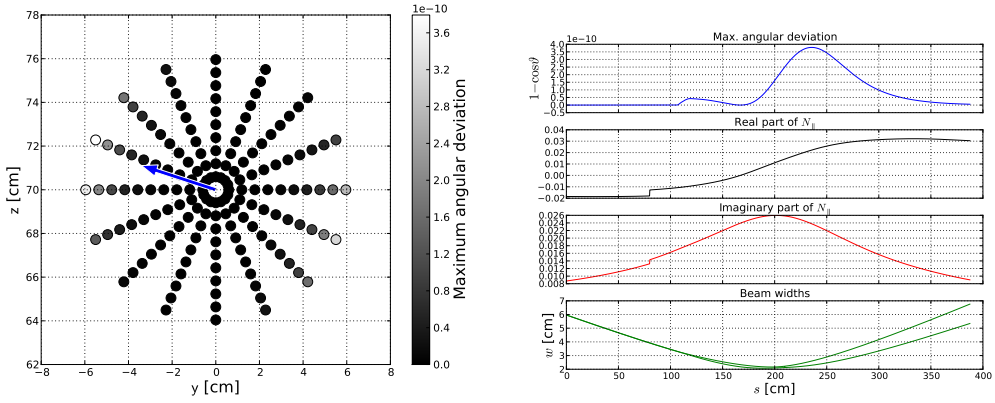

Figure 2.1: Angular deviation $1 - \cos\theta$ of extended rays, cf. Eq. (2.4), as computed by the GRAY code. The left panel shows the initial positions of extended rays, projected on the y-z plane. The gray level of each point encodes the maximum deviation observed along the corresponding ray, and the approximate direction of the equilibrium magnetic field is indicated by an arrow. The right panel shows the profile of the deviation for the "worst ray", compared to both the real and imaginary parts of the parallel refractive index, as well as to the two beam widths (defined as the widths of the elliptical e^{-2}-intensity contour in the beam cross-section). In this case, the equivalent focal length in free space is $d_0 = 200$ cm and the equivalent width at the waist in free space is $w_0 = 2$ cm. The poloidal and toroidal injection angles, defined on page xvii of the introduction, are $\alpha = 0^\circ$ and $\beta = 0^\circ$, respectively. The discontinuity in the parallel refractive index is due to the way the equilibrium magnetic field has been extended outside the numerical grid, in the vacuum region (we set $b = e_\phi$ outside the grid, e_ϕ being the unit vector in the toroidal direction). The Cartesian components of the refractive index are actually continuous. The initial positions of rays are given on a plane orthogonal to the injection direction, thus their projections on the x-y plane depend on the angle β.

where $n^2(x, N_\parallel)$ is obtained solving the Altar-Appleton-Hartree dispersion relation for high-frequency waves in cold magnetized plasmas and $N_\parallel$ is the real parallel refractive index component in the direction of the local equilibrium magnetic field.
For details on the GRAY code we refer to Appendix E.

In this simulation the GRAY code was slightly modified in order to compute the values of the $V(x)$ field at all the iterated points of the extended rays, and in particular the angle θ between $V(x)$, in the energy flux direction in the natural CGO formulation, and $V_\phi(x)$, tangent to the extended rays, defined by

$$\cos\theta = v(x) \cdot v_\phi(x) \,, \tag{2.4}$$

where $v(x) = V(x)/|V(x)|$ and $v_\phi(x) = V_\phi(x)/|V_\phi(x)|$.

Figures 2.1-2.4 show the results for four cases of non-astigmatic electron cyclotron beams, launched from the equatorial plane in ITER considering a typical ITER scenario at the end of the plasma current flat-top phase. Two types of beam are considered: the first with a mild focalization similar to ITER operational parameters, i.e., with an equivalent waist in free space $w_0 = 2$ cm and an equivalent waist distance from the antenna $d_0 = 2$ m; the second with a very high focalization ($w_0 = 0.5$ cm, $d_0 = 1.5$ m). Such a highly focused beam largely exceeds ITER parameters, but it has been considered as an example

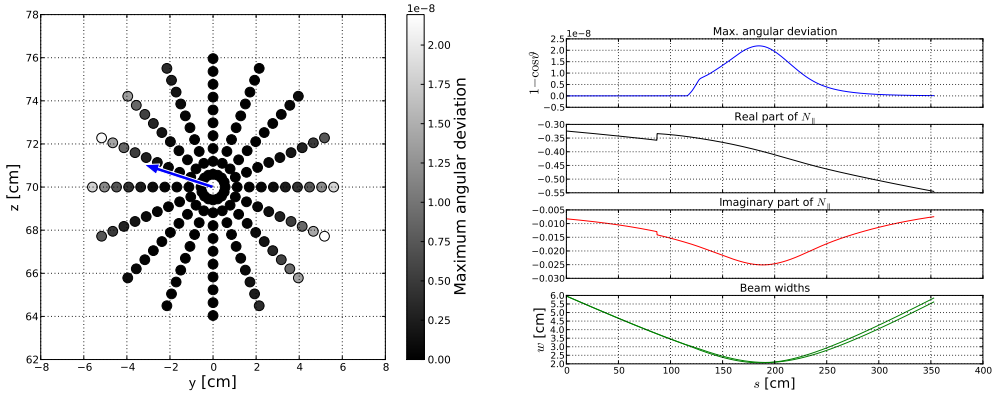

Figure 2.2: The same as in Fig. 2.1,but for $z_f = 200$ cm, $w_0 = 2$ cm, $\alpha = 0^\circ$, and $\beta = 20^\circ$.

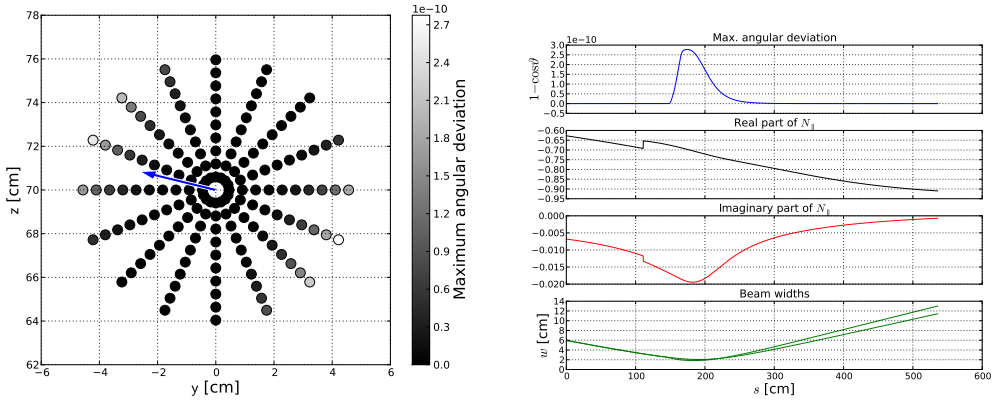

Figure 2.3: The same as in Fig. 2.1,but for $z_f = 200$ cm, $w_0 = 2$ cm, $\alpha = 0^\circ$, and $\beta = 40^\circ$.

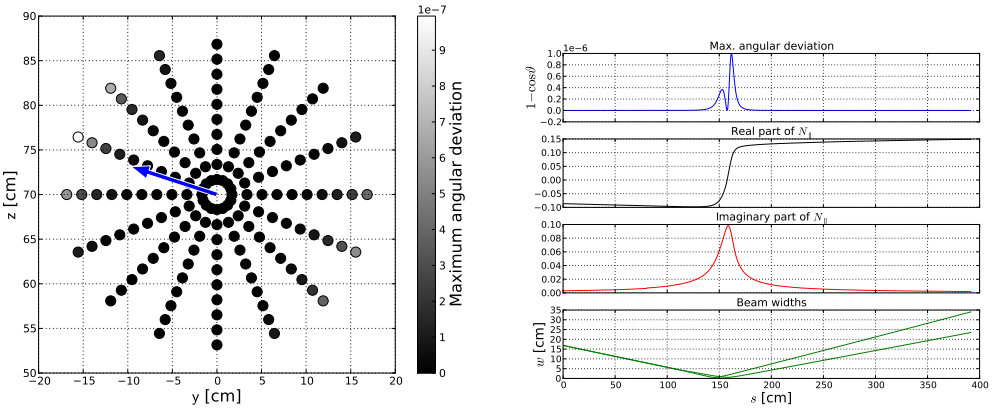

Figure 2.4: The same as in Fig. 2.1,but for $z_f = 150$ cm, $w_0 = 0.5$ cm, $\alpha = 0^\circ$, and $\beta = 0^\circ$.

Type of beam	x(m)	y(m)	z(m)	w_0(m)	d_0(m)	w(m)	R_c(m)
ITER-like	9.3	0	0.7	0.02	2	0.05959	-2.25389
Super-focalised	9.3	0	0.7	0.005	1.5	0.168475	-1.50132

Table 2.1: Launching coordinates and beam parameters for the two types of beam used in the simulations. x, y, z are the mirror coordinates in the laboratory frame, w_0 is the vacuum-equivalent waist size, d_0 is the vacuum-equivalent waist distance from the mirror, w is the beam size at the mirror and R_c is the curvature radius at the mirror.

in which the effects of diffraction are emphasized. The launching coordinates and the beam parameters are summarized in table 2.1.

The results for three Toroidal injection angles are shown for the mild-focused beam ($\beta = 0°, 20°, 40°$, Figures 2.1 to 2.3), while only the $\beta = 0°$ propagation is illustrated for the super-focused beam (Figure 2.4). Both the mild-focused and the super-focused beam are injected with null poloidal injection angle α. The poloidal and toroidal injection angles α and β are defined on page xvii of the introduction.
The left panels of Figures 2.1-2.4 show the initial positions of extended rays projected in the y-z plane. For this test, a large number of rays are considered, so that the beam is covered up to the e^{-4}-level of its amplitude, a much larger beam section than usually needed. Each point is represented in a gray scale, which encodes the maximum value of the angular deviation $1 - \cos\theta$, with θ given in (2.4), observed along the ray issued from that point. The approximate direction of the local magnetic field in the low-field side projected onto the y-z plane is indicated by an arrow (this is approximated by the value of the numerical equilibrium magnetic field at the nearest grid node to the launching point, specifically, at major radius coordinate $R = 850$ cm and vertical coordinate $z = 70.3125$ cm of the numerical grid). For each case of Figures 2.1-2.4, we have selected the "worst ray", i.e., the ray for which the maximum angular deviation is observed, and the corresponding profile of $1 - \cos\theta$ is plotted (right panels) as a function of the arc-length s along the central ray, which is used as a common parameter for all rays. The profiles of both the real and imaginary parts of the parallel refractive index (for convenience we have introduced the notation $N^{'} = \nabla\phi$ for the imaginary part of the refractive index, so that $N_{\|}^{'} = b \cdot \nabla\phi$), as well as the profiles of the two beam widths are also reported for a comparison. It is worth noting that, even if we considered beams that are non-astigmatic at the antenna, the plasma anisotropy makes them astigmatic and also introduces a slight rotation. The beam widths in particular are computed according to the standard definition for Gaussian beams, for which the intensity contours in the beam cross-section are ellipses. The widths are then defined as the length of the semi-axis of the e^{-2}-intensity contour.

The distribution of angular deviations (left panels of Figures 2.1-2.4) allows us to appreciate geometric effects. In all considered cases, rays for which the angular deviation attains its minimum are those with initial displacement with the beam axis in the direction perpendicular to the local magnetic field direction. This can be understood by inspection of the effective Hamiltonian H_ϕ (E.2). Let us consider the Appleton-Hartree expression solution for the refractive index, that is

$$n^2(x, N_\|) = 1 - X(x)^2 - X(x)Y(x)^2 \frac{1 + N_\|^2 \pm \Delta(x, N_\|)}{2(1 - X(x) - Y(x)^2)} , \tag{2.5}$$

with

$$\Delta(x, N_\parallel) = \sqrt{(1 - N_\parallel^2)^2 + 4N_\parallel^2 \frac{1 - X(x)}{Y(x)^2}} \,, \tag{2.6}$$

where $X(x) = \omega_p(x)^2/\omega^2$ is the square of the ratio between the electron plasma frequency and the wave frequency, $Y(x) = \Omega_e(x)/\omega$ is the ratio between the electron cyclotron frequency and the wave frequency. The $+, -$ signs refer to the extraordinary (XM) and ordinary (OM) mode, respectively.
From (E.2) it is worth noting that the difference $H_\phi - H$ depends only on the parallel part of the refractive index, and so the difference between V_ϕ and V can be computed as

$$V_\phi - V = \frac{\partial(H_\phi - H)}{\partial N} = \frac{\partial(H_\phi - H)}{\partial N_\parallel} b = \left[\frac{1}{2}(N_\parallel^{'})^2 \frac{\partial^3 n^2}{\partial N_\parallel^3}\right] b \,, \tag{2.7}$$

with

$$\frac{\partial^3 n^2}{\partial N_\parallel^3}(x, N_\parallel) = \pm 24 N_\parallel (1 - N_\parallel^4) \frac{X(x)(1 - X(x))}{Y(x)^2 \Delta(x, N_\parallel)^5} \,, \tag{2.8}$$

where b is the magnetic field unit vector. In our simulations we considered ordinary mode propagation, and therefore the plus sign has to be taken in (2.5). First of all we notice that, since $|V_\phi - V| \propto (N_\parallel^{'})^2$ and the imaginary part of the refractive index assumes its maximum values around the waists, then the deviations take their peak values near the waists too, as can be seen in the right panels of Figures 2.1-2.4 for the rays with maximum deviation within each beam. This fact was expected, because near the waists the diffraction effects are more important.
Let us now turn to the $N_\parallel$ dependence. The asymptotic behavior of $V_\phi - V$ for $N_\parallel \to 0$ is given by

$$V_\phi - V \sim \left[f N_\parallel (N_\parallel^{'})^2\right] b \,, \tag{2.9}$$

where f depends only on the space coordinates:

$$f(x) = 12 \frac{X(x)(1 - X(x))}{Y(x)^2} \,. \tag{2.10}$$

In the launching cases with null toroidal angle (Figures 2.1 and 2.4), the beams are injected toward the axis of the torus, intersecting the magnetic field surfaces nearly perpendicularly ("perpendicular propagation"). Since the beams are paraxial, the parallel refractive indexes of the rays are very small, so that the $V_\phi - V$ difference is in good agreement with (2.9) (The rays with the larger $1 - \cos\theta$ deviation satisfy $N_\parallel \in [-0.02, 0.04]$ and $N_\parallel \in [-0.1, 0.15]$ for the mild-focalized and super-focalized beam respectively). As a consequence, rays with a large $N_\parallel (N_\parallel^{'})^2$ product show larger deviations. Since the overall rotation of the beam can be neglected and the direction of the magnetic field does not vary too much during the propagation, from the left panel of Figures 2.1 and 2.4 it can be noticed that rays with initial displacement from the beam axis in the direction of the magnetic field (indicated by a blue arrow) show larger deviations. It is a consequence of the fact that during the focalization, apart from the region near the waists, they have a non vanishing parallel component of the refractive index. The rays that initially have a displacement from the beam axis that lies in the plane perpendicular to the local direction of the magnetic field have almost null parallel refractive index during the propagation and show negligible deviations.

Moreover, for perpendicular propagation, all the beam rays have a vanishing parallel component of the refractive index in the region near the waists, and this fact is reflected in a double-peak structure of the $1 - \cos\theta$ deviation profile, as can be seen in the right panels of Figures 2.1 and 2.4. The local minimum is found near the waists, where $N_\parallel$ is zero.

The geometrical interpretation of the results is more difficult for propagation with non-null toroidal launching angle ($\beta \neq 0$). While it continues to be true that rays with initial displacement orthogonal to the magnetic field direction show negligible deviations, rays with initial displacement with non vanishing component in the direction of B access a region of the $N_\parallel$ range distinct from the neighborhood of zero (the rays with the larger $1 - \cos\theta$ deviation satisfy $N_\parallel \in [-0.55, 0.30]$ and $N_\parallel \in [-0.95, 0.60]$ for the $\beta = 20°$ and $\beta = 40°$ case respectively), in which the approximation (2.9) no longer applies. In those $N_\parallel$ parameter regions the difference $V_\phi - V$ is no more simply proportional to $N_\parallel$, as it can be seen in Fig. 2.5, where the behavior of $g(N_\parallel, X)|_Y \equiv \partial^3 n^2/\partial N_\parallel^3(N_\parallel, X)|_Y$ (cf. (2.7) and (2.8)) in the $\beta = 40°$ case is shown for four values of Y extracted in the typical range $[0.5, 1.5]$, with X in the typical range $[0.3, 0.6]$. Nonetheless, the "worst rays" remain those initially displaced in the magnetic field direction, as it can be seen in the left panels of Figures 2.2 and 2.3. Moreover, the double-peak in the $1-\cos\theta$ deviation profile is removed, because the $N_\parallel = 0$ neighborhood is never reached.

In passing, let us mention that the slight discontinuity in the profiles of both the real and imaginary parallel refractive indices is due to the way the equilibrium magnetic field has been extended outside the numerical grid. There, the propagation happens in free space, and the ray trajectories do not depend on the magnetic field. We have set $b = e_\phi$ for the calculation of parallel refractive indices outside the grid, where e_ϕ is the unit vector in the toroidal direction. This choice does not match continuously to the numerical equilibrium at the boundary of the grid. The Cartesian components of the refractive index are actually continuous.

The overall conclusion from Figures 2.1-2.3 is that, under ITER-relevant conditions, the angular deviation of the two vector fields V and V_ϕ in the region of space spanned by the rays is small, i.e., of the order comparable to $\sqrt{\epsilon_{\mathrm{mach}}}$ where ϵ_{mach} is the machine precision. Similar results are found for the highly focused beam of Figure 2.4, for which diffraction effects are stronger.
The good agreement of velocity fields as computed by GRAY confirms the theoretical estimate of the difference (1.84) for finite values of κ. This result alone however does not allow us to draw any conclusion on the approximation of the energy flow. In fact, the GRAY code uses the optimized form (1.69) of extended ray equations, hence the vector V, computed here formally as $V(x) = \partial H/\partial N(x, \nabla S(x))$, does not correspond exactly to V shown in (1.26), because in this numerical experiment $\nabla S(x)$ is calculated using $S(x)$ obtained solving (1.69)-(1.70), while the energy flux (1.26) is written considering $S(x)$ obtained solving (1.64). Moreover, the integral lines of two vector fields might exhibit differences even when the vector fields themselves are very similar.

In section 2.2 a more quantitative estimate of the difference between the approximations of the wave energy flow will be supplied.

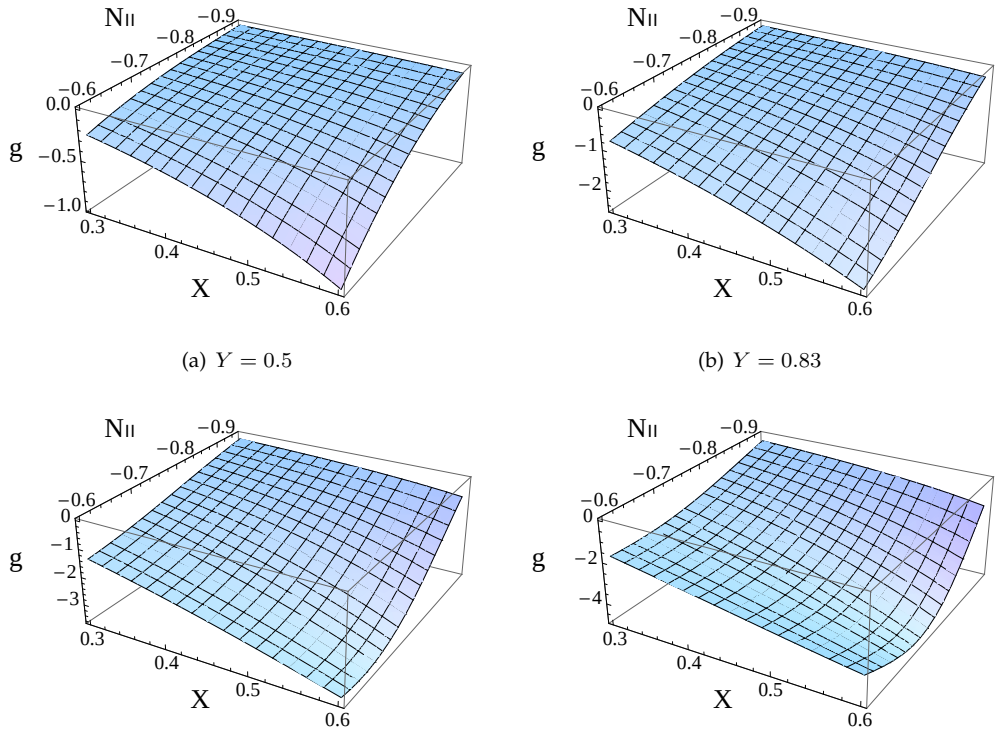

(a) $Y = 0.5$

(b) $Y = 0.83$

(c) $Y = 1.17$

(d) $Y = 1.5$

Figure 2.5: $g(N_\parallel, X)|_Y \equiv \partial^3 n^2 / \partial N_\parallel^3 (N_\parallel, X)|_Y$ graphs versus $N_\parallel$ and $X = \omega_p^2/\omega^2$, relative to four values of $Y = \Omega_e/\omega$.

2.2 GRAY extended rays versus TORBEAM paraxial WKB energy flux

This simulation has been performed in order to have an account of the global differences between the field lines of V_ϕ and V. The paraxial WKB code TORBEAM has been used to compute the V rays. This is made possible by a recently added module, which solves the set of ordinary differential equations

$$\frac{dx}{d\tau} = V(x) \,, \tag{2.11}$$

where $V(x)$ is defined by (1.62), with the real phase S being here computed in the paraxial WKB framework. In this framework, Eq. (1.55), Taylor-expanded around the reference ray, yields the matrix Riccati equation for the Hessian of the phase of the paraxial WKB method. This shows that the paraxial WKB solution for both the real part $S(x)$ and the imaginary part $\phi(x)$ of the complex eikonal is a good approximation of the corresponding quantities computed directly via the standard extended ray Eqs. (1.64). This argument is referred to as Gaussian limit of complex geometrical optics. In this limit, the paraxial WKB calculation of flow of V yields a good approximation of the energy flow obtained in the standard extended ray theory from the group velocity (1.26). We refer to the TORBEAM solution of Eq. (2.11) as TORBEAM rays, for simplicity.

Figure 2.6 (top) shows a qualitative comparison between the extended rays computed by GRAY and TORBEAM, with initial conditions given by the initial position of GRAY rays. The case considered is the same as that of Figure 2.1, with focusing typical for ITER parameters. The beams are described by bundles of rays up to the e^{-2}-level of the amplitude only, and the projection of the outer rays of both GRAY and TORBEAM beams into the x-z poloidal plane (left) and into the y-z plane (right) are shown. The common initial positions of rays are marked by dots. GRAY and TORBEAM rays propagate following each other with high precision up to the waist of the beam, where the diffraction effects become no more negligible. From here they start to slightly deviate from each other, but even after a long propagation length however (in 2.6 (top-left) figure the x-axis scale is very different from that of the z-axis), the cumulative effects of such differences are much smaller than the beam width. In Figure 2.6 (bottom) this comparison has been repeated for the highly focused case of Figure 2.4. In this case the beam width at the beginning and the end of the propagation is one order of magnitude larger that in the previous case and the waist is much smaller due to the strong focusing. Therefore the diffraction effects are stronger and the deviations between the GRAY and TORBEAM rays are larger. Nonetheless, the deviations of the rays are still smaller than the beam width.

The distances between GRAY rays and TORBEAM rays can be computed as follows. For each GRAY-TORBEAM couple of corresponding rays (that is rays with the same initial conditions), the distance is computed as the maximum distance between points on the rays at the same value of the archlength s, that is

$$d = \max_s [\mathrm{dist}(x_{\mathrm{GRAY}}(s), x_{\mathrm{TORBEAM}}(s))] \,. \tag{2.12}$$

Fig. 2.7 shows the distance between points at the same archlength s versus s, for the two GRAY-TORBEAM couples of rays with largest deviations. The left picture refers to the mildly focused beam, while the right picture to the highly focused beam. It is worth noting that in the highly focused case the diffraction effects are important in a narrow neighborhood of the waists, so that the distance (2.12) grows nearly linearly once the rays are moved away from the waists. In order to estimate the maximum deviation, for

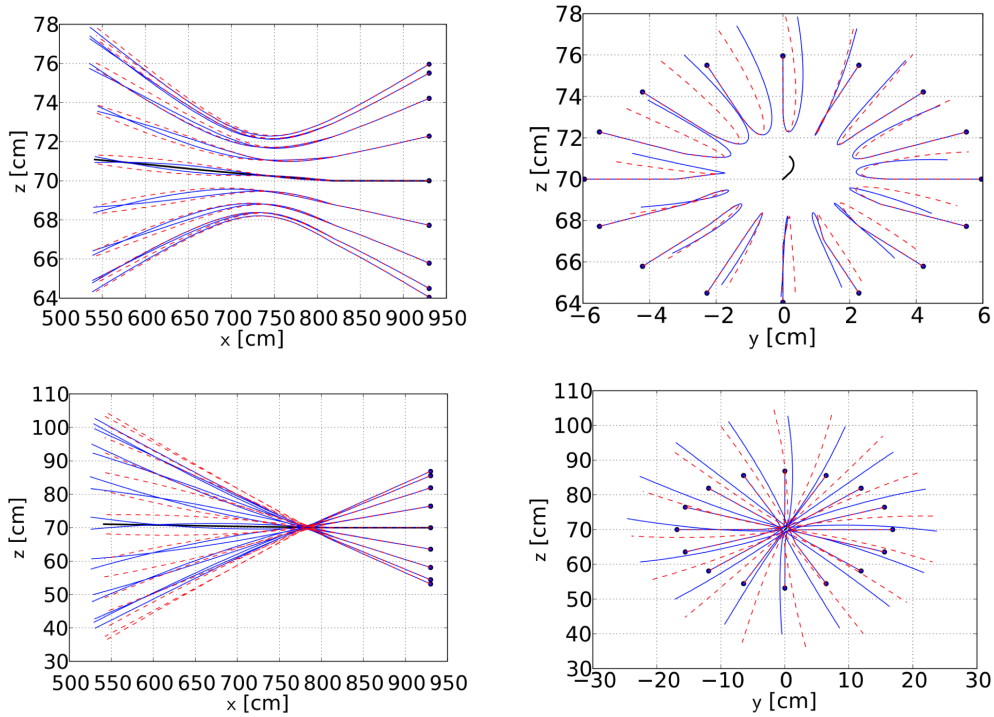

Figure 2.6: Visualization of extended rays for the cases $d_0 = 2$ m, $w_0 = 2$ cm (top) and $d_0 = 1.5$ m, $w_0 = 0.5$ cm (bottom), with $\alpha = \beta = 0$ of Figure 2.1 and 2.4 respectively. The projection of rays on the x-z plane (left panels) and on the y-z plane (right panels) shows the differences between GRAY rays (dashed, red, curves) and TORBEAM rays (solid, blue, curves). The central ray is also shown (thick, black, curve) at the center of the beam.

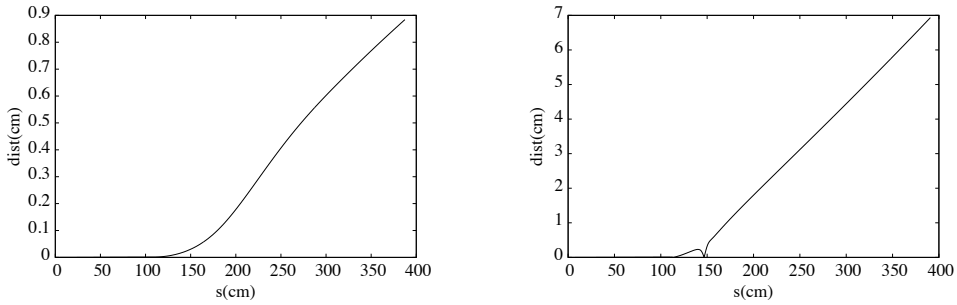

Figure 2.7: The distance between points at the same archlength s versus s is shown for the two GRAY-TORBEAM couples of rays with largest deviations. The left plot refers to the mildly focused beam, while the right plot to the highly focused beam.

the mildly focused beam we chose $s = 380$ cm and we found that the distance in the worst case is 0.86 cm, while for the highly focused beam we chose $s = 390$ cm with a relative distance in the worst case of 6.91 cm. These distances can be compared with the final beam sizes ($\simeq 6$ cm for the mildly focused beam and $\simeq 30$ cm for the highly focused beam), giving as a result that the deviations are $14,4\%$ and 23% of the beam width, respectively, but this results are only an overestimate of the percentage deviations, because the three-dimensional positions along the GRAY-TORBEAM couples of rays used to compute the maximum distances do not lie on the same beam cross section.
Moreover, from the right panels of Fig. 2.6 one can see that the final transversal sections of the GRAY-TORBEAM couples of beams almost completely overlap, and as a consequence, if the ray description of the beams is thick enough (that is if there are enough rays in order to describe the beam densely), the GRAY and the TORBEAM bundles of rays are equivalent to describe the beam absorption, because all the quantities related to the absorption are integrated over the cross-section of the beam.

The results of sections 2.1 and 2.2 give an estimate of the difference between the two independent approximations of the wave energy flux obtained from the standard and optimized formulations of extended ray theory, cf. section 1.5, and show that they are equivalent for practical purposes of beam absorption description in ITER-like conditions.

Part II
Beam absorption

CHAPTER 3

Finite beam width effects on the EC resonant interaction

For a plane wave propagating in a homogeneous infinite plasma with uniform background magnetic field, the EC resonance condition is given by

$$\omega - k_{\parallel} v_{\parallel} - n\Omega_e/\gamma = 0 \,, \tag{3.1}$$

as it was pointed out in the introduction (see section 0.2). The resonance condition is thus represented by a Dirac delta function of argument $\omega - k_{\parallel} v_{\parallel} - n\Omega_e/\gamma$. Using the well known relation

$$\delta\big(f(x)\big) = \frac{\delta(x - x_0)}{|f'(x_0)|} \,, \tag{3.2}$$

where x_0 is the only zero of the f function, and recalling that $\delta(x) = \delta(-x)$, the resonance Dirac delta can be rewritten in the form

$$\delta(\omega - k_{\parallel} v_{\parallel} - n\Omega_e/\gamma) = \frac{1}{|v_{\parallel}|}\delta(k_{\parallel} - k_{\parallel,\mathrm{res}}) \,, \tag{3.3}$$

with

$$k_{\parallel,\mathrm{res}} = \frac{1}{v_{\parallel}}\left[\omega - n\frac{\Omega_e}{\gamma}\right] \,. \tag{3.4}$$

that is, the resonance may be represented by a Dirac delta function of argument $(k_{\parallel} - k_{\parallel,\mathrm{res}})$. This last form can be interpreted in the following way: at a fixed point (x, y, z) in space, an electron with velocity (v_x, v_y, v_z) interacts with a plane wave with a fixed frequency ω if the wave vector component in the B field direction is equal to (3.4).

However, in a tokamak the plasma is finite, non-homogeneous and immersed in a non-uniform magnetic field. Moreover, the wave injected in ECRH&CD applications are finite width Gaussian beams. All these factors play a role in the resonance condition (cf. [8]). Nevertheless, a full rigorous description of these effects on the resonance condition can not be found in literature, and it is beyond the scope of this thesis work. Therefore, in most of the GO based simulation codes, the beam absorption is computed using the simple "plane wave" model. In particular, the GRAY code describes the absorption along each extended ray using the "plane wave" model, without taking into account these corrections to the resonance condition. In order to fill this gap a modified version of the GRAY code was developed in the past that takes into account the corrections of the resonance condition due to the finite beam width. Starting from this work, a revision and refinement has been done in order to include also the effects due to the non-uniformity of the equilibrium magnetic field.

In section 3.1 the resonance broadening due to the finite beam width effect is introduced. In section 3.2 the absorption model currently used in the GRAY code is summarized and a introduction of the broadening in the resonance condition is argued.

It will be shown that the broadened resonance function depends on the width of the $N_\parallel$ spectrum, where $N = kc/\omega$ is the refractive index. As a consequence the beam transversal spectrum has to be known in order to describe the resonance broadening. In section 3.3 a local Gaussian model for the evaluation of the transversal spectrum is presented, while in section 3.3.1 it is validated numerically with a modified version of the GRAY code in ITER-like conditions. In section 3.4 the details on the computation of the $N_\parallel$ spectrum width are presented.

Finally, in section 3.5 some numerical results obtained with the modified version of the GRAY code that contains the corrections due to the broadened resonance model are shown, giving an estimate of the entity of such corrections.

3.1 EC resonance broadening due to finite beam width

We will focus on the effect due to the finite width of the beams. Let us consider for simplicity a non-astigmatic Gaussian beam propagating in vacuum in the z direction of a cartesian system. At a fixed value $\bar{z}$ of the z coordinate, the transversal behavior of the E field is given by

$$E(x, y; \bar{z}) \propto e^{iA(\bar{z})(x^2+y^2)} , \tag{3.5}$$

with the complex valued function $A(z)$ defined by

$$A(z) = \frac{k_0}{2R(z)} + i\frac{1}{w(z)^2} , \tag{3.6}$$

where $w(z)$ and $R(z)$, defined in (1.34) and (1.35) respectively, represent the beam size and the curvature radius along the propagation. The Fourier Transform of (3.5), that is the "transversal spectrum", takes the form

$$\tilde{E}(k_x, k_y; \bar{z}) \propto e^{i\tilde{A}(\bar{z})(k_x^2+k_y^2)} , \tag{3.7}$$

with $\tilde{A} = -1/4A$. It follows that the modulus of the spectrum has a 2D Gaussian shape

$$|\tilde{E}| \propto e^{-(k_x^2+k_y^2)/(\Delta k)^2} , \tag{3.8}$$

with spectrum width $\Delta k = \Delta k_x = \Delta k_y$ given by

$$\Delta k = 1/\sqrt{\mathrm{Im}(\tilde{A})} = 2/w_0 , \tag{3.9}$$

where w_0 is the waist size. As a consequence, the spectrum has a finite width, and this is larger for focalized beams, like those used for ECCD applications.

As it will be shown in the next section a Gaussian beam, injected from vacuum in a tokamak plasma configuration with ITER parameters, retains during plasma propagation a local Gaussian behavior, that is, it can be locally approximated by a vacuum astigmatic Gaussian beam with suitable parameters. The Gaussian beam finite transversal spectrum width results in a finite width in the $k_\parallel$ spectrum, that assumes the form

$$\tilde{E}(k_\parallel; \bar{z}) \propto e^{(k_\parallel - k_{\parallel c}(\bar{z}))^2/(\Delta k_\parallel(\bar{z}))^2} , \tag{3.10}$$

where $k_{\|c}$ is the central value of the spectrum and $\Delta k_\|$ is the spectrum width.
The finite width of the $k_\|$ spectrum leads to a broadening of the resonance condition (3.1). The Dirac delta resonance function $\delta(k_\| - k_{\|,\mathrm{res}})$ is replaced by a broadened function

$$\Delta(k_{\|c} - k_{\|,\mathrm{res}}; \Delta k_\|) \tag{3.11}$$

of the central "parallel spectrum" value $k_{\|c}$, parametrically dependent on the spectrum width $\Delta k_\|$. In momentum space $(u_\|, u_\perp)$, the resonance curves (cf. Fig. 3) become 2D regions. A rigorous description of the broadening of the resonance condition due to the finite size of the beam can not be found in literature.

3.2 Resonance broadening model

3.2.1 GRAY EC absorption model and resonance broadening

Let us consider an extended ray computed by the GRAY code, integrating the ray equations (E.3). The EC power P evolves along the ray trajectory obeying to the equation

$$\frac{dP}{ds} = -\alpha P \,, \tag{3.12}$$

that is a consequence of the optimized form ($v_g \to v_{g\phi}$) of the energy transport equation (1.82), major result of the first part of this thesis, according to Appendix E.6. In Eq. (3.12), $\alpha = \gamma/|v_{g\phi}|$ is the absorption coefficient, with γ being the CGO analogous of (1.28) and $v_{g\phi}$ being the optimized version of the group velocity defined in (1.83), and s is the arc length along the ray. From Eq. (1.28) it follows that

$$\alpha \propto e^* \cdot \epsilon_1^a e \,, \tag{3.13}$$

where e is the κ^0 order polarization vector of the wave electric field and ϵ_1^a is the (κ order) anti-Hermitian part of the dielectric tensor.

While the extended rays are computed using the cold plasma non-relativistic dispersion relation for high-frequency waves propagating in a magnetized plasma, the absorption has to be computed taking into account the temperature effects. As a consequence the absorption coefficient has to be estimated using the relativistic dielectric tensor instead of the cold plasma dispersion tensor considered in chapter 1.

It can be shown that integrals of the Landau type appear in the relativistic dielectric tensor elements:

$$I = \int_{-\infty}^{\infty} \mathrm{d}\gamma \frac{f(\gamma)}{\gamma - \gamma_{\mathrm{res}} + ic_1\omega'} \,, \tag{3.14}$$

where f is a function of the relativistic gamma factor, c_1 is a positive real constant, $\gamma_{\mathrm{res}} = N_\| n_\| + n\Omega_e/\omega$ and ω' is a vanishing positive imaginary part introduced in the wave angular frequency in order to describe the absorption. The solution of this type of integrals in the limit $\omega' \to 0$ is well known and is obtained operating the formal substitution

$$\lim_{c_1\omega' \to 0^+} \frac{1}{\gamma - \gamma_{\mathrm{res}} + ic_1\omega'} = \mathcal{P}\frac{1}{\gamma - \gamma_{\mathrm{res}}} - i\pi\delta(\gamma - \gamma_{\mathrm{res}}) \,, \tag{3.15}$$

that is the Plemelj identity, where $\mathcal{P}$ indicate the principle part integral.

The second term in the RHS of (3.15), proportional to the resonance function $\delta(\gamma - \gamma_{\rm res})$, is related to the anti-Hermitian part ϵ_1^a of the dielectric tensor. In order to take into account the finite beam size effect on the resonance, this function has to be substituted by

$$\Delta(\gamma - \gamma_{c,\rm res}, \Delta N_\parallel) = \sqrt{\frac{2}{\pi}} \frac{1}{|\Delta N_\parallel u_\parallel|} e^{-2(\gamma-\gamma_{c,\rm res})^2/(\Delta N_\parallel^2 u_\parallel^2)} , \tag{3.16}$$

where

$$\gamma_{c,\rm res} = N_{c\parallel} u_\parallel - n\Omega/\omega . \tag{3.17}$$

This fact can be easily understood considering that the resonance function $\delta(N_\parallel - N_{\parallel,\rm res})$, where $N_{\parallel,\rm res} = (\gamma - n\Omega_e/\omega)/u_\parallel$, has to be weighted by the spectral distribution of the squared modulus of the electric field, that is, it has to be substituted by

$$\Delta(N_{c\parallel} - N_{\parallel,\rm res}; \Delta N_\parallel) \propto \int {\rm d}N_\parallel e^{-2(N_\parallel - N_{c\parallel})^2/\Delta N_\parallel^2} \delta(N_\parallel - N_{\parallel,\rm res}) = e^{-2(N_{c\parallel} - N_{\parallel,\rm res})^2/\Delta N_\parallel^2} . \tag{3.18}$$

Noting that $(\gamma - \gamma_{c,\rm res})^2 = u_\parallel^2 (N_{c\parallel} - N_{\parallel,\rm res})^2$ and introducing the correct Gaussian normalization $1/\sqrt{2\pi}\sigma_{\rm Gaussian}$, with $\sigma_{\rm Gaussian} = |\Delta N_\parallel u_\parallel|/2$, Eq. (3.16) is justified.

3.2.2 Wave global description ad ray description: estimation of the broadened resonance function parameters

The central value $\gamma_{c,\rm res}$ and the width $\Delta N_\parallel u_\parallel/2$ of the broadened resonance function (3.16) depend on the central value $N_{c\parallel}$ and the width $\Delta N_\parallel$ of (3.18) respectively, and have to be estimated to compute the beam absorption.

In the GRAY code the absorption is computed along each extended ray. Each ray is weighted to transfer a power proportional to the fraction of the beam cross section area around it, weighted by the Gaussian distribution of the field. In this manner, the effect of a finite width Gaussian beam is partially taken into account. Therefore, the global description of the model presented in the previous section has to be matched with the ray description of the beam.

The GRAY code has the special property of being able to reconstruct the phase fronts along the beam propagation. This result is achieved integrating the extended rays equations (1.65), (1.66), (1.70) using the real part S of the eikonal function as integration variable, that is integrating the system:

$$\begin{aligned} \frac{dx}{dS} &= \left. \frac{\partial H_\phi/\partial N}{N \cdot \partial H_\phi/\partial N} \right|_{H_\phi = 0} , \\ \frac{dN}{dS} &= - \left. \frac{\partial H_\phi/\partial x}{N \cdot \partial H_\phi/\partial N} \right|_{H_\phi = 0} , \\ \frac{\partial H_\phi}{\partial N} &\cdot \nabla\phi = 0 , \end{aligned} \tag{3.19}$$

that follows from dividing the Hamiltonian equations (1.65), (1.66) by (1.16) (with $H \to H_\phi$). Integrating Eqs. (3.19) with suitable initial conditions on an initial phase front, at each step of integration the iterated points lie on a phase front.

This description ceases to be applicable in the regions where the denominator $V_\phi \cdot N$ vanishes, such as cut-offs. In ITER conditions the density is well below the cut-off value for EC waves around all the plasma volume, so that this method of integration of the ray equations is always exploitable. Moreover, in low density plasmas, the refraction is low and the beam retains the Gaussianity along the propagation, so that at each step of integration in S the beam can be well approximated by a Gaussian beam also inside the plasma.

The spectrum is a global property of the Gaussian beam that locally approximates the actual beam along the plasma propagation, so that across the wave front, at a fixed value of S, the spectrum is the same. Therefore, the transversal spectrum is computed at each integration step. Moreover, the ray description allows us to include the resonance modification effect due to the non-uniformity of the equilibrium magnetic field, as it will be shown below.

On the other hand, the matching between the global and the ray description leaves a certain degree of arbitrariness in the estimate of $N_{c\|}$ and $\Delta N_\|$. The choices made will be shown in the following, specifying the details of the model.

Global description

Let us focus first on the $N_{c\|}$ estimate. Consider a fixed point along the beam propagation and a local coordinate system with the z axis pointed in the direction of propagation. The beam refractive index has a fixed z component N_z and a (N_x, N_y) spectrum. If θ is the angle between a refractive index spectral component (N_x, N_y, N_z) and the z axis, one has: $N_z = |N|\cos\theta, N_r = |N|\sin\theta$, where $|N| = \sqrt{N_x^2 + N_y^2 + N_z^2}$ and $N_r = \sqrt{N_x^2 + N_y^2}$. The paraxial character of the wave can be taken into account as follows. Since only the spectrum components with small θ are weighted with a non-vanishing coefficient, one has $N_z \simeq |N|(1 - \theta^2/2), N_r \simeq |N|\theta$, with the result, for small θ: $N_z/N - r \simeq 1/\theta$, that is N_r at the dominant order can be neglected compared to N_z. As a consequence, $N_{c\|}$ can be estimated locally by $b_z N_z$ with a good approximation, where b is the equilibrium magnetic field unit vector.

In the $\Delta N_\|$ estimation there is a certain arbitrariness in the choice of the plane on which the spectrum has to be computed. A good choice would be the plane locally tangent to the magnetic surface passing for the selected point, so that the spectral width in the B field direction can be obtained directly. We made a different choice, better suited for numerical implementation. First, the local transversal spectrum is computed, that is the spectrum is computed on the plane perpendicular to the local direction of propagation. If we consider the local reference frame adopted in the $N_{c\|}$ estimate, it is the xy plane. As a second step, the spectrum is integrated in the direction perpendicular to the projection of the equilibrium magnetic field on the xy plane, and the width of the obtained 1D spectrum is computed. Finally, the result is multiplied by $|\sin\vartheta|$, where theta is the angle between B and the direction of propagation, in order to be consistent with the case of parallel (to B) propagation, in which the result $\Delta N_\| = 0$ is expected.

Ray description and effects due to the non-uniformity of the equilibrium magnetic field

At each step of integration of the ray equations in the S parameter, the reference ray wave vector $N_{11} = k_{11}/k_0$ modulus estimates the N_z of the previous section (the (x, y, z) a coordinate system is chosen as in Appendix E.2). Consider an iterate point x_{jk} of the jk-th ray on the selected phase front (where here x_{jk} indicates with a slightly misleading notation the vector $(x, y, z)_{ij}$ instead of its first component, with j and k are the radial and angular indices related to the distribution of the points on the initial phase front, cf. Appendix E.3). The $N_{c\|}$ is computed as $N_{c\|} \simeq b(x_{jk}) \cdot N_z$ instead of $N_{c\|} \simeq b(x_{11}) \cdot N_z$ (x_{11} being the reference ray point on the selected phase front), in order to take into account the non-uniformity of the equilibrium magnetic field across the beam phase front.

Turning to the $\Delta N_\|$ estimation, it is done as follows. If a phase front relative to a fixed value of the real part of the eikonal S is considered, the transversal spectrum of the electric field is computed on the plane perpendicular to k_{11} passing through x_{11}, that is the xy plane (this task is described in the following section 3.3). Then, considering the iterate x_{jk} of the jk-th ray on the selected phase front and restricting to the xy plane, the E field spectrum is integrated in the direction perpendicular to the projection of the local equilibrium magnetic field $B(x_{jk})$ on that plane, in order to take into account the B non-uniformity effects. Then the width of the obtained 1D spectrum is computed and finally the result is multiplied by the sine of the angle between $B(x_{jk})$ and k_{11} as was explained in the previous section. the details of $\Delta N_\|$ estimation are given in section 3.4.

3.3 Computation of the beam transversal spectrum

The GRAY code describes the propagation of general astigmatic Gaussian beams (cf. Appendix E and [11]). Considering firstly the propagation in free space and restricting to a plane perpendicular to the direction of propagation, the constant-phase and the constant-amplitude contours are ellipses with non coinciding principal axes, instead of the concentric circumferences of the non-astigmatic beams. The phase fronts are elliptic paraboloids.

During the plasma propagation the refraction enhances the astigmatism and the anisotropy of the medium decouples the wave vector direction from the group velocity direction. Moreover, due to the plasma anisotropy, the beam axis is no more a straight line. Nevertheless, even during plasma propagation, if the density is not so high that the anisotropic refraction effect is too prominent, a beam retains its Gaussianity at least locally along the propagation with a good approximation. The phase fronts maintain the parabolic shape, with axis in the local direction of the wave vector. This fact has been investigated in ITER-like conditions with the GRAY code, obtaining the phase fronts integrating the ray equations using the real part S of the eikonal as integration variable and plotting the phase fronts points in a local frame with axis either in the direction of the reference ray wave vector or in the group velocity direction. An example is shown in fig. 3.1, relative to a simulation of the propagation of a beam in a ITER standard H-mode scenario at the end of the plasma current flat-top. As one can see, the front shows an elliptic paraboloid shape in the system with z in the k_{11} direction. Nevertheless, the curvature radii of the paraboloid are large compared to the beam width, so that the front is almost flat, as it can be seen in the representation of the front in the system with z in the v_g direction.

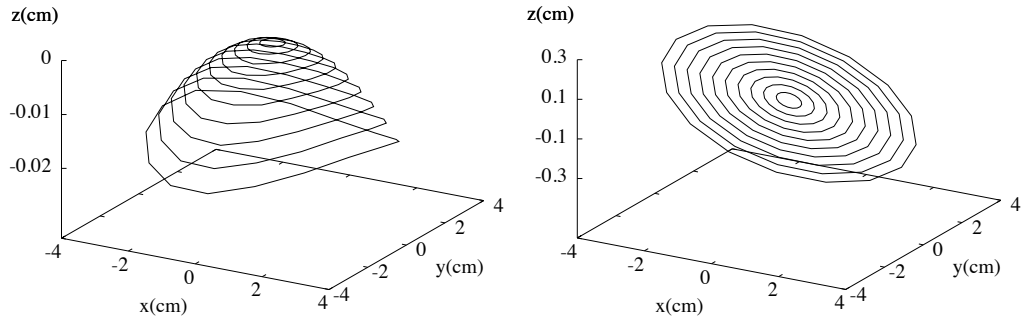

Figure 3.1: Phase front in the local (x, y, z) reference frame, at the fixed value $S = 160$ cm of the real part of the eikonal. The beam is launched from the UL with poloidal and toroidal launching angles $\alpha = 40^\circ, \beta = 20^\circ$, with free space equivalent waists $w_{0x} = w_{0y} = 2.9$ cm, equivalent waist distances $d_{0x} = d_{0y} = 1$ m, and it is described by a bundle of rays up to $1/e$ of the central E field value: (Left) z axis in k_{11} direction; (Right) z axis in v_{g11} direction; k_{11} and v_{g11} being the reference ray's wave vector and group velocity respectively.

The conservation of the beam Gaussianity along plasma propagation suggests that the spectrum can be computed locally as the analytic spectrum of a Gaussian beam with parameters that vary along the propagation. A routine devoted to this computation was recently added to the GRAY code.

In order to test the deviation of the real spectrum from the Gaussian spectrum computed with this routine and to allow the calculation of the transversal spectrum in extreme cases in which the loss of Gaussianity is no more negligible (for example high density propagation close to cut-off density), we developed an additional routine, able to compute the spectrum numerically, without imposing the Gaussian ansatz on the E field.

As it will be shown in section 3.3.2, we recovered that in ITER conditions the spectrum is well approximated by a Gaussian spectrum and as a consequence the first routine can be used to compute it with a very good approximation.

3.3.1 Computation of the spectrum assuming a local Gaussian model

As it was anticipated, in low density plasmas it can be shown that a Gaussian beam retains locally its Gaussianity during plasma propagation. The GRAY code routine that computes the beam transversal spectrum approximates the beam locally by a general astigmatic Gaussian beam. At each iterated phase front (at each fixed value of the integration variable S), the local Gaussian beam parameters are computed and the transversal spectrum is obtained analytically.

The analytical derivation of the transversal spectrum of a general astigmatic Gaussian beam is reviewed, and then the local determination of the Gaussian beam parameters is described.

Analytic spectrum computation for a general astigmatic Gaussian beam

The electric field of a general astigmatic beam propagating in the z direction of a cartesian system can be put in the form

$$E(x,y,z,t) = E_0(z)e^{-i\phi_{\mathrm{Gouy}}(z)}e^{e^{iM(z):rr}}e^{ik_0z-i\omega t}\ , \tag{3.20}$$

where $r=(x,y)$, M is the matrix

$$M = \begin{pmatrix} A & C/2 \\ C/2 & B \end{pmatrix}\ , \tag{3.21}$$

with complex elements, where both M, A, B, C depend on $\bar{z}$, and the $M:rr$ notation means

$$M:rr = \sum_{i,j=1}^{2} r_i M_{ij} r_j\ . \tag{3.22}$$

The non-astigmatic beam case is recovered if $C=0$ and $A=B$, so that $M_{ij}=A\delta_{ij}$.
The transversal behavior at a fixed value $\bar{z}$ of the z coordinate is given by

$$E(x,y;\bar{z}) \propto e^{iM(\bar{z}):rr}\ , \tag{3.23}$$

similar to (3.5).
In parallel with Eq. (3.7), the Fourier transform of (3.23) takes the form

$$\tilde{E}(k_x,k_y;\bar{z}) \propto e^{i\tilde{M}(\bar{z}):k_rk_r}\ , \tag{3.24}$$

where $k_r=(k_x,k_y)$ and $\tilde{M}=(-1/4)M^{-1}$, where M^{-1} indicate the inverse matrix.

Determination of the local Gaussian beam parameters

The elements of the matrix M (cf. (3.21)) are obtained at each step of integration taking into account the eikonal ansatz

$$E(x,y,z,t) \propto e^{ik_0[S(x,y,z)+i\phi(x,y,z)]-i\omega t} \tag{3.25}$$

of the wave electric field. From Eqs. (3.25), (3.20) and (3.21) it follows that

$$S = z + (A_R x^2 + B_R y^2 + C_R xy)\ , \tag{3.26}$$

$$k_0\phi = A_w x^2 + B_w y^2 + C_w xy\ . \tag{3.27}$$

where

$$(A,B,C) = k_0(A_R,B_R,C_R) + i(A_w,B_w,C_w)\ . \tag{3.28}$$

with (A_R,B_R,C_R) and (A_w,B_w,C_w) real vectors. The subscripts R,w indicate that (A_R,B_R,C_R) are related to the local radii of curvature R_ξ,R_η of the phase front and (A_w,B_w,C_w) are related to the local beam sizes w_ξ,w_η (cf. Appendix E.2).

The key point in the (A_R,B_R,C_R) coefficients determination is the fact that the real part of the eikonal function S is constant by definition on a phase surface so that, disregarding the slow z dependence of the coefficients, from Eq. (3.26) it follows that they can be obtained by a least square fit of the phase front surface. The (A_w,B_w,C_w) coefficients can be

estimated in a similar way. The value of the imaginary part of the eikonal function ϕ depends on the (x, y) coordinates, but it is constant along each extended ray (cf. Eq. (1.70)), so that on a given phase front the ϕ value of each ray is known from the initial conditions. Each ϕ value, known on the phase front, is transferred on the plane $z = 0$ by a first order Taylor expansion. As a consequence, the function $k_0\phi(x, y) = A_w x^2 + B_w y^2 + C_w xy$ plays the role that the function $z(x, y) = A_R x^2 + B_R y^2 + C_R xy$ had in the (A_R, B_R, C_R) estimate, and the coefficients can be estimated by a least square fit.

Let us show this procedure in detail. The phase front is composed of the points at a given step of integration in the S parameter, with local coordinates $\{(x_i, y_i, z_i)\ ,\ i = 1, \ldots, N_{\rm tot}\}$, where $N_{\rm tot} = (N_r - 1)N_\theta + 1$ is the total number of rays, with N_r rays in the radial direction and N_θ rays in the angular direction (cf. Appendix E.3).

The (A_R, B_R, C_R) least square fit is performed minimizing the function

$$f(A_R, B_R, C_R) = \sum_{i=1}^{N_{\rm tot}} \left[z_i(x, y) + \left(A_R x_i^2 + B_R y_i^2 + C_R x_i y_i \right) \right]^2 \ . \tag{3.29}$$

The result is given by the following expressions of the coefficients A_R, B_R, C_R:

$$\begin{aligned} A_R = &\left(-\langle x^2 z\rangle \langle xy^3\rangle^2 + \langle x^2 y^2\rangle \langle xy^3\rangle \langle xyz\rangle - \langle x^2 y^2\rangle^2 \langle y^2 z\rangle - \right. \\ &\left. + \langle x^3 y\rangle \langle xy^3\rangle \langle y^2 z\rangle + \langle x^2 y^2\rangle \langle x^2 z\rangle \langle y^4\rangle - \langle x^3 y\rangle \langle xyz\rangle \langle y^4\rangle \right) / \Delta \\ B_R = &\left(-\langle x^2 y^2\rangle^2 \langle x^2 z\rangle + \langle x^2 z\rangle \langle x^3 y\rangle \langle xy^3\rangle + \langle x^2 y^2\rangle \langle x^3 y\rangle \langle xyz\rangle - \right. \\ &\left. - \langle x^4\rangle \langle xy^3\rangle \langle xyz\rangle - \langle x^3 y\rangle^2 \langle y^2 z\rangle + \langle x^2 y^2\rangle \langle x^4\rangle \langle y^2 z\rangle \right) / \Delta \\ C_R = &\left(+\langle x^2 y^2\rangle \langle x^2 z\rangle \langle xy^3\rangle - \langle x^2 y^2\rangle^2 \langle xyz\rangle + \langle x^2 y^2\rangle \langle x^3 y\rangle \langle y^2 z\rangle - \right. \\ &\left. - \langle x^4\rangle \langle xy^3\rangle \langle y^2 z\rangle - \langle x^2 z\rangle \langle x^3 y\rangle \langle y^4\rangle + \langle x^4\rangle \langle xyz\rangle \langle y^4\rangle \right) / \Delta \end{aligned} \tag{3.30}$$

where

$$\begin{aligned} \Delta = &\langle x^2 y^2\rangle^3 - 2\langle x^2 y^2\rangle \langle x^3 y\rangle \langle xy^3\rangle + \langle x^4\rangle \langle xy^3\rangle^2 + \\ &+ \langle x^3 y\rangle^2 \langle y^4\rangle - \langle x^2 y^2\rangle \langle x^4\rangle \langle y^4\rangle \end{aligned} \tag{3.31}$$

and

$$\langle x^\alpha y^\beta z^\gamma \rangle = \frac{1}{N} \sum_{i=1}^{N} x_i^\alpha y_i^\beta z_i^\gamma \ . \tag{3.32}$$

The (A_w, B_w, C_w) fit is performed in the same way, by simply replacing $z_i(x, y) \to k_0\phi_i(x, y)$ where, for every iterate point $(x, y, z)_i$ on the phase front, $\phi_i(x, y)$ is the value of the imaginary part of the eikonal evaluated at the projection of the point on the (x, y) plane, obtained with a Taylor expansion at the first order, that is

$$\phi_i(x, y) \equiv \phi_i(x, y, 0) = \phi_i(x, y, z) - \frac{\partial \phi_i(x, y, z)}{\partial z} z \ . \tag{3.33}$$

Finally, the (A, B, C) coefficients of matrix (3.21) are reconstructed using Eq. (3.28).

All the procedure described in this section is based on the assumption that the beam is locally well approximated by a general astigmatic Gaussian beam. This assumption is verified numerically in ITER-like conditions in the following section.

3.3.2 Numerical computation of the transversal spectrum via 2D Fast Fourier Transform

In order to test the validity of the Gaussian model we developed a routine devoted to the direct numerical computation of the transversal spectrum. At each iterate of the extended rays equation integration in the S variable, constituted by $N_{\rm tot} = (N_r - 1)N_\theta + 1$ points x_{jk} ($j = 1, \ldots, N_r$; $k = 1, \ldots, N_\theta$), lying on the same phase front, the electric field eikonal is reconstructed on the plane perpendicular to the reference ray wave vector passing through the reference ray point x_{11}. Then, the 2D Fourier transform of the field is computed on that plane by numerical means, obtaining a result that does not rely on the local Gaussian field assumption.

A summary of the routine is reported, while afterwards the numerical results obtained with this routine are compared with those obtained with the local Gaussian beam approximation, showing that in ITER-like conditions the difference between the Gaussian approximated spectrum and the actual spectrum is negligible.

Firstly, the eikonal values are obtained on the plane xy of the local system (cf. page 38) by first order Taylor expansions from the values on the phase front, that is $\psi(x, y) = S(x, y) + i\phi(x, y)$, with real and imaginary parts given by

$$\begin{aligned} S_i(x, y) &\equiv S_i(x, y, 0) = S_i(x, y, z) - N_{zi}(x, y, z)z \,, \\ \phi_i(x, y) &\equiv \phi_i(x, y, 0) = \phi_i(x, y, z) - \frac{\partial \phi_i(x, y, z)}{\partial z} z \,, \end{aligned} \tag{3.34}$$

with $i = 1, \ldots, N_{\rm tot}$. The electric field has a transversal behavior given by

$$E(x, y) \propto e^{ik_0[S(x,y)+i\phi(x,y)]} \,, \tag{3.35}$$

This function is evaluated on a regular grid and its Fourier transform is computed by a 2D Fast Fourier Transform (FFT) routine. For a detailed description of the routine we refer to Appendix F.1.

Comparison between Gaussian approximated spectrum and actual spectrum: numerical results

Using a modified version of the GRAY code that includes a new routine able to compute the E field spectra both with the local Gaussian model and by direct numerical FFT, the difference between the two results is computed at each step of integration of the ray equations as follows. Firstly the outputs of the two methods of computation, evaluated on the regular grid on which the 2D FFT output is given, are normalized to the central value. Let us call $\tilde{E}_{{\rm Gauss},i}$ and $\tilde{E}_{{\rm FFT},i}$ these normalized values respectively, with $i = 1, \ldots, N_{\rm grid}$, where $N_{\rm grid}$ is the total number of grid points. Then the difference is evaluated by the mean squared error D, computed taking into account only the central $\tilde{N}$ points of the grid, defined by

$$D = \sqrt{\frac{1}{\tilde{N}} \sum_{i=1}^{\tilde{N}} \left[|\tilde{E}_{{\rm Gauss},i}| - |\tilde{E}_{{\rm FFT},i}| \right]^2} \,. \tag{3.36}$$

For a more detailed description of this procedure we refer to Appendix F.1.

A standard ITER scenario at the end of the flat-top is chosen and for simplicity a beam that is non-astigmatic at the launch. The launch conditions and beam parameters are as follows. An equatorial injection is considered with the antenna placed at $x_{\rm lab} = 930\ {\rm cm},\ y_{\rm lab} = 0\ {\rm cm},\ z_{\rm lab} = 70\ {\rm cm}$. A mildly-focused beam is chosen with a free space equivalent waist size $w_0 = 3\ {\rm cm}$ and waist equivalent distance from the antenna $d_0 = 2\ {\rm m}$. The beam is modeled with $(N_r - 1)N_\theta + 1$ rays, with $N_r = 15$ and $N_\theta = 16$, up to $e^{-1.96}$ of the central value of E field module ($\rho_{\rm max} = 1.4$, with $\rho_{\rm max}$ defined in Appendix E.3). In the simulation we described the beam with a broadened bundle of rays with external rays beyond the $1/e$ surface to improve the resolution of the spectrum near the waist.

In order to test the variation of the spectrum with plasma density, we analyzed two cases, relative to two different values of the plasma central density: the standard value of this ITER scenario ($n_0 = 1\times10^{20}{\rm m}^{-3}$) and the double value $n_0 = 2\times10^{20}{\rm m}^{-3}$. Both these values of the density are allowed from the point of view of wave propagation because they are well below the cutoff density, that in this case is given by $n_{\rm cutoff} \sim 3.6\times10^{20}{\rm m}^{-3}$ (the beam frequency is $f_{EC} = 170$ GHz and the plasma frequency $f_p = \omega_p/2\pi$ is expressed in function of the density by $f_p[{\rm Hz}] \sim 8980\sqrt{n_e[cm^{-3}]}$) .

In the mean squared error D computation we put $\tilde{N} = 121$. In Fig. 3.2 and Fig. 3.3 the projection of the trajectory of the beam rays in the poloidal plane and the mean squared error D versus the reference ray's arc length s_{11} are shown with plasma central density given by $n_0 = 1\times10^{20}{\rm m}^{-3}$ and $n_0 = 2\times10^{20}{\rm m}^{-3}$ respectively. It is worth noting that the error D starts to be non vanishing at the plasma boundary ($s_{11} \sim 1\ {\rm m}$) and grows nearly following the beam width profile. The D values are greater in the double density case but they are still very low. In Fig. 3.4 the transversal spectra of the beam in three different regions along the propagation (near the antenna, near the waist and near the resonance) are shown for the two density cases, comparing the Gaussian model computation with the numerical computation via 2D Fast Fourier Transform. In Fig. 3.5 the contour plots of the spectra in the resonance region are shown in the two density cases. From these two plots it is easy to see that in the double density case the beam is more rotated and stretched than in the normal density case, as it was expected, and the difference between the Gaussian spectrum and the numerical spectrum is more evident, in agreement with Fig. 3.2 and Fig. 3.3, but still small. Similar behavior was observed varying the launch positions (USM and LSM of Upper Launcher). The agreement between these two ways of calculating the spectrum ceases to be satisfactory increasing the central density up to values close to cutoff density.

It is possible to conclude that in ITER conditions the beam spectrum remains approximately Gaussian during the propagation and in particular in the absorption region. As a consequence it is possible to compute it with the Gaussian model instead that via 2D Fast Fourier Transform, with a very good approximation.

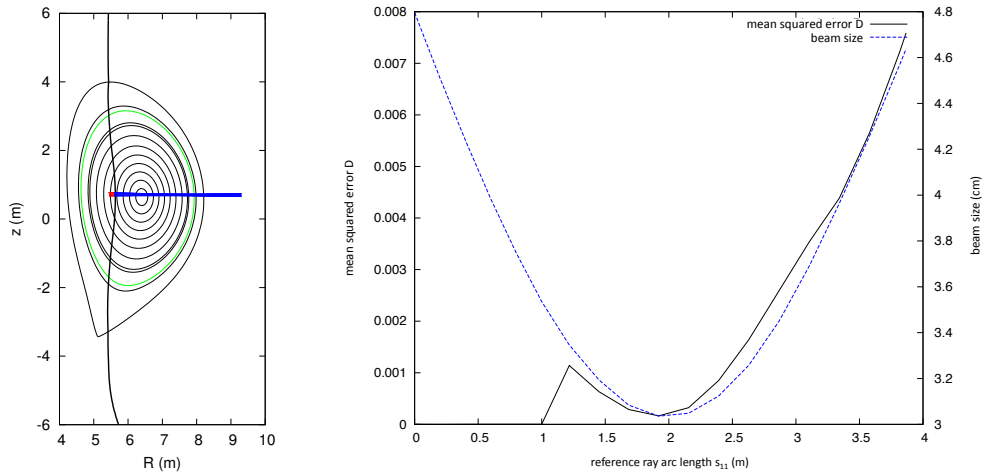

Figure 3.2: Equatorial launch with central electron density $n_0 = 1 \times 10^{20}\mathrm{m}^{-3}$. (Left) Beam trajectory in the poloidal plane (up to 1/e of the central E value, with 13x16 rays); (Right) Mean squared error D and one of the two beam widths versus the arc length s_{11} of the reference ray.

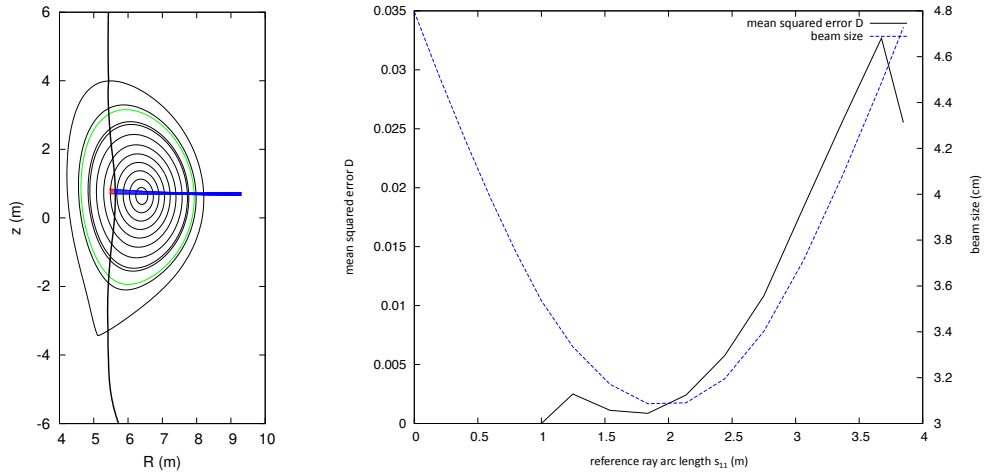

Figure 3.3: The same as Fig. 3.2 with double central electron density $n_0 = 2 \times 10^{20}\mathrm{m}^{-3}$.

Near the antenna:

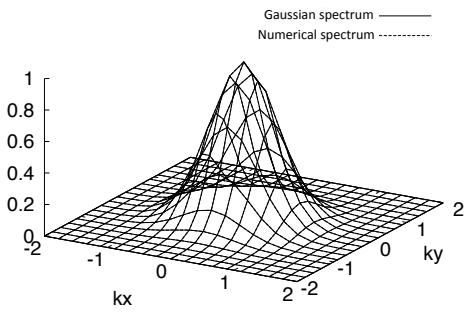

(a) $n_0 = 1 \times 10^{20}\mathrm{m}^{-3}, s_{11} \sim 0.2\mathrm{m}$.

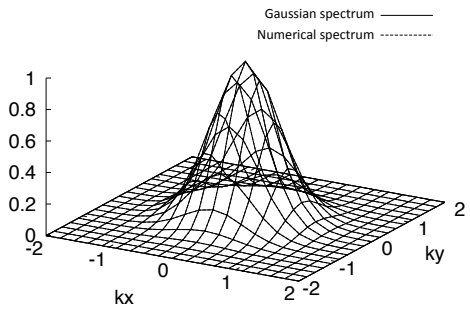

(b) $n_0 = 2 \times 10^{20}\mathrm{m}^{-3}, s_{11} \sim 0.2\mathrm{m}$.

Near the waist:

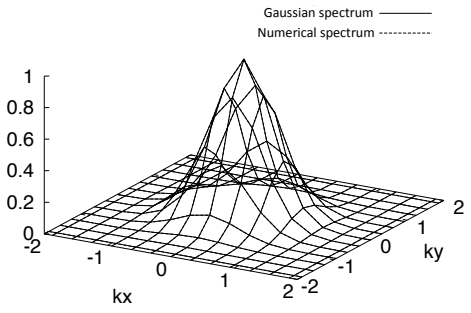

(c) $n_0 = 1 \times 10^{20}\mathrm{m}^{-3}, s_{11} \sim 2.2\mathrm{m}$.

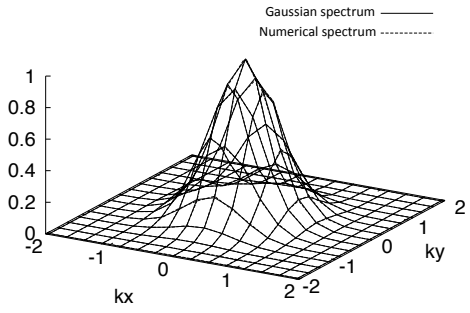

(d) $n_0 = 2 \times 10^{20}\mathrm{m}^{-3}, s_{11} \sim 2.1\mathrm{m}$.

Near the electron cyclotron resonance:

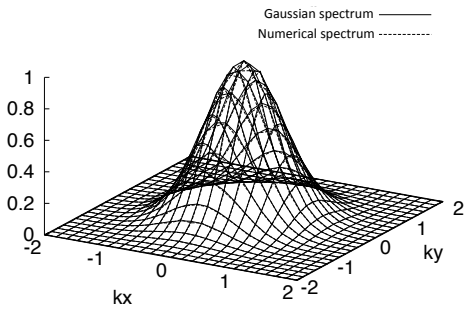

(e) $n_0 = 1 \times 10^{20}\mathrm{m}^{-3}, s_{11} \sim 3.8\mathrm{m}$.

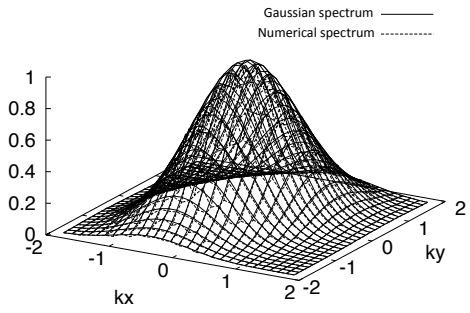

(f) $n_0 = 2 \times 10^{20}\mathrm{m}^{-3}, s_{11} \sim 3.7\mathrm{m}$.

Figure 3.4: Comparison between the beam transversal spectrum obtained with the Gaussian model and the one obtained numerically by using 2D FFT. (Left) Electron density $n_0 = 1 \times 10^{20}\mathrm{m}^{-3}$. (Right) Electron density $n_0 = 2 \times 10^{20}\mathrm{m}^{-3}$.

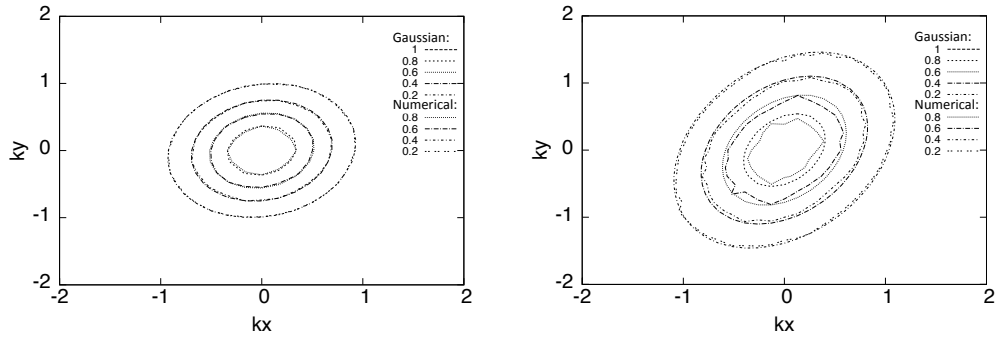

(a) $n_0 = 1 \times 10^{20}\mathrm{m}^{-3}$, $s_{11} \sim 3.8\mathrm{m}$, contour plot.

(b) $n_0 = 2 \times 10^{20}\mathrm{m}^{-3}$, $s_{11} \sim 3.7\mathrm{m}$, contour plot.

Figure 3.5: Comparison between the beam transversal spectrum obtained with the Gaussian fit and the one obtained numerically by using 2D fft. (Left) Electron density $n_0 = 1 \times 10^{20}\mathrm{m}^{-3}$. (Right) Electron density $n_0 = 2 \times 10^{20}\mathrm{m}^{-3}$. Contour plots of the final steps.

3.4 Computation of the parallel refractive index spectrum width

The transversal spectrum, computed according to the local Gaussian approximation, can be used to compute the parallel refractive index spectrum width $\Delta N_\parallel$.

We proceed as follows. First, the equilibrium magnetic field unit vector $b \equiv B/|B|$ is projected on the plane (x, y) of the local system (x, y, z) introduced at page 38, by $\bar{b} = b - \cos\theta\hat{z}$, where θ is the angle between B and the z axis and $\hat{z}$ demotes the z axis unit vector. Then, a new coordinate system $(\zeta_\parallel, \zeta_\perp)$ is introduced in the (x, y) plane, with axes in the directions of $\bar{b}$ and $\hat{z} \times \bar{b}$, rotated with respect to the (x, y) axes by the angle ι. It follows that the two couples of coordinates $r = (x, y)$ and $r^{'} = (\zeta_\parallel, \zeta_\perp)$ are related by $r = Rr^{'}$, where the rotation matrix R has components

$$R = \begin{pmatrix} \cos\iota & -\sin\iota \\ \sin\iota & \cos\iota \end{pmatrix} = \begin{pmatrix} b_x & -b_y \\ b_y & b_x \end{pmatrix} . \tag{3.37}$$

Now the transversal spectrum (3.24) can be expressed in the rotated system as follows:

$$\tilde{E}(k_\parallel, k_\perp; \bar{z}) \propto e^{i\tilde{M}^{'}(\bar{z}):k_{r^{'}}k_{r^{'}}} , \tag{3.38}$$

with $\tilde{M}^{'} = {}^tR\tilde{M}R$ and $k_{r^{'}} = (k_\parallel, k_\perp)$, where ${}^tR$ denotes the transpose of the matrix R. This fact is easily shown considering Eq. (3.23). It can be expressed in the $r^{'} = (\zeta_\parallel, \zeta_\perp)$ system as follows:

$$E \propto e^{ir\cdot Mr} = e^{ir^{'}\cdot({}^tRMR)r^{'}} , \tag{3.39}$$

Therefore, the spectrum is given by

$$\tilde{E} \propto e^{ik_{r^{'}}\cdot\tilde{M}^{'}k_{r^{'}}} , \tag{3.40}$$

with

$$\tilde{M}^{'} = -\frac{1}{4}({}^tRMR)^{-1} = -\frac{1}{4}R^{-1}M^{-1}({}^tR)^{-1} . \tag{3.41}$$

Equation (3.38) follows from Eq. (3.41), recalling that R is a rotation matrix, so that it is orthogonal ($R^{-1} = {}^tR$), and $\tilde{M} = -(1/4)M^{-1}$.

Disregarding the phase, Eq. (3.38) implies

$$|\tilde{E}| \propto e^{-k_{r^{'}}\cdot[\mathrm{Im}(\tilde{M}^{'})]k_{r^{'}}} , \tag{3.42}$$

where $\mathrm{Im}(\tilde{M}^{'})$ indicates the matrix that has components given by the imaginary part of $\tilde{M}^{'}$ components. This expression has to be integrated in the $k_\perp$ direction, in order to estimate the width $\Delta k_\parallel$ of the obtained 1D spectrum, that is

$$|\tilde{E}(k_\parallel; \bar{z})| = \int_{-\infty}^{\infty} |\tilde{E}(k_\parallel, k_\perp; \bar{z})| \, \mathrm{d}k_\perp . \tag{3.43}$$

The integral can be readily done taking into account the following result. Given a real 2×2 matrix T and a coordinate system (x, y) with position vector $r = (x, y)$, it can be shown that

$$\int_{-\infty}^{\infty} e^{-r\cdot Tr} dy = \sqrt{\frac{\pi}{T_{yy}}} e^{-\frac{\det(T)}{T_{yy}}x^2} . \tag{3.44}$$

As a consequence, implying the $\bar{z}$ dependence, one has

$$|\tilde{E}(k_{\parallel})| \propto e^{-\gamma k_{\parallel}^2} , \tag{3.45}$$

with

$$\gamma = \frac{\det[\mathrm{Im}(\tilde{M}')]}{[\mathrm{Im}(\tilde{M}')]_{\perp\perp}} . \tag{3.46}$$

The $\Delta k_{\parallel}$ width is computed by $(\Delta k_{\parallel})^2 = 1/\gamma$.

Moreover, the result is multiplied by the absolute value of the sine of the angle θ that the equilibrium magnetic field B makes with the z direction, so that actually $\Delta k_{\parallel}$ is defined by $|\sin\theta|/\sqrt{\gamma}$. Finally, the result is divided by $k_o = \omega/c$ in order to obtain the refractive index parallel spectrum width $\Delta N_{\parallel} = \Delta k_{\parallel}/k_0$.

3.5 Power absorption profile's broadening due to finite beam width: numerical results

The broadening model described so far has been implemented in a new version of the GRAY code, able to compute the power absorption profiles with the broadened resonance effects. In this section some examples of power absorption profiles obtained with this new version of the GRAY code in reference plasma scenarios for the ITER project are presented, showing the entity of the corrections introduced including the finite beam width effects in the absorption computation.

In Figures 3.6 and 3.7 a scansion in the poloidal launching angle α is presented, with fixed toroidal launching angle $\beta = 20°$ (reference value of the Upper Launcher design, cf. chapter 4), for beams injected from the Upper Steering Mirror or the Lower Steering Mirror of the ITER Upper Launcher respectively. An ITER standard H-mode scenario at the end of the plasma current flat top is considered. This scenario, the same used to perform the simulations of section 3.3.2, is referred to as "Scenario 1" and it will be analyzed in detail in chapter 4. In the figures the power density dP/dV deposited by the wave is represented in function of the toroidal flux coordinate ρ. The absorption profiles represented by red dotted lines are obtained taking into account the finite beam width effects on the resonance condition in the wave absorption computation, while the black solid lines are relative to the "plane wave" absorption model.

In Fig. 3.8 the x-axis zoom of four profiles extracted from the LSM α-scan is presented, with peak and width parameters summarized in Table 3.1. From that table it can be seen that the absolute value of the percentage differences between the peaks of the profiles obtained using the normal and broadened absorption model respectively are at most of the order of 10 percent, and the same holds for the percentage differences between the power density profiles widths $\overline{\Delta\rho}$, computed according to (E.30).

In Fig. 3.9 the same analysis is presented considering four beams launched aiming at the $q = 3/2$ and $q = 2$ from the LSM and USM. In this simulations we used the same ITER scenario and beam parameters as in Ramponi et al. ([12] and [13]), summarized in Table 3.2. A ITER H-mode old scenario denoted "scenario 2" at the end of the plasma current flat-top is considered (it is a different version of the actual reference "scenario 2"),

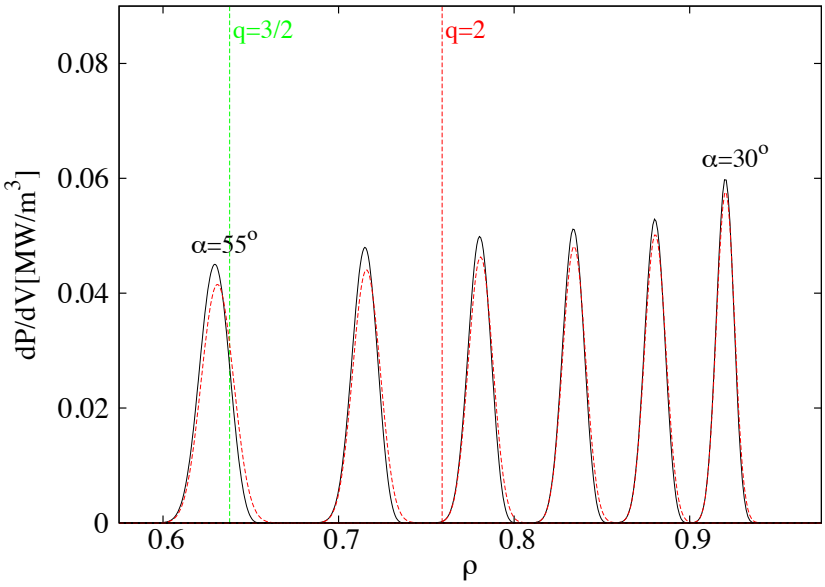

Figure 3.6: Upper Steering Mirror scanning in the poloidal launching angle α, at fixed toroidal launching angle $\beta = 20°$. Five power density profiles are presented in function of the toroidal flux coordinate ρ, for α ranging from $\alpha = 30°$ to $\alpha = 33°$, with spacing $\Delta\alpha = 5°$. The black solid lines represent the profiles obtained without the effects due to the finite beam width, while the dashed red lines show the results of the broadened EC resonance model. The green and red vertical dated lines represent the $q = 3/2$ and $q = 2$ rational surfaces respectively.

		δ resonance		Δ resonance		percentage differences	
mirror	α [deg]	$(dP/dV)_{\max}$ [MW/m^3]	$\overline{\Delta\rho}$	$(dP/dV)_{\max}$ [MW/m^3]	$\overline{\Delta\rho}$	$(dP/dV)_{\max}$ [MW/m^3]	$\overline{\Delta\rho}$
LSM	35°	0.0735	0.0117	0.0676	0.0130	8 %	11.1 %
LSM	40°	0.0665	0.0134	0.0613	0.0149	7.8 %	11.1 %
LSM	45°	0.0587	0.0160	0.0552	0.0174	6 %	8.7 %
LSM	50°	0.0502	0.0200	0.0490	0.0211	2.4 %	5.5 %

Table 3.1: Power density profiles parameters relative to the cases of Fig. 3.8. The peak values $(dP/dV)_{\max}$ and the widths $\overline{\Delta\rho}$, computed according to (E.30), are shown for the four injection cases, for the profiles obtained without the finite beam width effects (δ resonance) and for the broadened ones (Δ resonance). Moreover, the absolute value of the percentage differences between the peaks and widths of the δ and Δ model are shown.

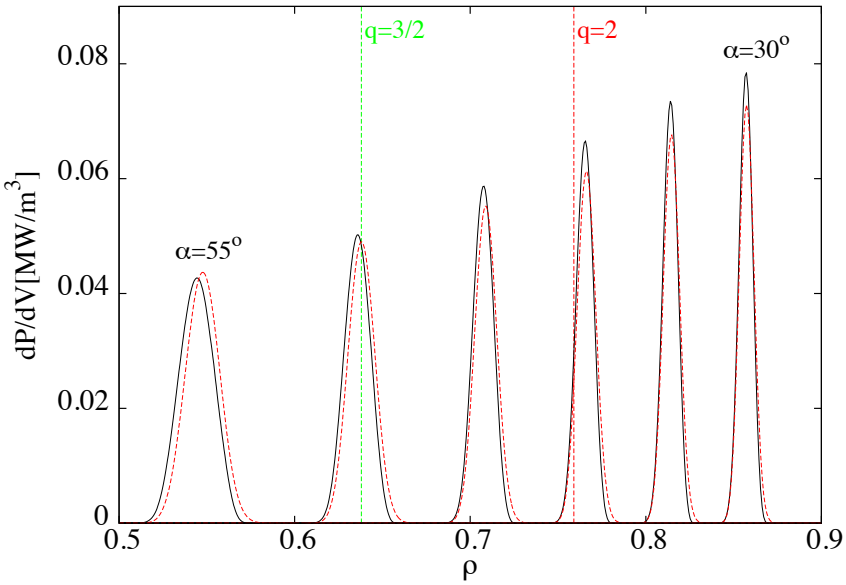

Figure 3.7: The same as Fig. 3.6 for the Lower Steering Mirror.

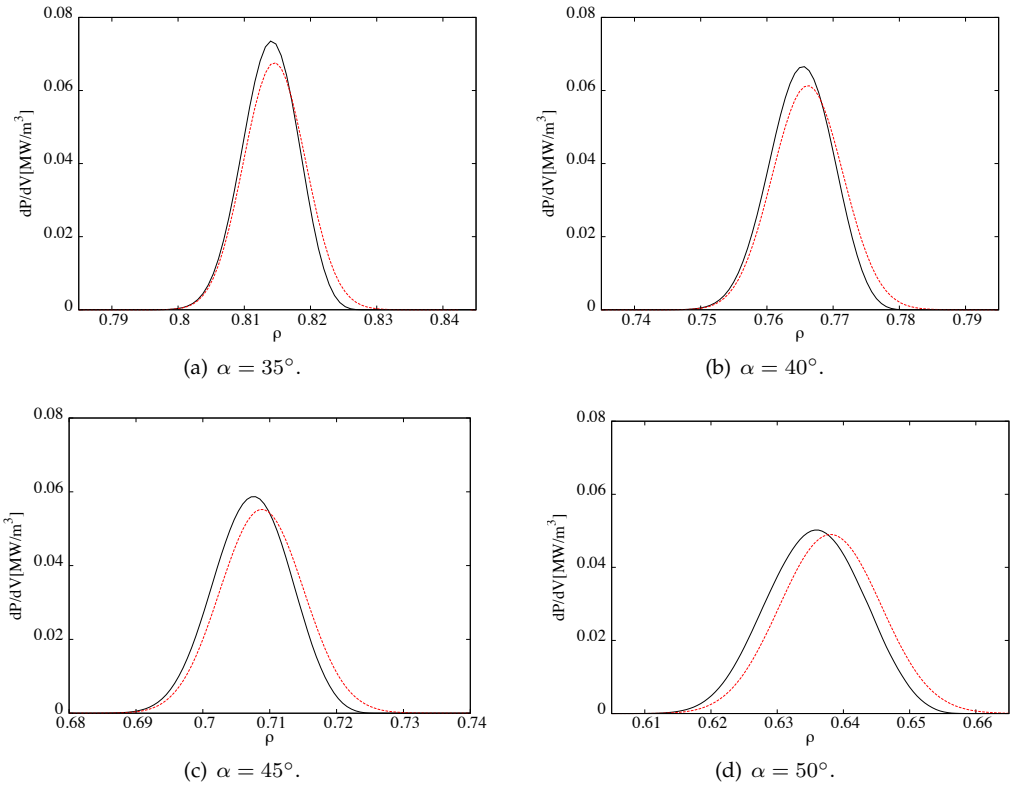

(a) $\alpha = 35°$.

(b) $\alpha = 40°$.

(c) $\alpha = 45°$.

(d) $\alpha = 50°$.

Figure 3.8: x axis zoom for a selection of four poloidal launching angles from the LSM scan.

mirror	x [cm]	y [cm]	z [cm]	w_0 [cm]	d_0 [cm]	β [deg]	$\alpha(q=3/2)$ [deg]	$\alpha(q=2)$ [deg]
USM	684.6	0	439.3	2.9	213.4	20	57.2	48.2
LSM	690	0	418	2.1	162	18	52	41.4

Table 3.2: Launch parameters and beam parameters relative to the simulations of propagation in the old version of ITER reference "scenario 2", for four beams launched from the USM and LSM of the Upper Launcher aiming to the $q = 3/2$ and $q = 2$ rational surfaces. Here, for brevity, (x, y, z) stand for the laboratory frame coordinates ($x_{\rm lab}$, $y_{\rm lab}$, $z_{\rm lab}$).

		δ resonance		Δ resonance		percentage differences	
mirror	q	$(dP/dV)_{\max}$ [MW/m^3]	$\overline{\Delta\rho}$	$(dP/dV)_{\max}$ [MW/m^3]	$\overline{\Delta\rho}$	$(dP/dV)_{\max}$ [MW/m^3]	$\overline{\Delta\rho}$
LSM	3/2	0.0568	0.0168	0.0556	0.0176	2.1 %	4.8 %
LSM	2	0.0778	0.0108	0.0718	0.0119	7.7 %	10.2 %
USM	3/2	0.0427	0.0229	0.0388	0.0256	9.1 %	11.8 %
USM	2	0.0446	0.0190	0.0417	0.0206	6.5 %	8.4 %

Table 3.3: The same as Table 3.1, for the cases of Fig. 3.9.

and the USM and LSM positions are relative to the 2010 status of the Upper Launcher design. The profiles parameters are summarized in Table 3.3. The percentage differences between the peaks and the widths of the profiles computed with normal and the broadened absorption models are in agreement with those obtained in the previous simulations, being at most of the 10 percent.

Beam parameters along the propagation

For completeness, in Fig. 3.10 the principal beam parameters related to the transversal spectrum computation and the $\Delta k_{\parallel}$ are represented in function of the arc length s_{11} along the reference ray, in order to appreciate the actual values of the spectrum widths that result in the differences between the δ resonance model and the broadened model. Differently from previous works (cf. for example Farina-Ramponi [14]) the spectrum widths in the plasma are computed taking into account the effects of the plasma propagation, as it was shown in the previous sections, instead of approximating them with the free-space value $2/w_0$, w_0 being the equivalent free-space waist size of the beam. As it was expected, the plasma introduces an astigmatism and the free-space curvature radius and beam size split into two branches in the plasma, relative to the directions of the constant phase and constant amplitude ellipses axes respectively. As a consequence also the transversal spectrum width, equal to $2/w_0$ in free-space, splits into two branches after the plasma entrance.

A spike is observed in one of the two inverse curvature radius branches, in correspondence of the vacuum-plasma interface (the reference ray plasma entrance is represented by a red vertical line). Therefore a spike is present also in the spectrum widths, because

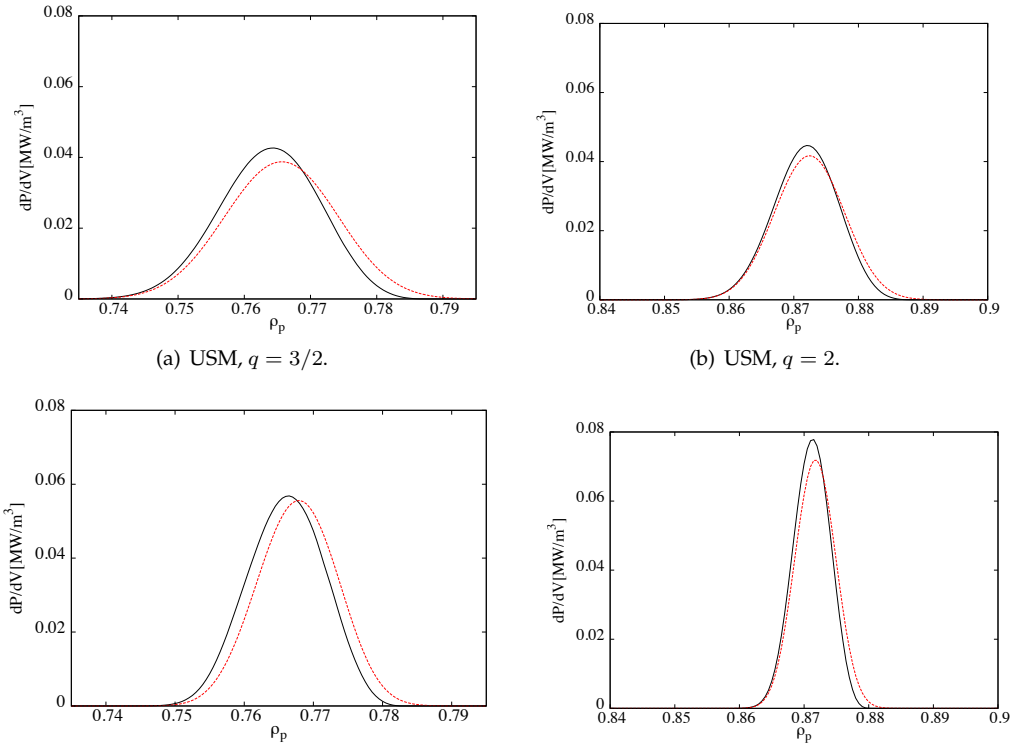

(a) USM, $q = 3/2$.

(b) USM, $q = 2$.

(c) LSM, $q = 3/2$.

(d) LSM, $q = 2$.

Figure 3.9: The same as Fig. 3.8, for the simulations performed considering the old version of ITER reference "scenario 2", with launch parameters and beam parameters contained in Table 3.2. The power density profiles are represented in function of the poloidal flux coordinate ρ_p instead of the toroidal flux coordinate ρ.

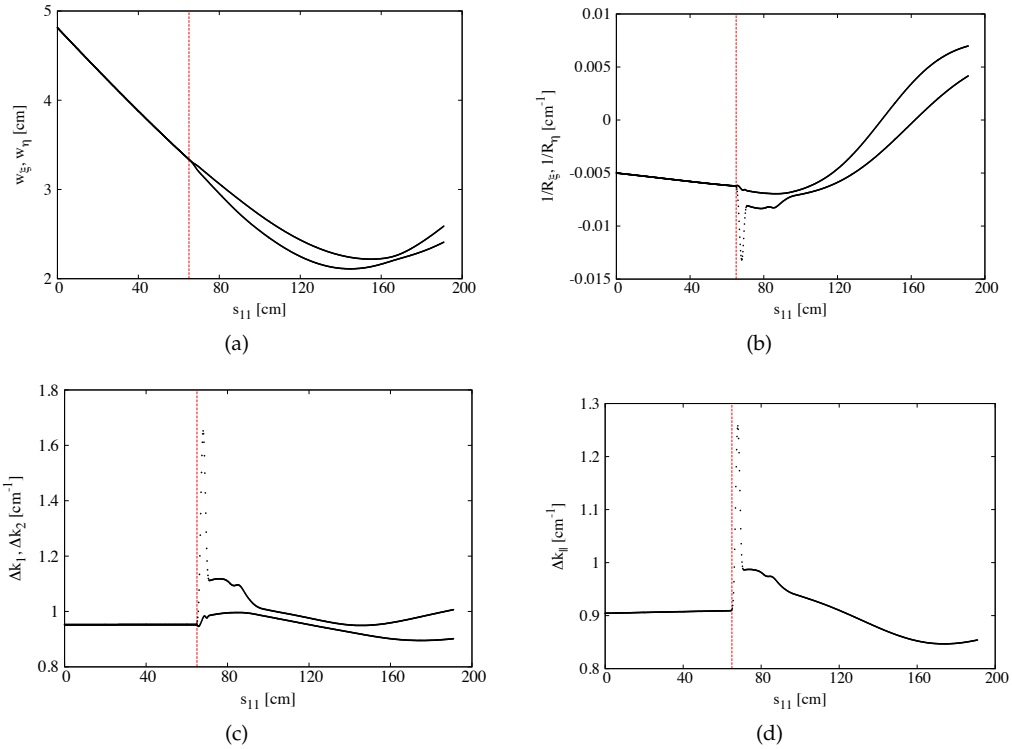

Figure 3.10: Principal beam parameters involved in the resonance broadening. The beam widths (a) and the inverse phase front curvature radii (b) as a function of the reference ray arc length s_{11}. The spectrum widths in the directions defined by the principal axes of the elliptic contours of (3.24) in the (k_x, k_y) plane (c) and the parallel width $\Delta k_{|||}$, as defined in section 3.4 (d). The red vertical lines indicate the intersection between the reference ray and the vacuum-plasma interface.

they are related to the curvature radii by the components of the M matrix (3.21). The origin of the peak in the inverse curvature radius graph is a consequence of the fact that at the plasma boundary the beam front is partly inside and partly outside the plasma. As a consequence the inner part of the front is refracted while the outer part in free space continues propagating in the same direction. Therefore the phase front is distorted in the direction perpendicular to the intersection of the front with the plasma boundary. However, once the beam has propagated for $\Delta s_{11} \sim 30\ \mathrm{cm}$ into the plasma, the inverse curvature radius recovers normal values, that are not affected by the border effect. As a consequence, this feature does not affect the absorption computation, because the absorption is computed far inside the plasma, where these border effects do not play any role.

In order to explain this behavior, a simulation has been made considering the simpler geometry of an equatorial injection. Three beams have been considered, aiming at the same point $\bar{x} = (824\ \mathrm{cm}, 0\ \mathrm{cm}, 70\ \mathrm{cm})$ on the intersection between the plasma boundary and the equatorial plane at a fixed toroidal angle. The three beams are launched from the same distance $\delta = 57.7\ \mathrm{cm}$ with different launching angles. "beam 1" is injected with null poloidal and toroidal launching angles, "beam 2", with launch point displaced

beam	x [cm]	y [cm]	z [cm]	α [deg]	β [deg]	$w_{0\xi}$ [cm]	$w_{0\eta}$ [cm]	d_0 [cm]
1	881.7	0	70	0	0	2.1	2	101.7
2	874	0	98.8	30	0	2.1	2	101.7
3	874	-28.8	70	0	30	2.1	2	101.7

Table 3.4: The launching parameters and the beam parameters of the three simulations performed in order to show the meaning of the peak in the inverse phase front curvature radii graph of Fig. 3.10 (b) are displayed.

vertically, is injected with $\alpha = 30°$, $\beta = 0°$, while "beam 3", with launch point displaced horizontally, is injected with $\alpha = 0°$, $\beta = 30°$. The launching parameters and the beams parameters are summarized in Table 3.4.

From the results it appears that for "beam 1" the spike is negligible compared to those of "beam 2" and "beam 3", because it enters the plasma perpendicularly. Focusing on the latter beams, the spike occurs in the horizontal direction for "beam 3", which crosses the vacuum-plasma interface from the side, while it occurs in the orthogonal direction for "beam 2" coming from above. In both cases the spikes occur in the directions perpendicular to the intersection between the beam phase front and the vacuum-plasma surface, indicating that the effect is well explained by the fact that at this interface the curvature in that direction has an anomaly related to the fact that the front is partly inside and partly outside the plasma, with different index of refractions in the two regions.

Let us now show these results in detail, looking at the data. In Fig. 3.11 (a) the inverse curvature radii are represented in function of the reference ray arc length for the "beam 1". As in Fig. 3.10, the red vertical line represents the reference ray plasma entrance. In Fig. 3.11 (b), (c), (d) a zoom around the vacuum-plasma is shown for the "beam 1", "beam 2" and "beam 3" respectively, with the superposed φ_R graph, where φ_R represents the angle between the ξ axis and the local x axis (that lies in the horizontal plane by definition) in the plane perpendicular to the reference ray wave vector (cf. Appendix E.2). As it can be seen in Figures 3.11 (b), (c), (d), this angle is small in both the three cases, and therefore the ξ axis lies approximately in the horizontal plane. By inspecting Figures 3.11 (c) and (d) it follows that for "beam 2" the peak is related to the η axis, while for "beam 3" it is related to the ξ axis, lying in the horizontal plane. Since the ξ and η axes are perpendicular to each other, it follows that the phase front deformation is in the horizontal direction for the "beam 3" , injected with non vanishing toroidal angle, while it is in the direction perpendicular to the local x axis in the plane perpendicular to k_{11} for the "beam 2", injected with non vanishing poloidal angle.

Conclusions

The obtained results are in qualitative agreement with those shown in the work by Farina-Ramponi [14], obtained with a version of the same code (GRAY), implemented with a different EC resonance broadening model, that does not take into account the plasma propagation effects on the transversal spectrum widths (the free space value $2/w_0$ is fixed along the plasma propagation), and a different way to include the B non-uniformity. Moreover, the results are also in qualitative agreement with those obtained

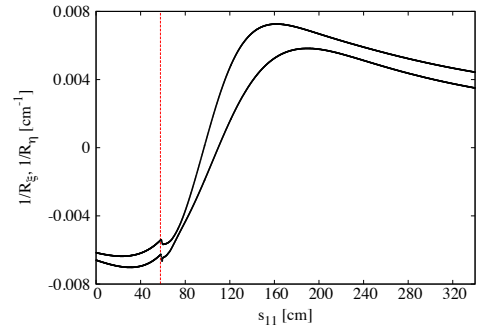

(a) $\alpha = \beta = 0°$ ("beam 1").

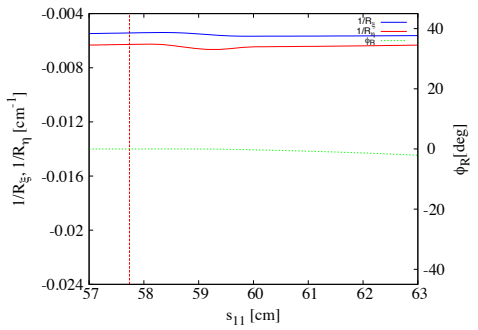

(b) $\alpha = \beta = 0°$ ("beam 1"), zoom.

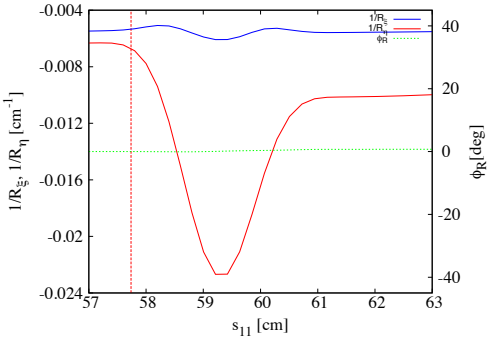

(c) $\alpha = 30°$, $\beta = 0°$ ("beam 2"), zoom.

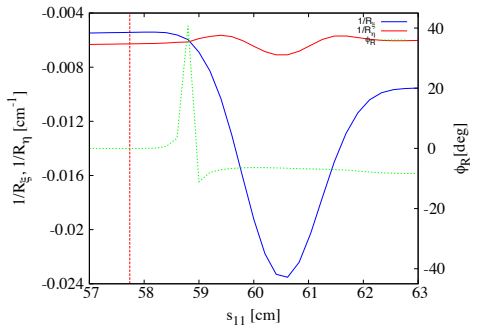

(d) $\alpha = 0°$, $\beta = 30°$ ("beam 3"), zoom.

Figure 3.11: In (a) the inverse phase front curvature radii behavior is shown versus s_{11} for the "beam 1", along all the propagation. The red vertical dotted line indicates the intersection between the reference ray and the vacuum-plasma interface. In (b) a x-axis zoom of (a) is presented, with the additional φ_R graph. The blue line is relative to the inverse curvature radius in ξ direction, while the red one is relative to the η direction. (c) and (d) are the analogous of (b) for "beam 2" and "beam 3" respectively.

by Bertelli et al. in [15], using a different Quasi-Optical code [16], that is based on a model that generalizes the parabolic wave equation for wave propagating in isotropic media (Fock and Leontovic) to anisotropic media with spatial dispersion, describing both the beam propagation and absorption using the weakly relativistic dispersion tensor.

From the above analysis it follows that the finite beam width effects on the power density profiles are small ($< 10\%$) but not negligible. Nevertheless, they do not affect substantially the results obtained without taking them into account. As a consequence, the simulations relative to the ITER Upper Launcher design presented in the following chapter have been made with the current reference version of the GRAY code, that uses the simpler δ resonance model to compute the beam absorption.

Finally, as future work, in order to have a precise estimate of the finite beam width effects on the ECCD process, these effects should be included also in the current drive computation.

CHAPTER 4

The ITER Upper Launcher Design: ECRH&CD simulations with the GRAY code

In the introduction (cf. section 0.3) it was pointed out that the ITER Upper Launcher design is still in progress. The work presented in this chapter is setted into this framework, and has been done under contract with Fusion For Energy (F4E), that is the European Union's Joint Undertaking for ITER and the Development of Fusion Energy. This organization, created by a decision of the Council of the European Union, is primarily responsible for providing Europe's contribution to the ITER project.

The UL will be devoted primarily to the control of NTM instabilities, therefore the total injected EC power and the launching angles have to be chosen in order to guarantee the modes stabilization around the $q = 3/2$ and $q = 2$ rational surfaces. In the present design of the UL system four beams of 1 MW each are reflected on either the USM or the LSM in each of the four launchers, and as a consequence 16 MW can be launched by either the USM or the LSM globally. In reality there are losses in the waveguides and in the optical system, so that the final available value is lowered to $P_{EC,max} = 13.3$ MW.
Each beam will be injected with almost fixed toroidal angle β (the actual reference value is $\beta = 20°$), varying the poloidal angle α with a steering mechanism. The optimal β angle has to be chosen in order to maximize the NTM stabilization efficiency, ensuring that the 13.3 MW of available EC power are sufficient to control the NTM modes evolution around the rational surfaces. This task, that presupposes a detailed analysis of the considered ITER scenario, has to be done taking into account the constraints on the toroidal and poloidal launching angles imposed by the geometry of the mirror steering system.

Part of the thesis work has been devoted to this task. Here it is presented the analysis of the new ITER H-mode plasma discharge scenario denoted "Scenario 1" (considered as the reference ITER baseline scenario), with the determination of the minimum total EC power required to stabilize the NTM modes at the rational surfaces in function of the angle β at a fixed time and, once fixed β, along the discharge. This work has been done by means of numerical simulations performed with the GRAY beam-tracing code.

The minimum EC power required to stabilize the NTM modes can be computed using two stabilization criteria (cf. Zohm et al. [17] and Sauter et al. [18]). As an introduction, a review is presented of the derivation of these criteria, according to Poli et al. [19] .

4.1 Criteria for NTM stabilization

In order to obtain a stabilization criterion for a NTM mode, it is needed to know the time evolution equation for the width of the associated magnetic island. Let us consider

the full width w of a magnetic island whose evolution is due to a Neoclassic Tearing Mode and undergoing a ECCD process. Its time variation is governed by the modified Rutherford equation, written here in a simplified form (cf. Poli et al. [19]):

$$\frac{\tau_R}{\rho_s^2|\Delta'|}\frac{d\mathrm{w}}{dt} \sim -1 + \frac{\mathrm{w}_{sat}}{\mathrm{w}} - 5.05\frac{\mathrm{w}_{CD}\mathrm{w}_{sat}}{\mathrm{w}^2}\frac{J_{CD}}{J_{bs}}\eta_{CD}\ , \tag{4.1}$$

where the saturated island width w_{sat} expresses the balance between the neoclassical (bootstrap) drive and the stabilization due to the equilibrium current profile in the absence of ECCD, w_{CD} is the width of the ECCD current profile (defined as $a_0 \times \nabla\rho$, where a_0 is the mid plane minor radius and $\nabla\rho$ the full ECCD current density profile width at $1/e$), η_{CD} is the current drive stabilization efficiency, J_{CD} is the peak of the ECCD deposited current density, J_{bs} is the bootstrap current density at the surface of interest, ρ_s is the minor radius of the resonant surface, τ_R is the resistive time and $\Delta^{'}$ is the "tearing stability index". The first term on the right-hand side is the stabilizing contribution from the equilibrium current density at large island size, the second term is the driving term from the perturbed bootstrap current, while the third term is the stabilizing ECCD contribution. The right hand side can be made negative for all w, requiring that no roots of the equation

$$\mathrm{w}^2 - \mathrm{w}_{sat} + 5.05\mathrm{w}_{CD}\mathrm{w}_{sat}\frac{J_{CD}}{J_{bs}}\eta_{CD} = 0 \tag{4.2}$$

exist (unconditional stability), i.e. that its discriminant is negative. This results in the following criterion:

$$\frac{\mathrm{w}_{CD}}{\mathrm{w}_{sat}}\frac{J_{CD}}{J_{bs}}\eta_{CD} > \frac{1}{20}\ . \tag{4.3}$$

This is a sufficient (but not necessary) condition of stability. It is useful to distinguish between the two limiting cases in which the ECCD profile is broader or narrower than the typical island width w_{marg} at which stabilization occurs.

Let us consider the case $\mathrm{w}_{CD} > \mathrm{w}_{marg}$. In this limit the stabilization efficiency for modulated injection can be approximated by

$$\eta_{CD} \simeq 0.15\mathrm{w}/\mathrm{w}_{CD} \tag{4.4}$$

and instead of using (4.3) it is more practical to exploit the fact that in ITER it can be assumed that w_{marg} is much smaller than w_{sat}, so that the first term on the right hand side of Eq. (4.1) can be dropped near marginal stability. Substituting (4.4) into (4.1), dropping the -1 term and forcing the right hand side to be negative, it follows that approximately $\eta_{NTM} > 4/3$. Including the reduction of the neoclassical drive due to geodesic-curvature effects, it follows the criterion

$$\eta_{NTM} \equiv \frac{J_{CD}}{J_{bs}} > 1.2\ , \tag{4.5}$$

that is the first requirement for a complete stabilization of NTMs used to assess the performance of the ITER upper launcher, where η_{NTM} is called "NTM efficiency".
For continuous injection $\eta_{CD} \simeq 0.1\mathrm{w}^2/\mathrm{w}_{CD}^2$ and the previous criterion should be replaced by

$$\eta_{NTM} > 2\frac{\mathrm{w}_{CD}}{\mathrm{w}} \tag{4.6}$$

i.e. complete stabilization $(\mathrm{w} \to 0)$ can be achieved in this model only with an infinite ECCD current (no effects leading to stability of small islands are considered in the above derivation) so that modulation is essential.

Now let us consider the opposite case $\mathrm{w}_{CD} < \mathrm{w}_{marg}$. In this limit the stabilization efficiency is approximately $\eta_{CD} \simeq 1/3$ for both continuous and modulated injection. It follows that Eq. (4.3) becomes

$$\frac{\mathrm{w}_{CD}}{\mathrm{w}_{sat}} \frac{J_{CD}}{J_{bs}} > \frac{3}{20} \,. \tag{4.7}$$

For a saturated island width of the order of 30 cm, this condition yields

$$\eta_{NTM} \mathrm{w}_{CD} > 4.5 \text{ cm} \,, \tag{4.8}$$

which is in quite good agreement with the stabilization criterion

$$\eta_{NTM} \mathrm{w}_{CD} > 5 \text{ cm} \tag{4.9}$$

known from literature. From the physical point of view, the difference in the criteria to be adopted depending on the width of EC deposition profile compared to the marginal island width reflects the fact that once the EC power is deposited inside the island there is little gain from further narrowing the profile, as the driven current already possesses the correct helicity to stabilize the mode, so that the total driven current becomes the figure to be optimized. Now, considering that the peak in the current density profile is proportional to the injected power, that is

$$J_{CD} \propto P_{in} \,, \tag{4.10}$$

it follows that the two criteria (4.5) and (4.9) can be rewritten as follows

$$P_{in} > P_{eta}[MW] = \frac{1.2}{\eta_{NTM(1MW)}} \,, \tag{4.11}$$

$$P_{in} > P_{etaw}[MW] = \frac{0.05}{\eta_{NTM(1MW)} \mathrm{w}_{CD}[\mathrm{m}]} \,, \tag{4.12}$$

where $\eta_{NTM(1MW)}$ refers to 1 MW of injected power.

The first criterion is valid in the limit of large w_{CD} while the second considering small w_{CD}. However, we note that w_{CD} values larger than 0.03 m are desirable to reduce aiming and/or misalignment problems.

4.2 ITER scenario analysis with NTM stabilization power determination

The main results of the EC performance analysis done on the ITER H-mode scenario denoted as "Scenario 1" are presented here. The available data relative to this Scenario contain all the physical informations about the discharge, such as the magnetic field equilibrium configuration and electron density, electron temperature, plasma current, safety factor, bootstrap current profiles at discretized values of the time (in the range $0\ s < t < 700\ s$). Calculations have been performed with the EC beam-tracing code GRAY. The reference value for the injected power is $P_{EC} = 1$ MW in the analysis presented here. Note that linear codes are used for ECRH&CD simulations, so that all the results scale linearly with the injected power.

The analysis can be divided into three main sections: 1) the presentation of the time variation of the most important physical variables of the scenario and the specification of the beams parameters; 2) the detailed study of the time slice $t = 520\ s$, relative to the end of the flat top of the plasma current, with characterization of the ECCD current density peak J_{CD} and the total driven current I_{CD} over a wide range of steering angles α and β, in order to establish the minimum EC power required to stabilize NTM modes on the $q = 2$ and $q = 3/2$ rational surfaces using the two criteria given in section 4.1; 3) determination of the NTM stabilization power time variation, slightly varying the toroidal steering angle β around the reference design value $\beta = 20°$.

I will present in detail the results for the injection from the Upper Steering Mirror (USM), while I will give only a few comments on the Lower Steering Mirror (LSM) results, that are similar.

4.2.1 Scenario assessment and beams parameters

The assessment of Scenario 1 has been performed with the goal to revise the radial range of occurrence of the resonant surfaces and to select a set of time slices to be used for H&CD calculations.
The 0D parameters of the scenario are the following: plasma major radius $R_0 = 6.2$ m; plasma minor radius $a_0 = 2$ m; toroidal field strength at $R_0 = 5.3$ T; plasma fuel: 1:1 deuterium-tritium mixture; flat-top plasma current $= 15$ MA.

In Fig. 4.1 the time evolutions of peak electron density and temperature, of the safety factor and of the plasma current are shown. The current flat-top is reached at $t = 80$ s and lasts till $t = 530$ s (H-mode phase). For 50 s after the L-H transition ($t = 80$ s) the electron density varies up to its maximum peak value of about $1.1 \times 10^{20}\ m^{-3}$, while the central temperature shows a sharp peak up to 38 keV and then decreases to about 25 keV.

The time evolution of the radial position of the rational surfaces $q = 2$ and q=3/2, where the NTM stabilization has to be done, and of the relative value of the bootstrap current, is shown in Fig. 4.2. The radial position of the rational surfaces is indicated by the flux coordinate ρ (i.e. the square root of the toroidal flux, normalized to 1 at the plasma edge, cf. section 0.2). It is important to know at every time the values $\{\rho(q)\ ,\ q = 2, 3/2\}$ because, since $\rho(\alpha, \beta)$ is given as output from the code after every simulation, this allows to find, for every fixed value of β, the α value such that the power deposition occurs around the considered rational surface.

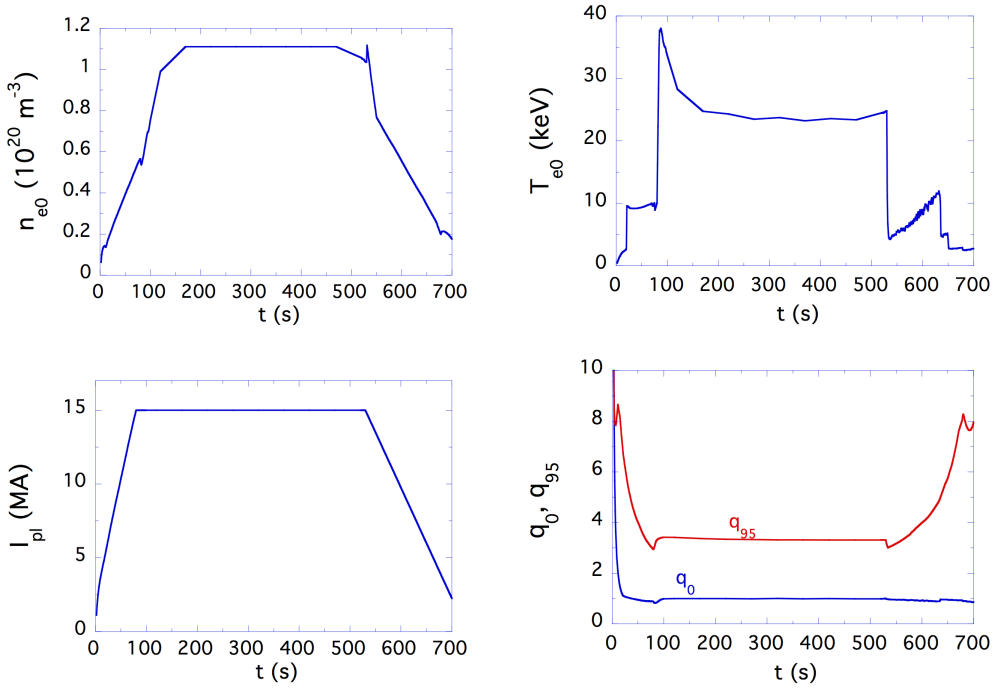

Figure 4.1: Time evolution of peak electron density, temperature, safety factor q_0 $(q(\rho = 0))$ and q_{95} $(q(\rho = 0.95))$, and plasma current for Scenario 1.

The simulations are performed with a "virtual beam" starting from the center of either the USM or LSM. Table 4.1 shows the complete list of the beam parameters given in input to the GRAY code. For sake of simplicity, all the GRAY simulations have been made rotating the laboratory coordinate system such that the launching point is located in the poloidal plane $(y_{\rm lab} = 0)$. Due to tokamak approximate axisymmetry, disregarding magnetic ripple effects, this does not affect any of the obtained results.

Mirror	x(m)	y(m)	R(m)	z(m)	w_0(m)	d_0(m)	w(m)	R_c(m)
USM	6.998	-0.123	6.999	4.414	0.029	2.134	0.05047	-3.186
LSM	7.053	-0.082	7.054	4.178	0.021	1.620	0.04813	-2.010

Table 4.1: Coordinates of the launching point of the virtual beams from the two mirrors and beam parameters. x, y, z are the mirror coordinate in the laboratory frame, $R = \sqrt{x^2 + y^2}$, w_0 is the vacuum-equivalent waist size, d_0 is the vacuum-equivalent waist distance from the mirror, w is the beam size at the mirror and R_c is the curvature radius at the mirror.

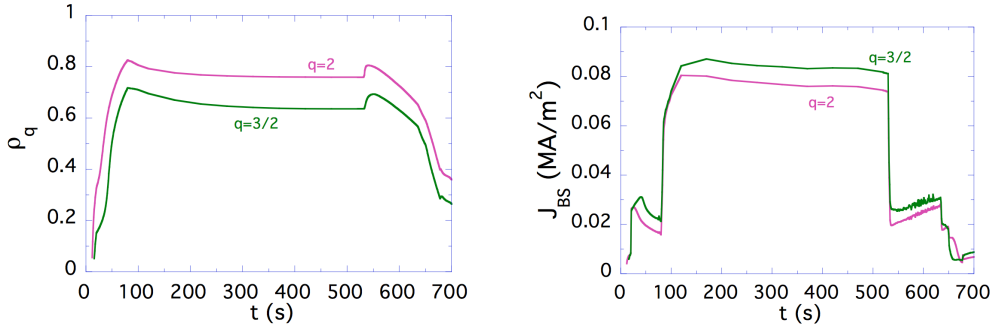

Figure 4.2: Time evolution of ρ and J_{bs} on the $q = 2$ (pink) and $q = 3/2$ (green) surfaces of Scenario 1.

resonant surface	ρ	$n_e(10^{19}\ \mathrm{m}^{-3})$	$T_e(\mathrm{keV})$	$J_{bs}(\mathrm{MA/m^2})$
$q = 2$	0.759	9.58	7.24	0.0745
$q = 3/2$	0.638	9.73	8.91	0.0816

Table 4.2: Plasma parameters at $q = 2$ and $q = 3/2$ for $t = 520$ s.

4.2.2 Fixed time analysis at the end of the current flat-top and NTM stabilization power determination

The ECCD performance of the plasma scenario at the end of the current flat-top ($t = 520$ s), i.e. close to the end of the burning phase, has been evaluated by means of beam tracing calculations using the data reported in Table 4.1.
The density, temperature, safety factor and bootstrap current profiles are presented in Fig. 4.3 for $t = 520$ s. The violet and green lines in the q profile indicate the $q = 2$ and $q = 3/2$ rational surfaces respectively, located at $\rho(q = 2) = 0.759$ and $\rho(q = 3/2) = 0.638$. The complete list of the plasma parameters on the rational surfaces is given in Table 4.2.

The ECCD results obtained from a wide scan in the poloidal and toroidal injection angles ($25° \leq \alpha \leq 65°$, $15° \leq \beta \leq 25°$, with $\Delta\alpha = \Delta\beta = 1°$) are summarized in Figure 4.4 and 4.5. The upper graphics show a contour plot of the peak current density (left) or the total driven current (right) in the (α, β) plane, with a superposed contour plot of the ρ values. These plots characterize the overall behavior of J_{cd} and I_{cd} versus (α, β). The same data are shown versus ρ at various β (lower graphics).
The current density shows a weak dependence on β with an quite broad "maximum" for $18° \leq \beta \leq 20°$, with $25° \leq \alpha \leq 65°$. In order to apply the stabilization criterion (4.12) it is important to consider I_{cd} versus (α, β) too, because $I_{cd} \propto J_{cd}\, w_{cd}$ at fixed radial position ρ. As it can be seen from the top-right graphic in Fig. 4.4, the EC current I_{cd} increases globally both with α and β, and in particular the EC current driven at a given "radius" ρ increases with increasing the toroidal launching angle for $15° \leq \beta \leq 25°$ as expected, because the parallel component $k_{\|}$ of the wave vector increases with increasing β and the current drive process becomes more and more efficient.
The LSM presents overall similar results, with higher values of J_{cd} for a given β, due to the smaller size of the beam with respect to that of USM (see Table 4.1). In Fig. 4.5 the

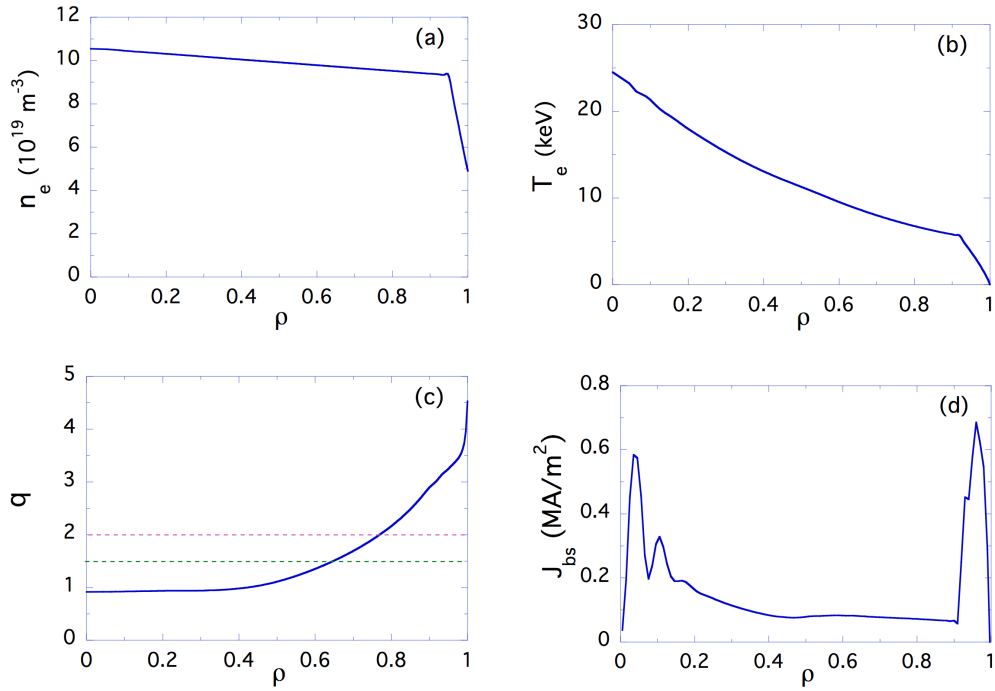

Figure 4.3: Radial profiles of electron density (a), temperature (b), safety factor (c), and bootstrap current (d) at t=520 s.

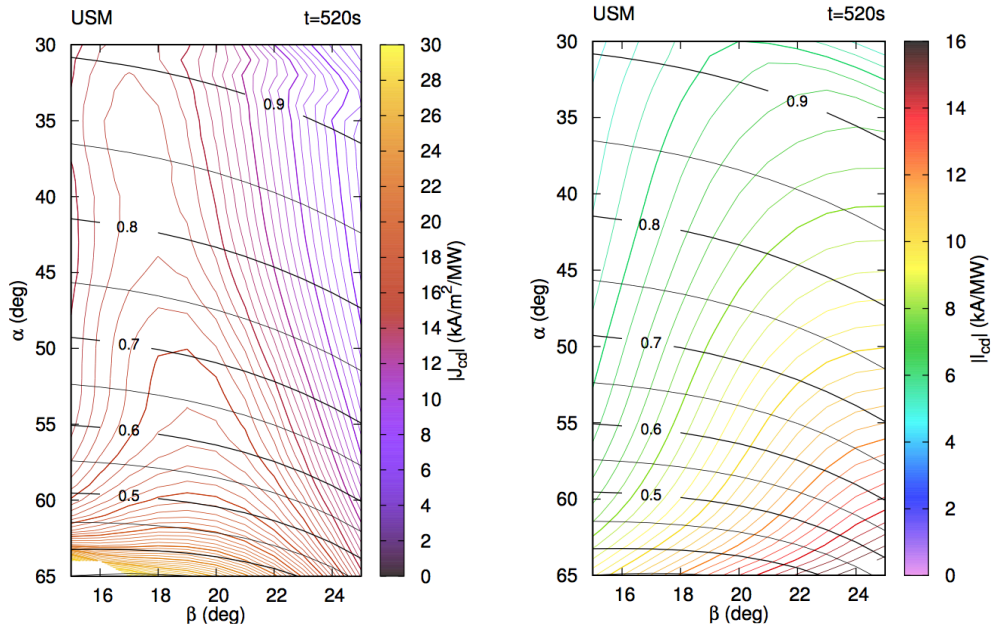

Figure 4.4: Contours of EC driven current density per unit injected power (left) or EC driven current per unit injected power (right), and of radial location ρ (black) versus toroidal β and poloidal α injection angles from USM, at $t = 520$ s.

radial profile of the normalized EC current density profile width $\Delta\rho$, for different values of β, is presented. This graphic shows a behavior similar to $I_{cd}(\rho)$ (Fig. 4.5, center).

Now the NTM stabilization powers P_{eta} and P_{etaw} computed according to the two criteria (4.11) and (4.12) respectively, obtained using the $J_{cd}(\alpha, \beta)$ and $J_{bs}(\rho)$ values reported in Figures 4.4 (left) and 4.3 (d), is shown as a function of β on the $q = 2$ and $q = 3/2$ surfaces, where the two criteria apply. In order to compute P_{etaw}, the current density profile width is taken as $w_{cd} = \Delta\rho\, a_0$, where we assume that $a_0 = 2$ m is the mid plane minor radius, with $\Delta\rho(\alpha, \beta)$ as reported in Fig 4.5 (bottom). Figure 4.6 shows the superimposed $P_{eta}(\beta)$ and $P_{etaw}(\beta)$ graphics at fixed ρ for $\rho = \rho(q = 2) = 0.759$ and $\rho = \rho(q = 3/2) = 0.638$. The required power P_{eta} from criterium (4.11) is minimum at $\beta \sim 18°$ and increases with β, while the required power P_{etaw} estimated using (4.12) decreases with increasing β.

The NTM stabilization power P_{stab} is estimated as the maximum of P_{eta} and P_{etaw}. The two criteria cross when $w_{cd} = 0.05/1.2$ m $= 0.042$ m and, for the cases shown in Fig. 4.6, the corresponding stabilization power P_{stab} is minimum. The β values relative to the P_{stab} minimum are $\beta \sim 19°$ for $q = 3/2$ and $\beta \sim 21°$ for $q = 2$, in agreement with the actual reference value $\beta = 20°$.

From the simple analysis summarized in the plots and in the tables reported in this section, we may conclude that, on the basis of the considered criteria, the power required for NTM stabilization is much less than the maximum EC power available from each

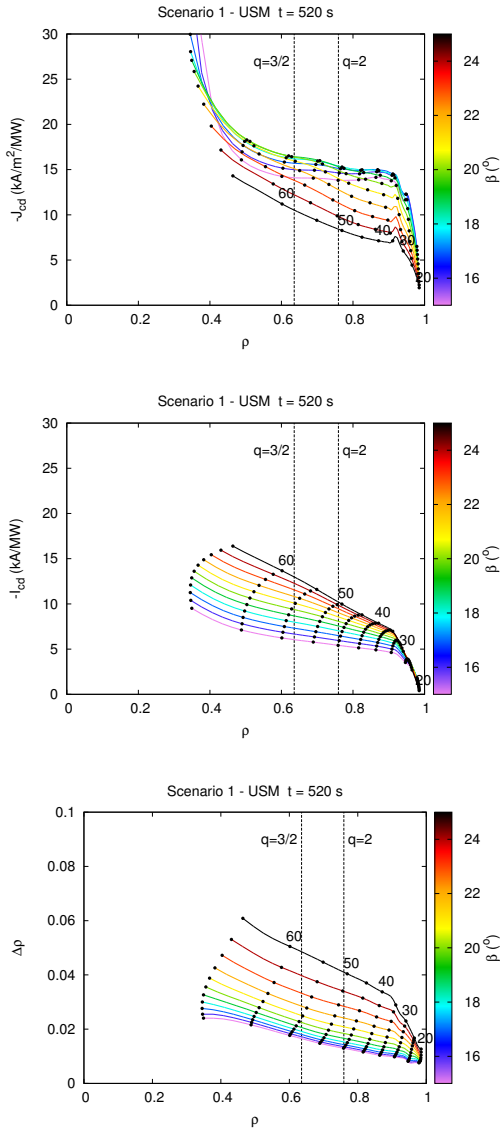

Figure 4.5: Radial variation of the ECCD current density peak per unit injected power (top), total driven current per unit injected power (center), and ECCD current density normalized full width (bottom), at $t = 520$ s, for injection from USM. Colored lines refer to different toroidal injection angles β, black dots to different poloidal injection angles α. The two vertical dotted lines indicate the radial location of the $q = 2$ and $3/2$ surfaces.

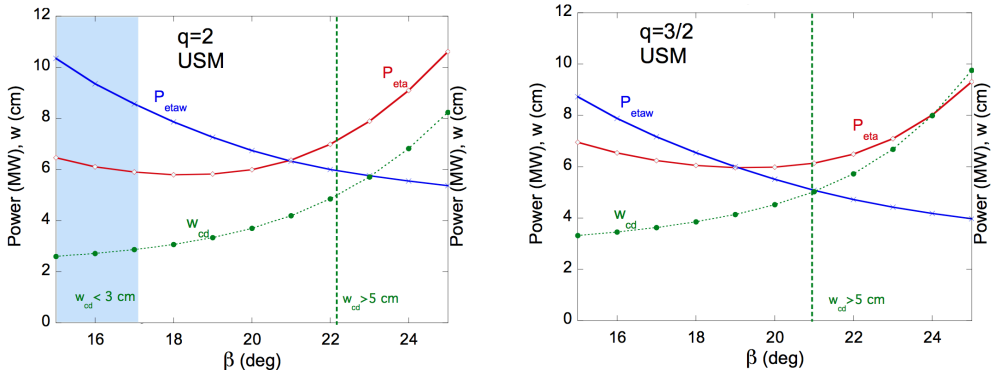

Figure 4.6: Power required for stabilization P_{eta} and P_{etaw} on the $q = 2$ (left) and $q = 3/2$ (right) surfaces given by the two criteria $\eta_{\mathrm{NTM}} > 1.2$ (red) and $\eta_{\mathrm{NTM}} w_{cd} > 0.05$ m (blue), and full width w_{cd} at $1/e$ of the current density profile (dotted green) for injection from USM. The light blue region highlighted is the parameter region for which $w_{cd} < 0.03$ m.

mirror ($P_{EC} = 13.3$ MW). However, we recall that the ECCD results refer to the case of a single "ideal" beam (the "virtual beam"), and so far no effects on profile broadening have been taken into account (e.g., four beams superposition, finite width of the k-spectrum, perpendicular diffusion, etc.). In addition, all the simulations are based on the launching conditions in Table 4.1, that do not correspond to the final UL design, still in progress. Further investigation based on the Rutherford equation taking into account the details of the physics of NTM stabilization is required to get more reliable values for the required power.

4.2.3 NTM stabilization power time variation

The NTM stabilization power has been computed for all the times, in order to estimate the Upper Launcher capability to control the instabilities during the various phases of the plasma discharge. In fact, being the total available power equal to $P_{EC} = 13.3$ MW, the Launcher is able to stabilize the NTM modes only when $P_{stab} < P_{EC}$.

The values of P_{eta} and P_{etaw} have been evaluated on the $q = 2, 3/2$ surfaces for all the times, for three fixed values of the toroidal steering angle around the reference value $\beta = 20°$. The behavior of P_{eta}, P_{etaw} and w_{cd} with $\beta = 18°, 20°, 22°$ as a function of time is shown in Fig. 4.7 for injection from USM aiming at the $q = 2, 3/2$ surfaces. In the plasma current flat-top region the stabilization power is almost constant both for the $q = 2$ and the $q = 3/2$ case. The behavior is different in the plasma current ramp-up and ramp-down regions. In fact the stabilization power in the case $q = 2$ shows two large peaks before the L-H transition ("Low confinement mode" to "High confinement mode" transition) and after the H-L transition, where it exceeds the maximum nominal available power $P_{EC} = 13.3$ MW. The observed behavior is related to the corresponding sharp variation of the electron temperature (that affects the ECCD efficiency). At the contrary, no large spikes are observed in the $q = 3/2$ case, even in the ramp-down phase.

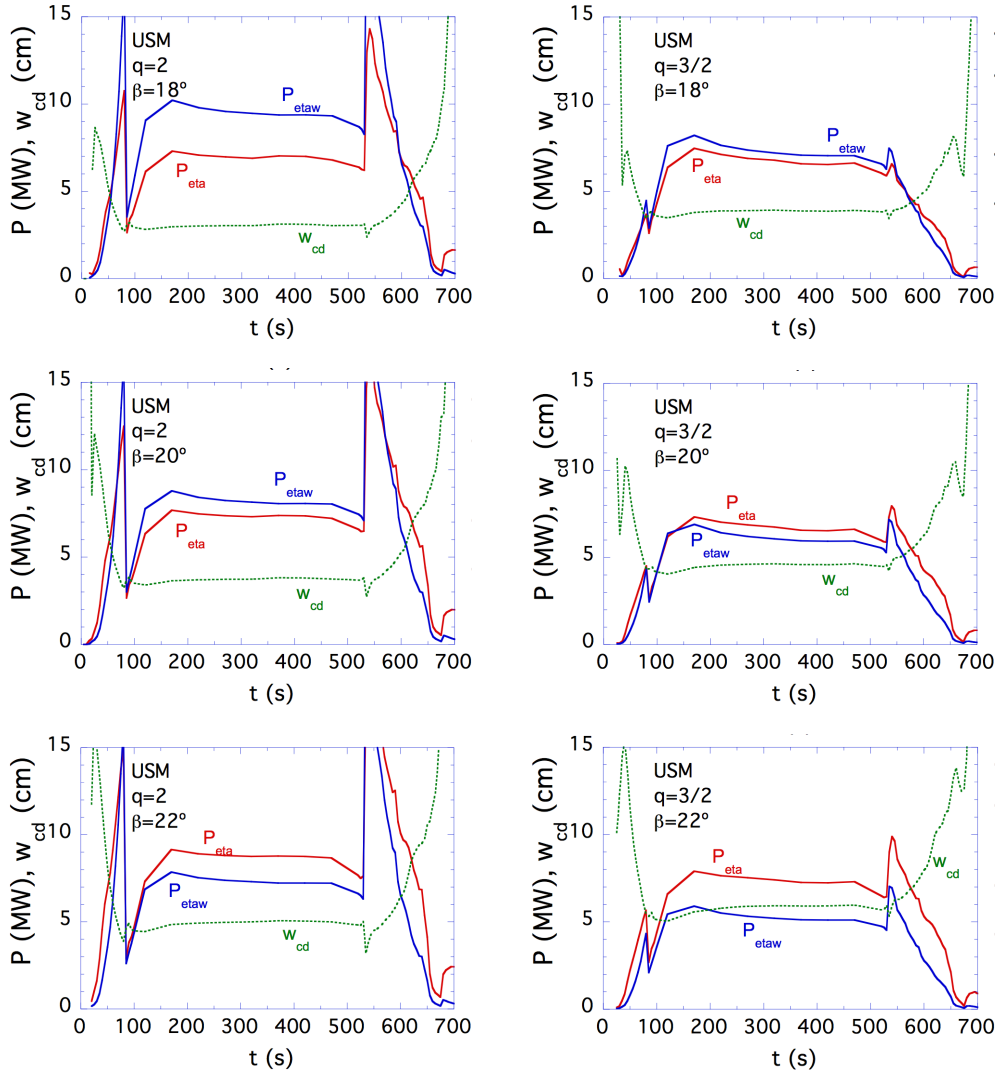

Figure 4.7: Power required for stabilization and profile width versus time from USM at $\beta = 18°$, $20°$, $22°$ (top to bottom) aiming at $q = 2$ (left) and $q = 3/2$ (right) rational surfaces.

Conclusions and future directions

In this work the propagation and absorption of electron cyclotron (EC) Gaussian beams in tokamak plasmas has been considered. This topic, of interest for nuclear fusion applications, has been investigated both theoretically and numerically. In applications like electron cyclotron resonance heating and current drive, the ratio λ/L of the beam wavelength to the plasma equilibrium quantities spatial variation scale is small (~ 0.001 in ITER Upper Launcher), so that the wave propagation can be described asymptotically in the limit $\lambda/L \to 0$. The geometrical optics (GO), able to describe correctly divergent beams far from the wave source, does not apply around the beam waists. In fact, the GO solution is obtained in terms of a bundle of rays, that intersect giving rise to a focus near to the beam waist. These rays, that far from the waist are found to be the streamlines of the wave energy flux, become meaningless near the focus, where the wave energy density shows an unphysical divergence. From the mathematical point of view, this is only a consequence of the fact that the geometrical optics rays are obtained as projections in the configuration space of the Hamiltonian orbits in the phase space that are solution of a set of Hamilton equations whose Hamiltonian is the wave dispersion function. Near caustics, like foci, this projection is not feasible and gives rise to unphysical solutions.

Amongst the various methods developed to overcome this drawback, we chose the complex eikonal method, within the complex geometrical optics (CGO) framework. This method consists in searching asymptotic solutions of the wave equation in the limit $\lambda/L \to 0$, assuming that the wave field phase function (called "eikonal") is complex valued, with the non-negative imaginary part accounting for the finite width of the beam cross section. The CGO solution is obtained in terms of a bundle of "extended rays", that take into account the diffraction effects and do not intersect in the case of focused beam, correctly describing the beam waist. Nevertheless, the eikonal imaginary part introduces a great complexity in the transport equation for the wave field along the rays, hampering the derivation of the wave energy flux. Therefore, without the connection with the energy flow, the physical meaning of the "extended rays" is uncertain. In order to fill this gap, we propose an argument that simplifies the analysis of the transport equation allowing us to derive the wave energy flux. This new result, that is not available in the literature in the case of beam propagation in anisotropic media like magnetized plasmas, constitutes the major goal of my PhD. This work has been done in collaboration with O. Maj (IPP, Garching, Germany) and published on Physics of Plasmas [1]. Moreover, an optimized version of the complex eikonal method is presented, showing that the CGO "extended rays" correctly describe the wave energy flow. This fact has an important

application, since it gives a rigorous basis at the GRAY code [6] equations. The theoretical derivation of these results is contained in chapter 1, while their numerical validation with GRAY and TORBEAM [7] codes is reported in chapter 2.

Turning to the description of the beam absorption, the electron cyclotron resonance condition has ben reviewed, in order to include the effects due to the finite beam width. This topic is important in the modeling of the interaction between focused electron cyclotron Gaussian beams and a tokamak plasma. Since the resonance condition $\omega - k_{\parallel} v_{\parallel} - n\Omega_e/\gamma$ is valid only for a plane wave that interacts for a infinite amount of time with a spatially infinite, homogeneous plasma with a uniform equilibrium magnetic field, some corrections have to be accounted for in the case of Gaussian beams propagating in tokamaks, because in this case the plasma is spatially localized, inhomogeneous and immersed in a non-uniform background magnetic field. Moreover, the beams have finite width, and in applications like current drive they are focused in order to deliver the power in a small region of plasma. As a consequence the interaction time between the electrons and the wave is finite. All these factors contribute in modifying the resonance condition. The theoretical description of this topic can be found in literature (cf. Demeio-Engelmann [8]), showing that the resonance conditions is broadened by these effects. Nevertheless, such descriptions have to be matched with the ray description of the beam obtained in the CGO framework. We propose a model that accounts for the modification in the resonance condition due to the finite width of the wave vector transversal spectrum caused by the paraxial character of the wave, that allows us to compute the beam absorption along the "extended rays" in a consistent way. Moreover, the resonance modification due to the non-uniformity of the equilibrium magnetic field has been taken into account by computing the absorption coefficient using the local value of the magnetic field on each ray. This model has been implemented in a modified version of the GRAY code. In order to compute the beam transversal spectrum, it has been assumed that the wave field maintains its transversal Gaussian shape along the plasma propagation, in order to apply a local Gaussian model and compute the spectrum analytically. This behavior has been verified in low density conditions (like in ITER), computing the spectrum numerically via 2D fast Fourier transform with the GRAY code. This new version of the code can be used to compute the transversal spectrum in critical situations, where for example the high density enhances the plasma astigmatism and the beam looses its transversal Gaussian form. Using this absorption model, the power absorption radial profiles have been computed, and compared with the standard "plane wave" ones. The profiles obtained with the "broadened resonance" are broadened respect to the "delta resonance" ones, but the differences are small, in agreement with previous works on the subject (Farina-Ramponi [14] and Bertelli et al. [15]). As a consequence the usual "plane wave" model can be used for practical purposes. All the theory and numerical examples about this topic are contained in chapter 3.

The electron cyclotron current drive performances have been evaluated with the GRAY code in the ITER reference plasma discharge scenario denoted as "Scenario 1", using the usual "plane wave" model. This task has been done in order to estimate the EC power required to stabilize the neoclassical tearing modes, particularly dangerous plasma instabilities, that can be controlled by injecting focused EC Gaussian beams in the plasma regions where the modes develop. This analysis is of interest for the ITER Upper Launcher (UL) design. The stabilization power, computed according to two standard criteria (cf. section 4.1), has been evaluated all along the plasma discharge, with the result that the available power from the UL is sufficient except in the L-H and H-L transitions in

certain cases (L indicates the "low confinement mode" and H the "high confinement mode"). Moreover, the optimal toroidal steering angle relative to the minimum stabilization power required has been estimated, with results consistent with the actual reference value $\beta = 20°$ for both the UL mirrors. This analysis is contained in chapter 4.

Finally, let us mention some future developments. A mathematically rigorous EC resonance broadening model has to be substituted to the actual one. This research task is related to the estimation of the parallel (to B) wave vector spectrum width. The arbitrariness on the computation of the $k_{\|}$ spectrum (described in section 3.2.2) has to be removed by a clearer understanding of the subject. At the same time, the GRAY code will undergo constant revisions, in order to keep it in step with the theoretical work. Numerical simulations of ECRH & CD in ITER scenarios will continue in order to contribute to the analysis of the ITER EC system.

Appendices

APPENDIX A

Ohm's law in a cold stationary plasma and $D = \epsilon E$ local constitutive relation

The general non-local, causal and linear relation between current density and electric field in a plasma slightly non-uniform spatially and temporally can be written in the symmetrized form

$$J(x,t) = \int \mathrm{d}x^{'} \int_{-\infty}^{t} \mathrm{d}t^{'} \hat{\sigma}(x - x^{'}, t - t^{'}, \frac{x + x^{'}}{2}, \frac{t + t^{'}}{2}) E(x^{'}, t^{'}) \,, \tag{A.1}$$

where the tensor $\hat{\sigma}$ is a function rapidly varying in the difference arguments and slowly varying in the sum arguments. The difference arguments represent the spatial and temporal dispersion, while the sum arguments represent the disuniformity of the medium. In our case the medium is stationary, that is $\hat{\sigma}$ is independent from $(t + t^{'})/2$, and spatially non-dispersive, that is the $x - x^{'}$ dependence of $\hat{\sigma}$ is given by a Dirac δ function of argument $x - x^{'}$. As a consequence

$$J(x,t) = \int \mathrm{d}x^{'} \int_{-\infty}^{t} \mathrm{d}t^{'} \hat{\sigma}(t - t^{'}, \frac{x + x^{'}}{2}) \delta(x - x^{'}) E(x^{'}, t^{'}) = \int_{-\infty}^{t} \mathrm{d}t^{'} \hat{\sigma}(t - t^{'}, x) E(x, t^{'}) \,. \tag{A.2}$$

We consider a stationary plasma and a wave source with fixed angular frequency ω, and as a consequence the temporal dependence of the field can be described by a factor $e^{-i\omega t}$, that is

$$E(x,t) = E(x) e^{-i\omega t} \,. \tag{A.3}$$

Changing integration variable from $t^{'}$ to $t^{''} = t^{'} - t$, taking into account (A.3) and introducing the conductivity tensor as

$$\sigma(\omega, x) = \int_{0}^{\infty} \mathrm{d}t^{''} \hat{\sigma}(t^{''}, x) e^{i\omega t^{''}} \,, \tag{A.4}$$

it follows that

$$J(x,t) = \sigma(\omega, x) E(x,t) \,. \tag{A.5}$$

Now, introducing the dielectric tensor

$$\epsilon(\omega, x) = I + \frac{4\pi i}{\omega} \sigma(\omega, x) \,, \tag{A.6}$$

it follows that the constitutive relation between the electric displacement D and the electric field E is local, namely

$$D(x,t) = \epsilon(\omega, x) E(x,t) \,. \tag{A.7}$$

APPENDIX B

Gaussian beams and Quasi-Optical approximation

In this appendix the expression of the electric field of a non-astigmatic Gaussian beam propagating in vacuum is reviewed and, considering it as a solution of the paraxial wave equation, the approximation that lead to this equation is presented in detail, showing how it is connected with the QO approximation as the beam enters the plasma.

The expression of the electric field of a non-astigmatic (with cylindrical symmetry) Gaussian beam propagating in the z direction, is well known. Considering a monochromatic beam under the so-called "scalar approximation" where the e.m. fields are uniformly (e.g.linearly or circularly) polarized, the wave electric field can be described by a scalar quantity $E(x, y, z, t)$. Assuming a $e^{-i\omega t}$ time dependence, that is

$$E(x, y, z, t) = E(x, y, z)e^{-i\omega t} \,, \tag{B.1}$$

$E(x, y, z)$ is given by

$$E(x, y, z) = E_0 \frac{w_0}{w(z)} e^{-i\phi_{\mathrm{Gouy}}(z)} e^{-\frac{x^2+y^2}{w(z)^2}} e^{ik_0\left[z+\frac{x^2+y^2}{2R(z)}\right]} \,. \tag{B.2}$$

where $E_0 = E(0, 0, 0)$, $w(z)$ and $R(z)$ represent the beam size and the curvature radius of the phase fronts respectively, with z variation given by

$$w(z) = w_0 \sqrt{1 + \left(\frac{z}{z_R}\right)^2} \,, \tag{B.3}$$

$$R(z) = z\left[1 + \left(\frac{z_R}{z}\right)^2\right] \,, \tag{B.4}$$

and ϕ_{Gouy} is the Gouy phase shift

$$\phi_{\mathrm{Gouy}} = \arctan\frac{z}{z_R} \,, \tag{B.5}$$

entirely due to diffraction effects, where

$$z_R = \frac{\pi w_0^2}{\lambda} \tag{B.6}$$

is the Rayleigh length, that is the length at which the beam size is $\sqrt{2}$ times w_0, the beam size at the waist, and λ is the wavelength.
The Gouy phase indicates that as a Gaussian beam passes through a focus, it acquires

an additional phase shift of π, in addition to the usual $k_0 z$ phase shift that would be expected from a plane wave.

This expression can be obtained either via the Fresnel-Kirchoff integral (c.f [20]) or via the paraxial wave equation (cf.[21]). Considering the second approach, the focus will be pointed on the approximations behind the paraxial wave equation.

The starting point is the electric field wave equation in vacuum

$$\Box E(x, y, z, t) = 0 \,, \tag{B.7}$$

where $\Box$ is the D'Alembert operator

$$\Box := \partial_\alpha \partial^\alpha = \nabla^2 - \frac{1}{c^2}\frac{\partial^2}{\partial t^2} \,. \tag{B.8}$$

Assuming a $e^{-i\omega t}$ time dependence, Eq. (B.7) becomes the Helmholtz equation

$$(\nabla^2 + k_0^2) E(x, y, z) = 0 \,, \tag{B.9}$$

where $k_0 = \omega/c = 2\pi/\lambda$ is the modulus of the vacuum wave vector for a plane wave of angular frequency ω, c being the speed of light. To take into account the paraxial behavior of the wave, that is the concentration of the wave energy around a little cylinder around the axis of propagation, the following ansatz is made:

$$E(x, y, z) = u(x, y, z) e^{ik_0 z} \,, \tag{B.10}$$

where $u(x, y, z)$ is a function slowly varying in the direction of propagation z (on the scale L_d of diffraction effects) and varying in the transversal direction on the waist size w_0 scale length. More precisely we have

$$\begin{aligned} &\left| e^{-ik_0 z} \frac{\partial}{\partial z} e^{ik_0 z} \right|^{-1} = k_0^{-1} \sim \lambda \,, \\ &\left| \frac{1}{u}\frac{\partial u}{\partial x} \right|^{-1} \sim \left| \frac{1}{u}\frac{\partial u}{\partial y} \right|^{-1} \sim w_0 \,, \\ &\left| \frac{1}{u}\frac{\partial u}{\partial z} \right|^{-1} \sim L_d \,. \end{aligned} \tag{B.11}$$

We assume that w_0 is an intermediate scale between λ and L_d:

$$\begin{aligned} &\lambda \ll w_0 \ll L_d \\ &\frac{\lambda}{w_0} \sim \frac{w_o}{L} \sim \kappa^{-1/2} \,, \end{aligned} \tag{B.12}$$

with $\kappa \equiv L/\lambda \gg 1$. Substituting ansatz (B.10) into Eq. (B.9) and introducing

$$\bar{x} = \frac{x}{w_0} \;\;,\;\; \bar{y} = \frac{y}{w_0} \;\;,\;\; \bar{z} = \frac{z}{L_d} \,, \tag{B.13}$$

we obtain the following equation

$$\underbrace{\frac{\partial^2 u}{\partial \bar{x}^2} + \frac{\partial^2 u}{\partial \bar{y}^2}}_{\alpha} + \underbrace{4\pi i \frac{w_0}{\lambda}\frac{w_0}{L_d}\frac{\partial u}{\partial \bar{z}}}_{\beta} + \underbrace{\frac{w_0^2}{L_d^2}\frac{\partial^2 u}{\partial \bar{z}^2}}_{\gamma} = 0 \,, \tag{B.14}$$

where

$$\begin{aligned} &\alpha \sim \beta = O(1) \,, \\ &\gamma = O(\kappa^{-1}) \ll 1 \,. \end{aligned} \tag{B.15}$$

As a consequence the third term γ can be neglected compared to the other two terms. The result, restoring the dimensional quantities, is the well known parabolic wave equation

$$\nabla_\perp^2 u + 2ik_0 \frac{\partial u}{\partial z} = 0 \,, \tag{B.16}$$

which leads to the Gaussian beam solution.

The ordering $\lambda \ll w_0 \ll L_d$ is formally the same as QO approximation (in which the diffraction scale length L_d is supposed of the order of the background plasma length scale L). It is expected that a EC Gaussian beam during the plasma propagation remains nearly Gaussian, and its propagation is usually described within the QO approximation by means of the CGO asymptotic method.

APPENDIX C

Maslov-Pereverzev estimates derivation

The wave field (1.31), in the limit $\kappa \to +\infty$, collapses on the zero-level set of the function $\mathrm{Im}\psi = \phi$, namely,

$$\mathcal{R} = \{x;\ \phi(x) = 0\}. \tag{C.1}$$

This feature is a consequence of the fact that $\phi(x) > 0$ for all points that do not lie on $\mathcal{R}$. In fact, the wave field is exponentially small, in the limit $\kappa \to +\infty$ near points x where $\phi(x) > 0$; indeed, one has $|E_{\mathrm{CGO}}(\kappa, x)| \propto e^{-\kappa\phi(x)} \to 0$ for $\kappa \to +\infty$, or, more precisely, for every integer $n > 0$,

$$\kappa^n |E_{\mathrm{CGO}}(\kappa, x)| \leq C_0 \Big(\frac{n}{e\phi(x)}\Big)^n, \quad \phi(x) > 0, \tag{C.2}$$

which is tantamount to exponential decay. Equation (C.2) follows from (1.6) and from the fact that the single variable function $f(y) = y^n \exp(-y)$ has a global maximum at $y_{\max} = n$, with $f(y_{\max}) = (n/e)^n$. In fact, if we put $y = \kappa\phi$, it follows that

$$\kappa^N e^{-\kappa\phi} = \phi^{-N} y^N e^{-y} \leq \frac{1}{\phi^N} \left(\frac{N}{e}\right)^N. \tag{C.3}$$

Let the set $\mathcal{R}$ be a curve given parametrically by $x = \bar{x}(\tau)$, the "reference ray".

By definition $\phi\big(\bar{x}(\tau)\big) = 0$, identically in τ and

$$0 = \frac{d}{d\tau}\phi\big(\bar{x}(\tau)\big) = \frac{d\bar{x}(\tau)}{d\tau} \cdot \nabla\phi\big(\bar{x}(\tau)\big),$$

which means that the component of $\nabla\phi\big(\bar{x}(\tau)\big)$ tangent to the curve $\mathcal{R}$ vanishes identically; the other two components must vanish as well, otherwise ϕ would change sign across $\mathcal{R}$, thus, violating the condition $\phi \geq 0$. It follows that

$$\nabla\phi\big(\bar{x}(\tau)\big) = 0,$$

identically in τ. Then, the Taylor polynomial of ϕ around $\bar{x}$ has terms of second order or higher only. Continuing, one has

$$0 = \frac{d}{d\tau}\nabla\phi\big(\bar{x}(\tau)\big) = D^2\phi\big(\bar{x}(\tau)\big)\frac{d\bar{x}(\tau)}{d\tau},$$

where $[D^2\phi(x)]_{ij} = \partial^2\phi(x)/\partial x^i \partial x^j$ is the Hessian matrix of second-order derivatives of ϕ. Thence, the tangent vector $e_t(\tau) \propto d\bar{x}(\tau)/d\tau$ is an eigenvector of $D^2\phi\big(\bar{x}(\tau)\big)$ corresponding to the null eigenvalue. In general, the whole matrix $D^2\phi(\bar{x})$ can be zero, and,

in that case, Taylor polynomial of ϕ would have only terms of fourth order or higher (the third order is again excluded by the condition $\phi \geq 0$). For definiteness, we shall consider the case in which, except for the tangent direction $\propto e_t$, the matrix $D^2\phi(\bar{x})$ is strictly positive definite. Precisely,

$$w \cdot D^2\phi\big(\bar{x}(\tau)\big)w > 0, \tag{C.4}$$

for every vector w linearly independent of $e_t(\tau)$, i.e., $D^2\phi$ is positive definite for vectors transversal to the reference curve $\mathcal{R}$. The exact Taylor expansion of a function f around $\bar{x}$ that involves partial derivatives up to the $l+1$ order is given by the following expression:

$$f(x) = \sum_{|\alpha|\leq l} \frac{D^\alpha f(\bar{x})}{\alpha!}(x-\bar{x})^\alpha + \sum_{|\alpha|=l+1} R_\alpha(x)(x-\bar{x})^\alpha \,, \tag{C.5}$$

where

$$R_\alpha(x) = \frac{|\alpha|}{\alpha!}\int_0^1 (1-s)^{|\alpha|-1} D^\alpha f\big(\bar{x}+s(x-\bar{x})\big)ds \,, \tag{C.6}$$

and the multi-index notation has been used ($\alpha = (\alpha_1, \alpha_2, \alpha_3)$ being a three-dimensional multi-index) :

$$\begin{aligned} &|\alpha| = \alpha_1 + \alpha_2 + \alpha_3 \\ &\alpha! = \alpha_1!\alpha_2!\alpha_3! \\ &x^\alpha = x_1^{\alpha_1} x_2^{\alpha_2} x_3^{\alpha_3} \\ &D^\alpha f = \frac{\partial^{|\alpha|} f}{\partial x_1^{\alpha_1}\partial x_2^{\alpha_2}\partial x_3^{\alpha_3}} \,. \end{aligned} \tag{C.7}$$

If we put $l = 1$ in this expression and drop the multi-index notation in favour of the matrix notation, it becomes

$$f(x) = f(\bar{x}) + \nabla f(\bar{x}) \cdot (x-\bar{x}) + (x-\bar{x}) \cdot R(x,\bar{x})(x-\bar{x}), \tag{C.8}$$

with

$$R(x,\bar{x}) = \int_0^1 (1-s) D^2 f\big(\bar{x}+s(x-\bar{x})\big)ds \,. \tag{C.9}$$

As a consequence, recalling that $\phi(\bar{x}) = 0$ and $\nabla\phi(\bar{x}) = 0$, the exact Taylor expansion of ϕ around $\bar{x}$ involving partial derivatives up to the second order is:

$$\phi(x) = \frac{1}{2}(x-\bar{x}) \cdot Q(x,\bar{x})(x-\bar{x}),$$

where, for $|x-\bar{x}|$ small enough, the matrix-valued function,

$$Q(x,\bar{x}) = 2\int_0^1 (1-s) D^2\phi\big(\bar{x}+s(x-\bar{x})\big)ds \,,$$

is positive definite for vectors transversal to the reference curve $\mathcal{R}$. Now it will be proven that for every x sufficiently close to the reference ray $\mathcal{R}$, there exist a point $\bar{x}$ on $\mathcal{R}$ and a 3×3 matrix $B(x,\bar{x})$, such that

$$(x-\bar{x}) \cdot Q(x,\bar{x})(x-\bar{x}) = (x-\bar{x}) \cdot {}^tB(x,\bar{x})B(x,\bar{x})(x-\bar{x}) \,. \tag{C.10}$$

The demonstration of this proposition is shown in three steps. First of all the matrix Q is diagonalized, then the point $\bar{x}$ is found and finally the matrix B is constructed.

Q can be easily diagonalized recalling that it is symmetric by definition. Hence for every pair of points $(x, \bar{x})$, there is a real eigenvector basis $\{v(x,\bar{x}), w_1(x,\bar{x}), w_2(x,\bar{x})\}$ corresponding to real eigenvalues $\{q_0(x,\bar{x}), q_1(x,\bar{x}), q_2(x,\bar{x})\}$ such that

$$Q = q_0 v^t v + q_1 {w_1}^t w_1 + q_2 {w_2}^t w_2 \,, \tag{C.11}$$

where, exploiting the fact that $Q = D^2\phi$ for $x = \bar{x}$, the eigenvectors are ordered so that q_0 tends to zero for $x \to \bar{x}$ and v tends to a vector proportional to the tangent vector $d\bar{x}/d\tau$ to the reference ray . The remaining eigenvectors $\{w_i \,,\ i = 1, 2\}$ are transversal to $\mathcal{R}$ in the limit $x \to \bar{x}$, and from (C.4) it follows that $q_i > 0$ for $i \neq 0$ and x in a sufficiently small tube around $\mathcal{R}$.

The point $\bar{x}$ is found as a solution of the equation

$$v\big(x, \bar{x}(\tau)\big) \cdot \big(x - \bar{x}(\tau)\big) = 0 \,. \tag{C.12}$$

For x close to the reference ray, v tend to the tangent vector and this express the condition that $x - \bar{x}$ is orthogonal to the reference ray.

Now it is possible to construct the matrix B. We restrict to a neighborhood of $\mathcal{R}$ where a solution of the equation (C.12) can be found and $q_0 \sim 0$. Let $\bar{x} = \bar{x}\big(\tau(x)\big)$ be such solution. If needed, we restrict further, so that $q_i(x,\bar{x}) > 0$ for $i \neq 0$. Then, we have:

$$\begin{aligned}
(x - \bar{x}) \cdot Q(x,\bar{x})(x - \bar{x}) &= \sum_{i=1}^{2} \left[(x - \bar{x}) \cdot w_i\right] q_i \left[{}^t w_i (x - \bar{x})\right] \\
&= \sum_{i,j=1}^{2} (x - \bar{x}) \cdot \left[w_i \sqrt{q_i}\right] \delta_{ij} \left[\sqrt{q_j}^t w_j\right] (x - \bar{x}) \\
&= (x - \bar{x}) \cdot \left[\sum_{i=1}^{2} \sqrt{q_i} {w_i}^t w_i\right] \left[\sum_{j=1}^{2} \sqrt{q_j} {w_j}^t w_j\right] (x - \bar{x}) \,,
\end{aligned} \tag{C.13}$$

where the orthogonality $w_i \cdot w_j = {}^t w_i w_j = \delta_{ij}$ has been accounted for. It follows that the 3×3 symmetric matrix

$$B(x,\bar{x}) = \sqrt{q_1(x,\bar{x})} w_1(x,\bar{x})^t w_1(x,\bar{x}) + \sqrt{q_2(x,\bar{x})} w_2(x,\bar{x})^t w_2(x,\bar{x}) \,, \tag{C.14}$$

satisfies (C.10).

Now that (C.10) has been demonstrated, defining the vector valued function

$$\xi(x) = B(x,\bar{x})(x - \bar{x}) \,, \tag{C.15}$$

the imaginary part of the complex phase becomes

$$\phi(x) = \frac{1}{2}\xi(x)^2 = \frac{1}{2}\delta_{ij}\xi^i(x)\xi^j(x) \,. \tag{C.16}$$

This form of the imaginary part ϕ is valid in a neighborhood U of the reference ray $\mathcal{R}$ only, but it is useful to obtain the following inequality:

$$|\xi(x)^\alpha e^{i\kappa\psi(x)}| \leq C_\alpha \kappa^{-|\alpha|/2} \,, \tag{C.17}$$

where α is a three dimensional multi-index. This inequality can be easily proven by noting that, introducing the vector function $z(x) = (z^1(x), z^2(x), z^3(x)) = \sqrt{\kappa}\xi(x)$, it follows that in the U space region

$$\begin{aligned} |\xi(x)^\alpha e^{i\kappa\psi(x)}| &= |\xi^\alpha e^{-\kappa\phi}| = |\xi^\alpha e^{-\kappa\xi^2/2}| = |z^\alpha e^{-z^2/2}|\kappa^{-|\alpha|/2} \\ &\leq \left[|(z^1)^{\alpha_1} e^{-(z^1)^2/2}| + |(z^2)^{\alpha_2} e^{-(z^2)^2/2}| + |(z^3)^{\alpha_3} e^{-(z^3)^2/2}|\right] \kappa^{-|\alpha|/2} \,. \end{aligned} \tag{C.18}$$

The terms in square brackets are bounded in all space, because the single variable function $f(x) = x^n \exp(-x^2/2)$ has a global maximum at $x_{\max} = \sqrt{n}$ with $f(x_{\max}) = (n/e)^{n/2}$, that depends on n. As a consequence, (C.17) is verified.

Equation (C.17), valid in a U neighborhood of the reference ray, can be used to obtain the following inequalities (Maslov-Pereverzev estimates, Eq. (1.47)), valid in every compact region K where the electric field has to be reconstructed, assuming that $\phi(x) \in C^\infty(K)$:

$$|(\nabla\phi(x))^\alpha e^{i\kappa\psi(x)}| \leq C_\alpha \kappa^{-|\alpha|/2} \,. \tag{C.19}$$

For brevity I will now show the proof of this inequalities for the case $\alpha = (1, 0, 0)$:

$$|\partial_1\phi(x) e^{i\kappa\psi(x)}| \leq C\kappa^{-1/2} \,, \tag{C.20}$$

where $\partial_1 \equiv \partial/\partial x^1$. The proof is analogous for an arbitrary multi-index.
In the U neighborhood of the reference ray the (C.17) inequality can be exploited, combined to the fact that in that region the gradient of ϕ can be written

$$\nabla\phi(x) = \delta_{ij}\xi^i(x)\nabla\xi^j(x) \,, \tag{C.21}$$

while in $K \setminus U$ the only inequality that can be exploited is Eq. (C.2). To combine the two regimes, let us introduce the characteristic function $\chi(x)$ defined by

$$\chi(x) = \begin{cases} 1 & \text{if } x \in U \cap K \,, \\ 0 & \text{if } x \notin K \setminus U \,. \end{cases}$$

Henceforth we consider $x \in K$. Now it can be shown that

$$|\chi(x)\partial_1\phi(x) e^{i\kappa\psi(x)}| \leq C_1\kappa^{-1/2} \,, \tag{C.22}$$

$$|(1-\chi(x))\partial_1\phi(x) e^{i\kappa\psi(x)}| \leq C_2\kappa^{-1} \tag{C.23}$$

Let us start by proving Eq. (C.22). In the $U \cap K$ region it can be written

$$|\chi(x)\partial_1\phi(x) e^{i\kappa\psi(x)}| = \left|\delta_{ij}\xi^i\partial_1\xi^j e^{i\kappa\psi}\right| \leq \delta_{ij}|\partial_1\xi^i| \left|\xi^j e^{i\kappa\psi}\right| \,. \tag{C.24}$$

Eq. (C.22) is a consequence of the fact that $|\partial_1\xi^i|$ are bounded $\forall i = 1, 2, 3$, because they are continuous functions on a compact domain (consequence of the $\phi(x) \in C^\infty(K)$ hypothesis), and $\left|\xi^j e^{i\kappa\psi}\right|$ terms can be estimated using Eq. (C.17) with $\alpha = (1, 0, 0)$.
Let us now proof Eq. (C.23). In the $K \setminus U$ region it can be written

$$|(1-\chi(x))\partial_1\phi(x) e^{i\kappa\psi(x)}| = |\partial_1\phi|(\kappa^N e^{-\kappa\phi})\kappa^{-N} \,, \tag{C.25}$$

for all integers N, and in particular if we put $N = 1$. Eq. (C.23) follows from the fact that $|\partial_1\phi|$ is bounded, being a continuous function on a compact domain, and the $(\kappa e^{-\kappa\phi})$ factor can be estimated using Eq. (C.3) with $N = 1$, noting that ϕ has a lower bound on $K \setminus U$. The C_2 constant can be computed as the product of the maximum of $|\partial_1\phi|$ times the Eq. (C.3) upper bound with $\phi = \phi_{\min}$ and $N = 1$, that is

$$C_2 = \frac{1}{e}\frac{\max_{K\setminus U}(|\partial_1\phi|)}{\min_{K\setminus U}(\phi)} \,. \tag{C.26}$$

Combining Eq. (C.22) and (C.23), it follows that

$$|\partial_1\phi(x)e^{i\kappa\psi(x)}| \leq C_1\kappa^{-1/2} + C_2\kappa^{-1} = O(\kappa^{-1/2}) \,, \tag{C.27}$$

and so Eq. (C.20) is proven.

APPENDIX D

CGO energy flux derivation

D.1 Complex geometrical optics equations and their solution

D.1.1 Wave equation ordering

The electric field ansatz (1.30) can be substituted into Maxwell's wave Eq. (1.1), and the result is

$$
\begin{aligned}
e^{i\kappa\psi}\Big\{ & \kappa^2 D_0(x,\nabla\psi)a_0(x) \\
& + \kappa\Big[D_0(x,\nabla\psi)a_1(x) - i\Big[\frac{\partial D_0}{\partial N_i}(x,\nabla\psi)\frac{\partial a_0}{\partial x^i}(x) \\
& + \frac{1}{2}\frac{\partial}{\partial x^i}\Big[\frac{\partial D_0}{\partial N_i}(x,\nabla\psi)\Big]a_0(x) - i\varepsilon_1(x)a_0(x)\Big]\Big]\Big\} + O(1) = 0,
\end{aligned}
\tag{D.1}
$$

where Eq. (1.7) has been accounted for. In writing Eq. (D.1), one should note that the dispersion tensor D_0, defined in Eq. (1.9), is a polynomial in N and it extends to an entire function of the complex refractive index $\tilde{N} = N + iN^{'}$. It is possible, therefore, to evaluate D_0 at $\tilde{N} = \nabla\psi$. The same argument applies to the derivatives of D_0. Explicitly,

$$
D_{0,ij}(x,\nabla\psi) = (\nabla\psi)^2\delta_{ij} - \frac{\partial\psi}{\partial x^i}\frac{\partial\psi}{\partial x^j} - \varepsilon_{0,ij}(x), \tag{D.2a}
$$

$$
\frac{\partial D_{0,ij}}{\partial N_k}(x,\nabla\psi) = 2\frac{\partial\psi}{\partial x^l}\delta^{lk}\delta_{ij} - \delta_i^k\frac{\partial\psi}{\partial x^j} - \frac{\partial\psi}{\partial x^i}\delta_j^k, \tag{D.2b}
$$

$$
\frac{\partial^2 D_{0,ij}}{\partial N_k\partial N_l}(x,\nabla\psi) = 2\delta^{kl}\delta_{ij} - \delta_i^k\delta_j^l - \delta_i^l\delta_j^k, \tag{D.2c}
$$

while

$$
\frac{\partial}{\partial x^k}\Big[\frac{\partial D_{0,ij}}{\partial N_k}(x,\nabla\psi)\Big] = \frac{\partial^2 D_{0,ij}}{\partial x^k\partial N_k}(x,\nabla\psi) + \frac{\partial^2\psi}{\partial x^k\partial x^l}\frac{\partial^2 D_{0,ij}}{\partial N_k\partial N_l}(x,\nabla\psi)\,. \tag{D.3}
$$

The first term on the right-hand side of (D.3) is actually zero for the dispersion tensor (1.9) and the second-order derivative with respect to N is constant, cf. Eq. (D.2c).

Now it is needed to take into account the paraxial character of the beam, applying the Pereverzev-Maslov estimates (1.47). When one neglects the paraxial character of the wave field, terms of different order in κ are separated in (D.1) , yielding a hierarchy of equations for ψ, a_0, and a_1. Such equations, although formally similar to the corresponding equations of standard geometrical optics, are complicated by the presence of the

imaginary part of the phase. The hierarchy thus obtained, however, is unnecessarily too strong and it can be considerably simplified by taking into account (1.47). Pereverzev-Maslov estimate implies that terms proportional to $\mathrm{Im}(\nabla\psi) = \nabla\phi$ in Eq. (D.1) can be better estimated by half-integer powers of κ.

It follows that

$$\begin{aligned} e^{i\kappa\psi} D_0(x,\nabla\psi) = &\underbrace{e^{i\kappa\psi} D_0(x,\nabla S)}_{O(1)} + \\ &+ \underbrace{ie^{i\kappa\psi}\left[2(\nabla S\cdot\nabla\phi)I - \nabla S\nabla\phi - \nabla\phi\nabla S\right]}_{O(\kappa^{-\frac{1}{2}})} + \\ &+ \underbrace{e^{i\kappa\psi}\left[\nabla\phi\nabla\phi - (\nabla\phi)^2 I\right]}_{O(\kappa^{-1})}, \end{aligned} \tag{D.4}$$

where

$$D_0(x,\nabla S) = (\nabla S)^2 I - \nabla S\nabla S - \epsilon_0(x)\,, \tag{D.5}$$

and similarly

$$e^{i\kappa\psi}\frac{\partial D_{0,ij}}{\partial N_k}(x,\nabla\psi) = \underbrace{e^{i\kappa\psi}\frac{\partial D_{0,ij}}{\partial N_k}(x,\nabla S)}_{O(1)} + O(\kappa^{-\frac{1}{2}})\,. \tag{D.6}$$

Applying this results to (D.1) and recalling that

$$\begin{aligned} &\frac{\partial^2 D_{0,ij}}{\partial x^k \partial N_k}(x,\nabla\psi) = 0\,, \\ &\frac{\partial^2 D_{0,ij}}{\partial N_k \partial N_l}(x,\nabla\psi) = \mathrm{const}\,, \end{aligned} \tag{D.7}$$

we obtain

$$\begin{aligned} e^{i\kappa\psi}\Big\{ &\kappa^2 D_0(x,\nabla\psi)a_0(x) \\ &+ \kappa\Big[D_0(x,\nabla S)a_1(x) - i\Big[\frac{\partial D_0}{\partial N_i}(x,\nabla S)\frac{\partial a_0}{\partial x^i}(x) \\ &+ \frac{1}{2}\frac{\partial^2\psi}{\partial x^i\partial x^j}(x)\frac{\partial^2 D_0}{\partial N_i\partial N_j}(x,\nabla S)a_0(x) - i\varepsilon_1(x)a_0(x)\Big]\Big]\Big\} + O(\sqrt{\kappa}) = 0. \end{aligned} \tag{D.8}$$

Since (D.8) has to be valid $\forall\kappa$ sufficiently large, the independence of the powers κ^n is now exploited to separate the coefficients of κ^2 and κ:

$$D_0(x,\nabla\psi)a_0(x) = \rho_0(x,\nabla\phi)\,, \tag{D.9}$$

$$\begin{aligned} &D_0(x,\nabla S)a_1(x) - i\left[\frac{\partial D_0}{\partial N_i}(x,\nabla S)\frac{\partial a_0}{\partial x^i}(x)\right. \\ &\left. + \frac{1}{2}\frac{\partial^2\psi}{\partial x^i\partial x^j}(x)\frac{\partial^2 D_0}{\partial N_i\partial N_j}(x,\nabla S)a_0(x) - i\varepsilon_1(x)a_0(x)\right] = \rho_1(x,\nabla\phi)\,, \end{aligned} \tag{D.10}$$

where ρ_0 and ρ_1 are allowed remainders in order to solve eq. $(D.8)$ with the correct $O(\sqrt{\kappa})$ remainder. ρ_0 and ρ_1 must be at least cubic and linear in $\nabla\phi$, respectively, so that at least:

$$\begin{aligned} e^{-\kappa\phi}\rho_0(x,\nabla\phi) &= O(\kappa^{-3/2}) \,, \\ e^{-\kappa\phi}\rho_1(x,\nabla\phi) &= O(\kappa^{-1/2}) \,. \end{aligned} \tag{D.11}$$

D.1.2 Solution of the wave equation at the dominant order

The matrix $D_0(x,\tilde{N})$, for $\tilde{N} = N + iN^{'}$ complex, is no longer Hermitian, even though it is Hermitian for $N^{'} = 0$. To solve eq. (D.9) we can exploit the fact that the matrix $D_0(x,\nabla\psi)$, even if it is no longer Hermitian, is still much simpler than a generic complex matrix, being the analytical continuation of a Hermitian matrix. To exploit the properties of the Hermitian matrix $D_0(x,N)$ we rewrite $D_0(x,\tilde{N})$ in the following way:

$$D_0(x,\tilde{N}) = \tilde{D}_0(x,\tilde{N}) \,, \tag{D.12}$$

where

$$\tilde{D}_0(x,\tilde{N}) = D_0(x,N) + i\frac{\partial D_0(x,N)}{\partial N_k}N_k^{'} - \frac{1}{2}\frac{\partial^2 D_0(x,N)}{\partial N_k \partial N_l}N_k^{'}N_l^{'} \,. \tag{D.13}$$

The equality (D.12) can be easily checked taking into account that from (D.2) it follows that

$$\begin{aligned} \frac{\partial D_0}{\partial N_k}N_k^{'} &= 2(N\cdot N^{'})I - N^{'}N - NN^{'} \,, \\ \frac{\partial D_0}{\partial N_k \partial N_l}N_k^{'}N_l^{'} &= 2N^{'2}I - N^{'}N^{'} \,. \end{aligned} \tag{D.14}$$

The key point of the solution of the wave equation at the dominant order is the fact that if $e_j(x,N)$ and $\lambda_j(x,N)$ are the $j-$th eigenvector and relative eigenvalue of $D_0(x,N)$ that solve the eigenvalue equation

$$D_0(x,N)e_j(x,N) = \lambda_j(x,N)e_j(x,N) \,, \tag{D.15}$$

the analytic continuations $\tilde{e}_j(x,\tilde{N})$ and $\tilde{\lambda}_j(x,\tilde{N})$ still solve the equation, apart from a remainder cubic in $|N^{'}|$, that is

$$\Gamma \equiv D_0(x,\tilde{N})\tilde{e}_j(x,\tilde{N}) - \tilde{\lambda}_j(x,\tilde{N})\tilde{e}_j(x,\tilde{N}) = O(|N'|^3) \,, \tag{D.16}$$

where

$$\tilde{e}_j(x,\tilde{N}) = e_j(x,N) + i\frac{\partial e_j(x,N)}{\partial N_k}N_k' - \frac{1}{2}\frac{\partial^2 e_j(x,N)}{\partial N_k \partial N_l}N_k'N_l' \,, \tag{D.17}$$

$$\tilde{\lambda}_j(x,\tilde{N}) = \lambda_j(x,N) + i\frac{\partial \lambda_j(x,N)}{\partial N_k}N_k' - \frac{1}{2}\frac{\partial^2 \lambda_j(x,N)}{\partial N_k \partial N_l}N_k'N_l' \,. \tag{D.18}$$

In fact, substituting (D.13), (D.17) and (D.18) in the Γ expression, we obtain

$$\begin{aligned}\Gamma &= D_0 e_j - \lambda_j e_j \\ &+ i\left[\frac{\partial D_0}{\partial N_k}e_j + D_0\frac{\partial e_j}{\partial N_k} - \frac{\partial \lambda_j}{\partial N_k}e_j - \lambda_j\frac{\partial e_j}{\partial N_k}\right]N_k^{'} \\ &- \frac{1}{2}\left[\frac{\partial^2 D_0}{\partial N_k \partial N_l}e_j + \frac{\partial D_0}{\partial N_k}\frac{\partial e_j}{\partial N_l} + \frac{\partial D_0}{\partial N_l}\frac{\partial e_j}{\partial N_k} + D_0\frac{\partial^2 e_j}{\partial N_k \partial N_l}\right. \\ &\left. - \frac{\partial^2 \lambda_j}{\partial N_k \partial N_l}e_j - \frac{\partial \lambda_j}{\partial N_k}\frac{\partial e_j}{\partial N_l} - \frac{\partial \lambda_j}{\partial N_l}\frac{\partial e_j}{\partial N_k} - \lambda_j\frac{\partial^2 e_j}{\partial N_k \partial N_l}\right]N_k^{'}N_l^{'} \\ &- \frac{i}{2}\left[\frac{\partial^2 D_0}{\partial N_k \partial N_m}\frac{\partial e_j}{\partial N_l} + \frac{\partial D_0}{\partial N_k}\frac{\partial^2 e_j}{\partial N_l \partial N_m} - \frac{\partial^2 \lambda_j}{\partial N_k \partial N_m}\frac{\partial e_j}{\partial N_l} - \frac{\partial \lambda_j}{\partial N_k}\frac{\partial^2 e_j}{\partial N_l \partial N_m}\right]N_k^{'}N_l^{'}N_m^{'} \\ &+ \frac{1}{4}\left[\frac{\partial^2 D_0}{\partial N_k \partial N_m}\frac{\partial^2 e_j}{\partial N_l \partial N_n} - \frac{\partial^2 \lambda_j}{\partial N_k \partial N_m}\frac{\partial^2 e_j}{\partial N_l \partial N_n}\right]N_k^{'}N_l^{'}N_m^{'}N_n^{'} \\ &= (D_0 e_j - \lambda_j e_j) + i\frac{\partial (D_0 e_j - \lambda_j e_j)}{\partial N_k}N_k^{'} - \frac{1}{2}\frac{\partial^2 (D_0 e_j - \lambda_j e_j)}{\partial N_k \partial N_l}N_k^{'}N_l^{'} + O(|N^{'}|^3)\,.\end{aligned} \tag{D.19}$$

where the symmetry of $N_i^{'}N_j^{'}$ was exploited to write

$$\frac{\partial A}{\partial N_i}\frac{\partial B}{\partial N_j}N_i^{'}N_j^{'} = \frac{1}{2}\left[\frac{\partial A}{\partial N_i}\frac{\partial B}{\partial N_j} + \frac{\partial A}{\partial N_j}\frac{\partial B}{\partial N_i}\right]N_i^{'}N_j^{'}\,, \tag{D.20}$$

with $B = e_j$ and $A = D_0$ or $A = \lambda_j$. Equation (D.16) follows from (D.15).
Moreover, similarly it can be shown that the completeness and orthogonality conditions for the $D_0(x, N)$ eigenvectors

$$I = \sum_j e_j(x, N)e_j^*(x, N)\,, \tag{D.21}$$

$$e_i^*(x, N) \cdot e_j(x, N) = \delta_{ij}\,, \tag{D.22}$$

are still valid for $\tilde{D}_0(x, \tilde{N})$ "eigenvectors", apart from a cubic remainder:

$$I - \sum_j \tilde{e}_j(x, \tilde{N})\tilde{f}_j(x, \tilde{N}) = O(|N'|^3)\,, \tag{D.23}$$

$$\tilde{f}_i(x, \tilde{N}) \cdot \tilde{e}_j(x, \tilde{N}) - \delta_{ij} = O(|N'|^3)\,, \tag{D.24}$$

where $\tilde{f}_j(x, \tilde{N})$ is the complex extension of the dual eigenvector $e_j^*(x, N)$:

$$\tilde{f}_j(x, \tilde{N}) = e_j^*(x, N) + i\frac{\partial e_j^*(x, N)}{\partial N_k}N_k' - \frac{1}{2}\frac{\partial^2 e_j^*(x, N)}{\partial N_k \partial N_l}N_k'N_l'\,. \tag{D.25}$$

Now it is possible to solve (D.9). First of all (D.23) is exploited to expand the amplitude $a_0(x)$ on the $\tilde{D}_0(x, \tilde{N})$ "eigenvectors":

$$a_0(x) = Ia_0(x) = \sum_j A_j(x)\tilde{e}_j(x, \nabla\psi) + O(|\nabla\phi|^3)\,, \tag{D.26}$$

where

$$A_j(x) = \tilde{f}_j(x, \nabla\psi) \cdot a_0(x)\,. \tag{D.27}$$

After substituting (D.26) and using (D.12) and (D.16), eq. (D.9) amounts to

$$\sum_j \tilde{\lambda}_j(x,\nabla\psi)A_j(x)\tilde{e}_j(x,\nabla\psi) + O(|\nabla\phi|^3) = \rho_0(x,\nabla\phi)\ . \tag{D.28}$$

Taking the dot product with $\tilde{f}_i$ and using the orthogonality (D.24), the vector equation (D.28) is splitted into three scalar equations:

$$\tilde{\lambda}_i(x,\nabla\psi)A_i(x) + O(|\nabla\phi|^3) = \tilde{f}_i(x,\nabla\psi)\cdot\rho_0(x,\nabla\phi)\ . \tag{D.29}$$

for $i = 1,2,3$. Apart from the trivial solution $A_i = 0\ ,\ \forall i = 1,2,3$, the equation is fulfilled if and only if

$$\tilde{\lambda}_i(x,\nabla\psi) = O(|\nabla\phi|^3)\ , \tag{D.30}$$

because $A_i = O(1)$, $\tilde{f}_i(x,\nabla\psi) = O(1)$ and $\rho_0(x,\nabla\phi)$ is at least cubic in $\nabla\phi$. On the other hand, only one out of the three eigenvalues can fulfill this condition for a given complex phase ψ, otherwise the hypothesis of separability of eigenvalues λ_i would be violated in points $(x,\nabla S(x))$, for $x = x(\tau)$ on the reference ray.

Summing up, given a mode relative to the $D_0(x,\nabla S)$ eigenvalue $H(x,\nabla S)$ (and relative eigenvector $e(x,\nabla S)$), eq. (D.9) is solved by a complex eikonal $\psi(x)$ and an amplitude $a_0(x)$ such that

$$\tilde{H}(x,\nabla\psi) = \sigma_0(x,\nabla\phi)\ , \tag{D.31}$$

$$a_0(x) = A(x)\tilde{e}(x,\nabla\psi)\ , \tag{D.32}$$

where $\sigma_0(x,\nabla\phi)$ is an arbitrary cubic remainder and $A(x)$ is an arbitrary complex scalar amplitude.

Eq. (D.31) depends on the arbitrary cubic remainder σ_0, and therefore it does not determine uniquely the complex eikonal ψ. The natural choice $\sigma_0 = 0$ leads to the following set of equations:

$$\mathrm{Re}(\tilde{H})(x,\nabla S) \equiv H_\phi(x,\nabla S) = H(x,\nabla S) - \frac{1}{2}\frac{\partial^2 H(x,\nabla S)}{\partial N_k \partial N_l}\frac{\partial\phi}{\partial x^k}\frac{\partial\phi}{\partial x^l} = 0\ , \tag{D.33}$$

$$\mathrm{Im}(\tilde{H})(x,\nabla S) = \frac{\partial H(x,\nabla S)}{\partial N_k}\frac{\partial\phi}{\partial x^k} = 0\ . \tag{D.34}$$

D.1.3 Solution of the first order wave equation: amplitude transport

If (D.32) is substituted into (D.10) and the obtained equation is dot multiplied with $\tilde{f}(x,\nabla\psi)$, the result is

$$\underbrace{\tilde{f}\cdot D_0 a_1}_{\alpha} - \underbrace{i\tilde{f}\cdot\left[\overbrace{\frac{\partial D_0}{\partial N_i}\frac{\partial[A\tilde{e}]}{\partial x^i}}^{\beta_1} + \overbrace{\frac{1}{2}\frac{\partial^2\psi}{\partial x^i\partial x^j}\frac{\partial^2 D_0}{\partial N_i\partial N_j}[A\tilde{e}]}^{\beta_2}\overbrace{-i\varepsilon_1[A\tilde{e}]}^{\beta_3}\right]}_{\beta} = \underbrace{\tilde{f}\cdot\rho_1}_{O(|\nabla\phi|)}\ , \tag{D.35}$$

where $\tilde{f}$ and $\tilde{e}$ are evaluated at $(x,\nabla\psi)$, A, a_1 and ε_1 at x, D_0 and its N derivatives at $(x,\nabla S)$ while ρ_1 is evaluated at $(x,\nabla\phi)$. The notation $\partial[\cdots]/\partial x^k$ denotes the derivative

with respect to both the explicit and implicit dependence on x.

We will manipulate α and β terms separately. Let us start with α. From (D.12) and (D.13) it follows that

$$\begin{aligned} D_0(x,\nabla S) &= D_0(x,\nabla\psi) - \underbrace{i\frac{\partial D_0(x,\nabla S)}{\partial N_k}\frac{\partial\phi}{\partial x^k}}_{O(|\nabla\phi|)} + \underbrace{\frac{1}{2}\frac{\partial^2 D_0(x,\nabla S)}{\partial N_k \partial N_l}\frac{\partial\phi}{\partial x^k}\frac{\partial\phi}{\partial x^l}}_{O(|\nabla\phi|^2)} \\ &= D_0(x,\nabla\psi) + O(|\nabla\phi|)\,. \end{aligned} \tag{D.36}$$

As a consequence

$$\alpha \equiv \tilde{f}(x,\nabla\psi)\cdot D_0(x,\nabla S)a_1(x) = \tilde{f}(x,\nabla\psi)\cdot D_0(x,\nabla\psi)a_1(x) + O(|\nabla\phi|) \tag{D.37}$$

Moreover, following (D.16) derivation, it is easy to recover that

$$\tilde{f}(x,\nabla\psi)\cdot D_0(x,\nabla\psi) = \tilde{H}(x,\nabla\psi)\tilde{f}(x,\nabla\psi) + O(|\nabla\phi|^3)\,. \tag{D.38}$$

Summing up it follows that

$$\alpha = \underbrace{\tilde{H}(x,\nabla\psi)}_{O(|\nabla\phi|^3)}\underbrace{\tilde{f}(x,\nabla\psi)\cdot a_1(x)}_{O(1)} + O(|\nabla\phi|) = O(|\nabla\phi|)\,, \tag{D.39}$$

where (D.31) was exploited in the last equivalence, with $\sigma_0 = O(|\nabla\phi|^3)$.

Let us consider the β term. It must be dealt with carefully. First of all we retain only terms of zero order in $\nabla\phi$, because the allowed remainder ρ_1 is $O(|\nabla\psi|)$:

$$\tilde{f}(x,\nabla\psi)\cdot\Big[\cdots\Big] = [\underbrace{e^*(x,\nabla S)}_{O(1)} + O(|\nabla\phi|)]\cdot\underbrace{\Big[\cdots\Big]}_{O(1)} = e^*(x,\nabla S)\Big[\cdots\Big] + O(|\nabla\phi|)\,. \tag{D.40}$$

The terms β_1, β_2 and β_3 are manipulated separately. We start with β_1. From definition (D.17), one gets

$$\frac{\partial[A\tilde{e}]}{\partial x^k} = \frac{\partial[Ae]}{\partial x^k} + iA\frac{\partial^2\phi}{\partial x^k\partial x^l}\frac{\partial e}{\partial N_l} + O(|\nabla\phi|)\,, \tag{D.41}$$

hence

$$\begin{aligned} \beta_1 &\equiv e^*\cdot\frac{\partial D_0}{\partial N_k}\frac{\partial[A\tilde{e}]}{\partial x^k} = e^*\cdot\frac{\partial D_0}{\partial N_k}\frac{\partial[Ae]}{\partial x^k} + iAe^*\cdot\frac{\partial D_0}{\partial N_k}\frac{\partial e}{\partial N_l}\frac{\partial^2\phi}{\partial x^k\partial x^l} + O(|\nabla\phi|) \\ &= e^*\cdot\frac{\partial D_0}{\partial N_k}\frac{\partial[Ae]}{\partial x^k} + \frac{i}{2}Ae^*\cdot\left(\frac{\partial D_0}{\partial N_k}\frac{\partial e}{\partial N_l} + \frac{\partial D_0}{\partial N_l}\frac{\partial e}{\partial N_k}\right)\frac{\partial^2\phi}{\partial x^k\partial x^l} + O(|\nabla\phi|)\,, \end{aligned} \tag{D.42}$$

where in the last equivalence the symmetry of $\partial\phi/\partial x^k\partial x^l$ was exploited. The term in round brackets can be computed by making use of the identity obtained by deriving twice the eigenvalue equation $D_0 e = He$ with respect to N, evaluating the result for $N = \nabla S$:

$$\begin{aligned} &e^*\cdot\left(\frac{\partial D_0}{\partial N_k}\frac{\partial e}{\partial N_l} + \frac{\partial D_0}{\partial N_l}\frac{\partial e}{\partial N_k}\right) = \frac{\partial^2 H}{\partial N_k\partial N_l} - e^*\cdot\frac{\partial^2 D_0}{\partial N_k\partial N_l}e \\ &+ e^*\cdot\left(\frac{\partial H}{\partial N_k}\frac{\partial e}{\partial N_l} + \frac{\partial H}{\partial N_l}\frac{\partial e}{\partial N_k}\right) + \underbrace{He^*\cdot\frac{\partial^2 e}{\partial N_k\partial N_l} - e^*\cdot D_0\frac{\partial^2 e}{\partial N_k\partial N_l}}_{\zeta}\,. \end{aligned} \tag{D.43}$$

The ζ term vanishes, since because of the hermitianity of D_0 and of the reality of H it follows that

$$[e^* \cdot D_0]_i = e^*_j D_{0,ji} = [D^*_{0,ji} e_j]^* = [D_{0,ij} e_j]^* = [He_i]^* = He^*_i \ . \tag{D.44}$$

After substituting into β_1 and taking into account the symmetry of $\partial\phi/\partial x^i \partial x^j$ due to ϕ smoothness using (D.20) with $A \to H$, $B \to e$ and $N_k N_l \to \partial\phi/\partial x^i \partial x^j$, the following expression is obtained

$$\begin{aligned} \beta_1 = {} & e^* \cdot \frac{\partial D_0}{\partial N_k} \frac{\partial [Ae]}{\partial x^k} \\ & + \frac{i}{2} A \left[\frac{\partial^2 H}{\partial N_k \partial N_l} - e^* \cdot \frac{\partial^2 D_0}{\partial N_k \partial N_l} e \right] \frac{\partial^2 \phi}{\partial x^k \partial x^l} \\ & + iA \frac{\partial H}{\partial N_k} \frac{\partial e}{\partial N_l} \frac{\partial^2 \phi}{\partial x^k \partial x^l} + O(|\nabla\phi|) \ . \end{aligned} \tag{D.45}$$

The last term in β_1 expression can be estimated to be $O(|\nabla\phi|)$. Let us show this. The imaginary part of (D.31) is

$$\frac{\partial H}{\partial N_k} \frac{\partial \phi}{\partial x^k} = \mathrm{Im}(\sigma_0) \ , \tag{D.46}$$

with σ_0 cubic in $\nabla\phi$. Deriving respect to x^l one obtains

$$\underbrace{\frac{\partial H}{\partial N_k} \frac{\partial^2 \phi}{\partial x^l \partial x^k}}_{O(1)} + \underbrace{\frac{\partial^2 H}{\partial x^l \partial N_k} \frac{\partial \phi}{\partial x^k}}_{O(|\nabla\phi|)} = \underbrace{\frac{\partial \big(\mathrm{Im}(\sigma_0)\big)}{\partial x^l}}_{O(|\nabla\phi|^2)} \ , \tag{D.47}$$

because $\partial\big(\mathrm{Im}(\sigma_0)\big)/\partial x^l$ is quadratic in $\nabla\phi$. As a consequence

$$iA \frac{\partial H}{\partial N_k} \frac{\partial e}{\partial N_l} \frac{\partial^2 \phi}{\partial x^k \partial x^l} = O(|\nabla\phi|) \tag{D.48}$$

and

$$\beta_1 = e^* \cdot \frac{\partial D_0}{\partial N_k} \frac{\partial [Ae]}{\partial x^k} + \frac{i}{2} A \frac{\partial^2 \phi}{\partial x^k \partial x^l} \left[\frac{\partial^2 H}{\partial N_k \partial N_l} - e^* \cdot \frac{\partial^2 D_0}{\partial N_k \partial N_l} e \right] + O(|\nabla\phi|) \ . \tag{D.49}$$

Let us now consider β_2 and β_3. They can be written in the following form:

$$\begin{aligned} \beta_2 \equiv {} & e^* \cdot \frac{1}{2} \frac{\partial^2 \psi}{\partial x^i \partial x^j} \frac{\partial^2 D_0}{\partial N_i \partial N_j} [A\tilde{e}] = e^* \cdot \frac{1}{2} \frac{\partial^2 \psi}{\partial x^i \partial x^j} \frac{\partial^2 D_0}{\partial N_i \partial N_j} [Ae] + O(|\nabla\phi|) \\ = {} & \frac{1}{2} A \frac{\partial^2 S}{\partial x^i \partial x^j} e^* \cdot \frac{\partial^2 D_0}{\partial N_i \partial N_j} e + \frac{i}{2} A \frac{\partial^2 \phi}{\partial x^i \partial x^j} e^* \cdot \frac{\partial^2 D_0}{\partial N_i \partial N_j} e + O(|\nabla\phi|) \ , \end{aligned} \tag{D.50}$$

$$\beta_3 \equiv e^* \cdot (-i\varepsilon_1 [A\tilde{e}]) = -iAe^* \cdot \varepsilon_1 e + O(|\nabla\phi|) \ . \tag{D.51}$$

After substituting β_1, β_2 and β_3 into β, the result is

$$\begin{aligned} & \underbrace{e^* \cdot \frac{\partial D_0}{\partial N_k} \frac{\partial [Ae]}{\partial x^k} + e^* \cdot \left[\frac{1}{2} \frac{\partial^2 S}{\partial x^k \partial x^l} \frac{\partial^2 D_0}{\partial N_k \partial N_l} - i\varepsilon_1 \right] eA}_{\text{formally like GO}} \\ & + \underbrace{\frac{i}{2} \frac{\partial^2 \phi}{\partial x^k \partial x^l} \frac{\partial^2 H}{\partial N_k \partial N_l}}_{\text{new CGO term}} + O(|\nabla\phi|) = \tilde{f} \cdot \rho_1 \ . \end{aligned} \tag{D.52}$$

One can find out that the first two terms in Eq. (D.52) are formally the same as those in the corresponding equation of standard geometrical optics, which implies the amplitude transport equation (1.17). The only difference consists in evaluating all phase space functions at $N = \nabla S$, with $\psi = S + i\phi$ solving (D.31). Thus, one has

$$H(x, \nabla S) = O(|\nabla \phi|^2) \,, \tag{D.53}$$

as opposite to the exact local dispersion relation $H(x, \nabla S) = 0$ of the standard geometrical optics. This fact follows from the real part of (D.31):

$$H(x, \nabla S) = \underbrace{\frac{1}{2} \frac{\partial^2 H(x, \nabla S)}{\partial N_k \partial N_l} \frac{\partial \phi}{\partial x^k} \frac{\partial \phi}{\partial x^l}}_{O(|\nabla \phi|^2)} + \underbrace{\sigma_0(x, \nabla \phi)}_{O(|\nabla \phi|^3)} = O(|\nabla \phi|^2) \,. \tag{D.54}$$

With that in mind, we can follow the lines of the standard theory (cf., for instance Littlejohn and Flynn [22]). I will continue exposing all the calculation in detail.

Recalling that $A = A(x)$ and $e = e(x, \nabla S)$, we obtain

$$\begin{aligned} GO - \text{like term} = & \underbrace{e^* \cdot \frac{\partial D_0}{\partial N_k} e}_{\alpha'} \frac{\partial A}{\partial x^k} + e^* \cdot \frac{\partial D_0}{\partial N_k} \frac{\partial e}{\partial x^k} A + e^* \cdot \frac{\partial D_0}{\partial N_k} \frac{\partial e}{\partial N_l} \frac{\partial^2 S}{\partial x^k \partial x^l} A \\ & + \frac{1}{2} \underbrace{e^* \cdot \frac{\partial^2 D_0}{\partial N_k \partial N_l} e}_{\beta'} \frac{\partial^2 S}{\partial x^k \partial x^l} A - i e^* \cdot \epsilon_1 e A \,. \end{aligned} \tag{D.55}$$

$\beta^{'}$ can be expressed in function of $\partial^2 H / \partial N_k \partial N_l$ by (D.43) with $\zeta = 0$ and in a similar way, deriving $D_0 e = H e$ respect to N_k and using $(e^* \cdot D_0 = H e^*)$, it can be shown that

$$\alpha^{'} \equiv e^* \cdot \frac{\partial D_0}{\partial N_k} e = \frac{\partial H}{\partial N_k} \,. \tag{D.56}$$

As a consequence, after exploiting the symmetry of $\partial^2 S / \partial x^k \partial x^l$, it can be found

$$\begin{aligned} GO - \text{like term} = & \frac{\partial H}{\partial N_k} \frac{\partial A}{\partial x^k} + \Bigg[\underbrace{e^* \cdot \frac{\partial D_0}{\partial N_k} \frac{\partial e}{\partial x^k}}_{\alpha''} + \frac{1}{2} \frac{\partial^2 H}{\partial N_k \partial N_l} \frac{\partial^2 S}{\partial x^k \partial x^l} \\ & + \underbrace{e^* \cdot \frac{\partial H}{\partial N_k} \frac{\partial e}{\partial N_l} \frac{\partial^2 S}{\partial x^k \partial x^l}}_{\beta''} - i e^* \cdot \epsilon_1 e \Bigg] A \,. \end{aligned} \tag{D.57}$$

Now we will manipulate $\alpha^{''}$ and $\beta^{''}$ terms. Let us start with $\beta^{''}$. If the total space derivative of (D.33) is taken, from the result the following estimate can be obtained:

$$\frac{\partial H}{\partial x^k} + \frac{\partial^2 S}{\partial x^k \partial x^l} \frac{\partial H}{\partial N_l} = O(|\nabla \psi|) \,. \tag{D.58}$$

In fact

$$
\begin{aligned}
0 = \frac{\partial}{\partial x^n}[H_\phi] = \frac{\partial [H]}{\partial x^n} - \frac{1}{2}\frac{\partial}{\partial x^n}\left[\frac{\partial^2 H}{\partial N_k \partial N_l}\right]\frac{\partial \phi}{\partial x^k}\frac{\partial \phi}{\partial x^l} \\
- \frac{1}{2}\frac{\partial^2 H}{\partial N_k \partial N_l}\frac{\partial^2 \phi}{\partial x^n \partial x^k}\frac{\partial \phi}{\partial x^l} - \frac{1}{2}\frac{\partial^2 H}{\partial N_k \partial N_l}\frac{\partial \phi}{\partial x^k}\frac{\partial^2 \phi}{\partial x^n \partial x^l} \\
= \frac{\partial H}{\partial x^n} + \frac{\partial^2 S}{\partial x^n \partial x^k}\frac{\partial H}{\partial N_k} - \underbrace{\frac{1}{2}\frac{\partial}{\partial x^n}\left[\frac{\partial^2 H}{\partial N_k \partial N_l}\right]\frac{\partial \phi}{\partial x^k}\frac{\partial \phi}{\partial x^l}}_{O(|\nabla\phi|^2)} \\
- \underbrace{\frac{\partial^2 H}{\partial N_k \partial N_l}\frac{\partial^2 \phi}{\partial x^n \partial x^k}\frac{\partial \phi}{\partial x^l}}_{O(|\nabla\phi|)},
\end{aligned}
\tag{D.59}
$$

where in the last equality the symmetry of $\partial^2 H/\partial N_k \partial N_l$ was exploited. From (D.58) it follows that

$$
\beta'' = -e^* \cdot \frac{\partial H}{\partial x^k}\frac{\partial e}{\partial N_k} + O(|\nabla\phi|) \,. \tag{D.60}
$$

Let us consider α''. Using (D.44) and (D.53), it can be rewritten as follows

$$
\alpha'' = e^* \cdot \frac{\partial H}{\partial N_k}\frac{\partial e}{\partial x^k} - \frac{\partial e^*}{\partial N_k} \cdot D_0 \frac{\partial e}{\partial x^k} + O(|\nabla\phi|^2) \,. \tag{D.61}
$$

Moreover, we point out that $-ie^* \cdot \epsilon_1 e = e^* \cdot \epsilon_1^a e$, because $\epsilon_1 = \epsilon_1^h + i\epsilon_1^a$ (with ϵ_1^h andϵ_1^a being its hermitian and anti-hermitian part respectively) and usually the first order hermitian part of the dielectric tensor vanishes. Summing up, the GO-like term becomes

$$
\begin{aligned}
GO - \text{like term} = \frac{\partial H}{\partial N_k}\frac{\partial A}{\partial x^k} + \left[\frac{1}{2}\frac{\partial^2 S}{\partial x^k \partial x^l}\frac{\partial^2 H}{\partial N_k \partial N_l} + e^* \cdot \{H, e\}\right. \\
\left. - \frac{\partial e^*}{\partial N_k} \cdot D_0 \frac{\partial e}{\partial x^k} - ie^* \cdot \epsilon_1 e\right] A + O(|\nabla\phi|) \,,
\end{aligned}
\tag{D.62}
$$

where the poisson brackets are defined in (1.21). This term can be easily put in the more symmetric form (1.17). In fact deriving $D_0 e = He$ respect N and x, after a little of algebra, recalling that $H(x, \nabla S) = O(|\nabla\phi|^2)$ and $\partial^2 D_0/\partial x^k \partial N_k = 0$, it follows that

$$
\begin{aligned}
\frac{1}{2}\frac{\partial^2 S}{\partial x^k \partial x^l}\frac{\partial^2 H}{\partial N_k \partial N_l} = \frac{1}{2}\frac{\partial}{\partial x^k}\left[\frac{\partial H}{\partial N_k}\right] - \frac{1}{2}\frac{\partial^2 H}{\partial x^k \partial N_k} = \\
= \frac{1}{2}\frac{\partial}{\partial x^k}\left[\frac{\partial H}{\partial N_k}\right] + \frac{1}{2}\left(\frac{\partial e^*}{\partial N_k} \cdot D_0 \frac{\partial e}{\partial x^k} + \frac{\partial e^*}{\partial x^k} \cdot D_0 \frac{\partial e}{\partial N_k}\right) + O(|\nabla\phi|^2) \,,
\end{aligned}
\tag{D.63}
$$

which after substitution in (D.62) gives, with a slightly different notation, Eq. (1.17), apart from a remainder at least linear in $\nabla\phi$ and recalling that V(x)=$\partial H/\partial N(x, \nabla S(x))$, where $S(x)$ function is different from the *GO* namesake. Substituting the $GO - \text{like term}$ into (D.52), we obtain the complete amplitude transport equation

$$
V(x) \cdot \nabla A(x) - [-\gamma_1(x) + i(\delta_1(x) - \delta_{\text{Gouy}}(x)) - \frac{1}{2}\nabla \cdot V(x)]A(x) = \sigma_1(x, \nabla\phi) \,, \tag{D.64}
$$

where γ_1 and δ_1 are formally given by (1.19) and (1.20), respectively, and the additional phase shift

$$\delta_{\text{Gouy}} = \frac{1}{2}\frac{\partial^2 H(x,\nabla S)}{\partial N_k \partial N_l}\frac{\partial^2 \phi}{\partial x^k \partial x^l} \,, \tag{D.65}$$

is the generalization of the classical Gouy shift (1.36). Again, an arbitrary remainder $\sigma_1(x,\nabla\phi)$ is allowed, which must be at least linear in $\nabla\phi$.

D.2 Wave energy flux derivation in the standard formulation of CGO

Let us consider the standard formulation of CGO (natural choice $\sigma_0 = \sigma_1 = 0$ of the remainders in Eqs. (1.55) and (1.71)).
The derivation of the energy density flux expression is considerably simplified by the fact that Eq. (1.71) parallels the corresponding GO amplitude transport equation (1.17). The only additional term in the complex geometrical optics transport equation is the purely imaginary Gouy phase shift term, and a phase shift does not affect the transport of $|A|^2$. If Eq. (1.73) is multiplied by A^* and the real part is taken, the result

$$\nabla \cdot [V(x)|A(x)|^2] = -2\gamma_1(x,\nabla S)|A(x)|^2 \tag{D.66}$$

is formally identical to the GO one, obtained from Eq. (1.17). Apart from this formal equality, the interpretation of the CGO and GO result is different. In fact, in CGO, the squared amplitude $|A|^2$ does not account for the whole electric field amplitude as, from (1.30) and (1.56),

$$|E|^2 = e^{-2\kappa\phi}|A(x)|^2 + O(1/\sqrt{\kappa}) \,, \tag{D.67}$$

where the Pereverzev-Maslov estimate (C.19) has been accounted for (the exponential has double argument, so the constant C_α is different but the κ power behavior remains unchanged). Let us now show that the factor $e^{-2\kappa\phi}$ is present also in the energy flux expression.
Let us turn to physical units. The Poynting vector, that represents the energy density flux, is defined [23] by

$$S = \frac{c}{4\pi}\text{Re}E \times \text{Re}B \,, \tag{D.68}$$

where the customary complex expression of E and B was considered and, because we are interested in the time-averaged expression over the period $2\pi/\omega$, we have

$$\langle S\rangle = \frac{c}{8\pi}\text{Re}(E^* \times B) = \frac{c}{16\pi}(E^* \times B + E \times B^*) \,. \tag{D.69}$$

The B field can be expressed in terms of the E field using the Faraday law

$$\nabla_r \times E = ik_0 B \,, \tag{D.70}$$

with the result

$$\langle S\rangle = \frac{c}{8\pi k_0}\text{Im}\left[E^* \times (\nabla_r \times E)\right] \,. \tag{D.71}$$

Returning to normalized x/L units, defining $F = (16\pi/c)\langle S\rangle$, one has

$$F(\kappa,x) = \frac{2}{\kappa}\text{Im}[E^*(\kappa,x) \times (\nabla \times E(\kappa,x))] \,. \tag{D.72}$$

For the specific case of a complex eikonal wave (1.30) with amplitude given by (1.56), flux (D.72) becomes

$$F_{\mathrm{CGO}}(\kappa,x)=\underbrace{[2\nabla S-(e^*\cdot\nabla S)e-(e\cdot\nabla S)e^*]}_{\alpha}e^{-2\kappa\phi}|A|^2+O(1/\sqrt{\kappa})\,. \tag{D.73}$$

Even if it is not used nor important in this context, it is interesting to note that the $\mathrm{O}(1/\sqrt{\kappa})$ term is in the form

$$(\nabla\phi\cdot R)e^{-2\kappa\phi}|A|^2+O(1/\kappa)\,, \tag{D.74}$$

with the R matrix given by

$$R_{ij}=2\mathrm{Im}\left[e_ie_j^*+2\left(e^*\cdot\frac{\partial e}{\partial N_i}\right)N_j+\left(N\cdot\frac{\partial e^*}{\partial N_i}\right)e_j+(N\cdot e)\frac{\partial e_j^*}{\partial N_i}\right]\,. \tag{D.75}$$

Now we point out that α term in (D.73) is equal to V. In fact

$$\begin{aligned}V=\frac{\partial H}{\partial N_k}&=e^*\cdot\frac{\partial D_0}{\partial N_k}e\\&=e^{*i}2\frac{\partial S}{\partial x^l}\delta^{lk}\delta_{ij}e^j-e^{*i}\delta_i^k\frac{\partial S}{\partial x^j}e^j-e^{*i}\frac{\partial S}{\partial x^i}\delta_j^ke^j\\&=2\frac{\partial S}{\partial x^l}\delta^{lk}-e^{*k}\frac{\partial S}{\partial x^j}e^j-e^{*i}\frac{\partial S}{\partial x^i}e^k=[\alpha]_k\,,\end{aligned} \tag{D.76}$$

where (D.56) and (D.2b) (with all quantities evaluated at $(x,\nabla S)$ instead of $(x,\nabla\psi)$) were taken into account in third and fourth equivalence respectively. It follows that

$$F_{\mathrm{CGO}}(\kappa,x)=V(x)e^{-2\kappa\phi(x)}|A(x)|^2+O(1/\sqrt{\kappa})\,. \tag{D.77}$$

In physical units, the corresponding Poynting vector reads

$$\frac{c}{16\pi}F_{\mathrm{CGO}}(\kappa,x)=v_g(x)W_{\mathrm{CGO}}(x)+O(1/\sqrt{\kappa})\,, \tag{D.78}$$

with $W_{\mathrm{CGO}}(x)$ formally given by

$$W_{\mathrm{CGO}}(x)=e^{-2\kappa\phi(x)}W_{\mathrm{GO}}(x)\,, \tag{D.79}$$

where v_g is formally equivalent to (1.26) and $W_{\mathrm{GO}}(x)$ expression given in (1.27). Summing up, in the Complex geometrical optics framework, the dominant order of the Pointing flux is the same as the GO one, except from an exponential decaying factor $e^{-2\kappa\phi}$, that controls the localization of the beam around the reference ray.

In order to obtain the energy transport equation, we turn back to Eq. (D.66). First of all it is worth noting that the term in squared brackets is equal to the dominant order of F_{CGO} (Eq. (D.77)), apart from a factor $e^{-2\kappa\phi}$. Since we are interested to estimate the divergence of the dominant order term of the flux F_{CGO}, we want to include the $e^{-2\kappa\phi}$ factor in the brackets. This is easy to be done, using Eq. (1.67). In fact

$$\nabla\cdot[Ve^{-2\kappa\phi}|A|^2]=e^{-2\kappa\phi}\nabla\cdot[V|A|^2]-2\kappa e^{-2\kappa\phi}|A|^2\underbrace{V\cdot\nabla\phi}_{=0}\,, \tag{D.80}$$

and hence, from Eq. (D.66) and Eq. (D.80) it follows that

$$\nabla \cdot [V e^{-2\kappa\phi}|A|^2] = -2\gamma_1 e^{-2\kappa\phi}|A|^2 \,, \tag{D.81}$$

which, restoring dimensional quantities, gives rise to

$$\nabla_r \cdot [v_g W_{\mathrm{CGO}}] = -\gamma W_{\mathrm{CGO}} \,, \tag{D.82}$$

with group velocity v_g and energy absorption coefficient γ formally equal to GO expressions (1.26) and (1.28) respectively, and W_{CGO} given in (D.79). Equation (D.82) is formally equal to GO one (Eq. (1.25)), but the equivalence is purely formal, because in the CGO framework all the phase functions (like $H(x, N)$) have to be evaluated at $N = \nabla S$, where $S(x)$ is different from the GO namesake, taking into account all the diffraction effects.

Just to check, let us show that Eq. (D.81) (and thus Eq. (D.82), restoring dimensional units) can be directly obtained taking the divergence of Eq. (D.72), substituting the CGO electric field ansatz, and retaining only the dominant order term. If the divergence of Eq. (D.72) is taken, from (1.1), recalling that

$$\epsilon(\kappa, x) = \epsilon_0^h(x) + \kappa^{-1}\epsilon_1^a + O(\kappa^{-2}) \,, \tag{D.83}$$

one finds

$$\nabla \cdot F = -2E^* \cdot \epsilon_1^a E + O(\kappa^{-1}) \,. \tag{D.84}$$

In fact one has

$$\begin{aligned} \nabla \cdot F &= \frac{1}{i\kappa}[\nabla \cdot (E^* \times (\nabla \times E)) - \nabla \cdot (E \times (\nabla \times E^*))] \\ &= \frac{1}{i\kappa}[-E^* \cdot \nabla \times (\nabla \times E) + E \cdot \nabla \times (\nabla \times E^*)] \\ &= -\frac{\kappa}{i}[E_i^*(\epsilon_{ij} - \epsilon_{ji}^*)E_j] = -2\kappa E_i^* \left(\frac{\epsilon_{ij} - \epsilon_{ji}^*}{2i}\right) E_j \\ &= -2\kappa E^* \cdot \epsilon^a E = -2E^* \cdot \epsilon_1^a E + O(\kappa^{-1}) \,, \end{aligned} \tag{D.85}$$

where in the second equality it was used the vector identity

$$\nabla \cdot A \times B = B \cdot \nabla \times A - A \cdot \nabla \times B \,, \tag{D.86}$$

and in the third equality Eq. (1.1) was taken into account. Eq. (D.84) shows that F is a conserved flux in a non-dissipative medium ($\epsilon_1^a = 0$).
Now it is possible to substitute the CGO electric field expression

$$\begin{aligned} E_{\mathrm{CGO}}(\kappa, x, t) &= A(x)\tilde{e}(x, \nabla\psi(x))e^{-\kappa\phi + i\kappa S - i\omega t} + O(\kappa^{-1}) \\ &= A(x)e(x, \nabla S(x))e^{-\kappa\phi + i\kappa S - i\omega t} + O(\kappa^{-1/2}) \,, \end{aligned} \tag{D.87}$$

obtaining

$$\nabla \cdot F = -2(e^* \cdot \epsilon_1^a e)e^{-2\kappa\phi}|A|^2 + O(\kappa^{-1/2}) = -2\gamma_1 e^{-2\kappa\phi}|A|^2 + O(\kappa^{-1/2}) \,, \tag{D.88}$$

consistently with Eq. (D.81) at the dominant order, as was expected.

APPENDIX E

Overview of the GRAY code

The beam tracing code GRAY performs the computation of the quasi-optical propagation of a Gaussian beam of electron cyclotron waves in a general tokamak equilibrium, and of the power absorption and driven current. The propagation of a general astigmatic Gaussian beam is described within the framework of the complex eikonal approach in terms of a set of "extended" rays that allow for diffraction effects. The absorbed power and the driven current density are computed along each ray solving the fully relativistic dispersion relation for electron cyclotron wave and by means of the neoclassical response function for the current.

E.1 Beam tracing equations

The GRAY code solves Eq. (1.65), (1.66) and (1.70), with the Hamiltonian

$$H(x,N) = N^2 - n^2(x,N_\parallel)\ , \tag{E.1}$$

where $n^2(x,N_\parallel)$ is obtained from the Altar-Appleton-Hartree dispersion relation for high-frequency waves in cold magnetized plasmas and $N_\parallel = b(x)\cdot N$ is the real parallel refractive index, with $b(x)$ the unit vector of the local equilibrium magnetic field. The complex extension, cf. Eq. (D.33), gives the effective Hamiltonian

$$H_\phi(x,N) = N^2 - n^2(x,N_\parallel) - |\nabla\phi(x)|^2 + \frac{1}{2}\frac{\partial^2 n^2(x,N_\parallel)}{\partial N_\parallel^2}(b(x)\cdot\nabla\phi(x))^2\ . \tag{E.2}$$

Three choices for the integration variable τ of the quasi-optical ray-tracing equations (1.65), (1.66) and (1.70) are available, i.e., the arc length along the trajectory s, the "time" ct, and the real part of the eikonal function S. The default option is the variable s and the QO ray equations become

$$\begin{aligned}
\frac{dx}{ds} &= \left.\frac{\partial H_\phi/\partial N}{|\partial H_\phi/\partial N|}\right|_{H_\phi=0}\ , \\
\frac{dN}{ds} &= -\left.\frac{\partial H_\phi/\partial x}{|\partial H_\phi/\partial N|}\right|_{H_\phi=0}\ , \\
\frac{\partial H_\phi}{\partial N}&\cdot\nabla\phi = 0\ .
\end{aligned} \tag{E.3}$$

The algorithm for the quasi-optical ray-tracing equations solution is described in detail in [6].

E.2 Coordinate systems and general astigmatic Gaussian beam description

A few sets of coordinate systems are used in the code:

The reference "laboratory" system is the right handed cartesian orthogonal system $(x_{\rm lab}, y_{\rm lab}, z_{\rm lab})$ with $z_{\rm lab}$ axis being the tokamak symmetry axis. For the purpose of the physics analysis this coordinate system may be rotated around the $z_{\rm lab}$-axis so that the $x_{\rm lab}z_{\rm lab}$ plane contains the launching point, i.e., $z_{\rm lab}$ vertical, $x_{\rm lab}$ radially outward through the port center, and $y_{\rm lab}$ pointing in the counter clockwise direction when viewed from above.

In addition to the right handed cartesian orthogonal system specified above, we introduce also a right-handed cylindrical system (R, φ, Z) with transformation from the cylindrical to the cartesian system given by $x_{\rm lab} = R\cos\varphi$, $y_{\rm lab} = R\sin\varphi$, $z_{\rm lab} = Z$.

Moreover, locally a reference system (x, y, z) is introduced, in which the z axis is directed along the direction of propagation of the beam and the x axis lies in the horizontal plane (i.e., $z_{\rm lab} = {\rm const}$).

$$\begin{aligned} \hat{z} &= \hat{k}_{11} = \frac{k_{11}}{|k_{11}|} \,, \\ \hat{x} &= \frac{\hat{k}_{11} \times \hat{z}_{\rm lab}}{|\hat{k}_{11} \times \hat{z}_{\rm lab}|} \,, \\ \hat{y} &= \hat{z}_{\rm lab} \times \hat{x} \,, \end{aligned} \tag{E.4}$$

where k_{11} is the reference ray's wave vector, and $\hat{z}_{\rm lab}$ is the unit vector pointing in the z direction.The (x, y, z) coordinates are obtained from the laboratory coordinates by the following rotation:

$$\begin{aligned} x &= x_{\rm lab}\cos\bar{\delta} - y_{\rm lab}\sin\bar{\delta} \,, \\ y &= \left(x_{\rm lab}\sin\bar{\delta} + y_{\rm lab}\cos\bar{\delta}\right)\cos\gamma - z_{\rm lab}\sin\gamma \,, \\ z &= \left(x_{\rm lab}\sin\bar{\delta} + y_{\rm lab}\cos\bar{\delta}\right)\sin\gamma + z_{\rm lab}\cos\gamma \,, \end{aligned} \tag{E.5}$$

where

$$\begin{aligned} \gamma &= \hat{k}_{11} \cdot \hat{z}_{\rm lab} \,, \\ \delta &= \arctan\left(\frac{\hat{k}_{11} \cdot \hat{y}_{\rm lab}}{\hat{k}_{11} \cdot \hat{x}_{\rm lab}}\right) \,, \\ \bar{\delta} &= \frac{\pi}{2} - \delta \,. \end{aligned} \tag{E.6}$$

These coordinate system is sufficient to describe a non-astigmatic Gaussian beam (cf. Appendix B).

In general, due to the particular optical system of the wave source, we have to deal with general astigmatic Gaussian beams, characterized by intensity and phase varying in the plane transversal to the direction of propagation as 2D elliptic Gaussian functions,

with a non-vanishing angle between their principal axes. The spatial dependence of the electric field of a general astigmatic Gaussian beam can be written in the form

$$E \propto \exp - \left(A_w x^2 + B_w y^2 + C_w xy\right) \exp \left[z + \left(A_R x^2 + B_R y^2 + C_R xy\right)\right], \tag{E.7}$$

with real coefficients (A_R, B_R, C_R) and (A_w, B_w, C_w) that depend on the z variable. The subscripts R, w depend on the fact that (A_R, B_R, C_R) are related to the local radii of curvature R_ξ, R_η of the phase front and (A_w, B_w, C_w) are related to the local beam sizes w_ξ, w_η. In fact, Eq. (E.7) can be rewritten to emphasize the elliptic shape of the constant phase and constant amplitude contours, introducing two additional coordinate systems, (ξ_w, η_w) and (ξ_R, η_R) in the (x, y) plane, rotated by the angles φ_w and φ_R, respectively,

$$\begin{aligned} x &= \xi_w \cos\varphi_w - \eta_w \sin\varphi_w = \xi_R \cos\varphi_R - \eta_R \sin\varphi_R \\ y &= \xi_w \sin\varphi_w + \eta_w \cos\varphi_w = \xi_R \sin\varphi_R + \eta_R \cos\varphi_R \end{aligned} \tag{E.8}$$

In the (ξ_w, η_w) and (ξ_R, η_R) systems, the axes are aligned with the major and minor axes of the intensity and phase ellipses respectively, and the general astigmatic Gaussian beam in vacuum takes the simple form (cf. [11])

$$E \propto \exp\left[-\left(\frac{\xi_w^2}{w_\xi^2} + \frac{\eta_w^2}{w_\eta^2}\right)\right] \exp\left[ik_0\left(z + \frac{\xi_R^2}{2R_\xi} + \frac{\eta_R^2}{2R_\eta}\right)\right]. \tag{E.9}$$

In particular, the radii of curvature R_ξ, R_η and local beam sizes w_ξ, w_η are related with the (A_R, B_R, C_R) and (A_w, B_w, C_w) coefficients as follows:

$$R_\xi = 1/(2\mathcal{K}_\xi)\,, \quad R_\eta = 1/(2\mathcal{K}_\eta) \tag{E.10}$$

$$w_\xi = 1/\sqrt{\mathcal{W}_\xi}\,, \quad w_\eta = 1/\sqrt{\mathcal{W}_\eta}\,, \tag{E.11}$$

where

$$\mathcal{K}_\xi = \frac{1}{2}\left[A_R + B_R + \frac{A_R - B_R}{\cos(2\varphi_R)}\right]\,, \quad \mathcal{K}_\eta = A_R + B_R - \mathcal{K}_\xi\,, \tag{E.12}$$

$$\mathcal{W}_\xi = \frac{1}{2}\left[A_w + B_w + \frac{A_w - B_w}{\cos(2\varphi_w)}\right]\,, \quad \mathcal{W}_\eta = A_w + B_w - \mathcal{W}_\xi\,, \tag{E.13}$$

with

$$\begin{aligned} \varphi_R &= \frac{1}{2}\arctan\frac{C_R}{A_R - B_R}\,, \\ \varphi_w &= \frac{1}{2}\arctan\frac{C_w}{A_w - B_w}\,. \end{aligned} \tag{E.14}$$

A general astigmatic Gaussian beam is described in terms of six parameters: the beam widths $w_{\xi,\eta}$, the phase front curvature radii $R_{\xi,\eta}$ and the intensity and phase ellipses rotation angles $\varphi_{w,R}$.

Simple astigmatic beams can be described in terms of 5 parameters only, because the

phase and intensity ellipses are aligned, i.e., $\varphi_w = \varphi_R \equiv \varphi$: $w_{\xi,\eta}$, $R_{c\xi,\eta}$, φ or alternatively by the beam waists $w_{0\xi,\eta}$, the waists z coordinates $d_{0\xi,\eta}$, and φ, where $R_{\xi,\eta}$, $w_{\xi,\eta}$ are related to $d_{0\xi,\eta}$, $w_{0\xi,\eta}$ by equations formally equal to (1.34) and (1.35):

$$w_j(z) = w_{0j}\sqrt{1+\left(\frac{z-d_{0j}}{z_{Rj}}\right)^2}\,, \tag{E.15}$$

$$R_j(z) = (z-d_{0j})\left[1+\left(\frac{z_{Rj}}{z-d_{0j}}\right)^2\right]\,, \tag{E.16}$$

where $j = \xi, \eta$ and $z_{Rj} = k_0 w_{0j}^2/2$ are the Rayleigh lengths. According to Eq. (E.16), a convergent beam ($z < d_{0j}$) has $R_j < 0$, while a divergent beam has $R_j > 0$.

E.3 Ray initial conditions

The QO ray equations (E.3) are solved for $N_T = (N_r - 1) \times N_\theta + 1$ rays distributed in order to simulate the Gaussian pattern of an actual antenna, with initial position on a suitable surface at the antenna centered on the beam axis.
The N_r rays are distributed radially up to a "cut-off" "radius" $\rho_{\max}$ defined as $\rho_{\max} = \kappa\phi_{\max}$ such that the beam carries a fraction of the input power equal to $[1-\exp(-2\rho_{\max}^2)]$. In fact, defining the adimensional radial coordinate $\rho = \kappa\phi$, it follows that

$$\begin{aligned}\frac{P_{\rm in}(\text{up to } \rho_{\max})}{P_{\rm in}} &= \frac{\int_0^{\rho_{\max}} |E(\rho)|^2 2\pi\rho\,\mathrm{d}\rho}{\int_0^{\infty} |E(\rho)|^2 2\pi\rho\,\mathrm{d}\rho} \\ &= \frac{\int_0^{\rho_{\max}} e^{-2\rho^2}\,2\pi\rho\,\mathrm{d}\rho}{\int_0^{\infty} e^{-2\rho^2}\,2\pi\rho\,\mathrm{d}\rho} = 1-\exp(-2\rho_{\max}^2)\,.\end{aligned} \tag{E.17}$$

The N_θ angular rays are distributed at constant electric field amplitude (i.e. at ϕ = const). For details we refer to [6].

E.4 Launching coordinates and wave vector

The launching coordinates of the central ray of the EC beam will be denoted either as $(x_{\rm lab,0}, y_{\rm lab,0}, z_{\rm lab,0})$, or (R_0, ϕ_0, Z_0), depending on the coordinate system used (cartesian or cylindrical)

$$x_{\rm lab,0} = R_0\cos\phi_0, \quad y_{\rm lab,0} = R_0\sin\phi_0, \quad z_{\rm lab,0} = Z_0. \tag{E.18}$$

and the launched refractive index vector N will have components (N_{x0}, N_{y0}, N_{z0}), and $(N_{R0}, N_{\varphi 0}, N_{Z0})$, related by

$$\begin{aligned} N_{x0} &= N_{R0}\cos\varphi_0 - N_{\phi 0}\sin\varphi_0, \\ N_{y0} &= N_{R0}\sin\varphi_0 + N_{\phi 0}\cos\varphi_0 \\ N_{z0} &= N_{Z0} \end{aligned} \tag{E.19}$$

E.5 EC Launching angles

The poloidal and toroidal launching angles α, β are defined in terms of the cylindrical components of the refractive index vector

$$\begin{aligned} N_{R0} &= -\cos\beta\cos\alpha, \\ N_{\varphi 0} &= \sin\beta, \\ N_{Z0} &= -\cos\beta\sin\alpha\ . \end{aligned} \tag{E.20}$$

with $-180° \leq \alpha \leq 180°$, and $-90° \leq \beta \leq 90°$, so that

$$\begin{aligned} \tan\alpha &= N_{Z0}/N_{R0}, \\ \sin\beta &= N_{\varphi 0}\ . \end{aligned} \tag{E.21}$$

A 1-D scan of launch angle with constant toroidal component at launch ($N_{\varphi 0}$) is achieved by varying only α, keeping β fixed. Injection at $\beta = 0, \alpha = 0$ results in a ray launched horizontally and in a poloidal plane towards the machine centre. The above choice is quite convenient to perform physics simulations, since EC results are invariant under toroidal rotation, due to axisymmetry. This convention is the same used for the EC injection angles in ITER.

E.6 EC absorption model

The EC power P is assumed to evolve along the ray trajectory obeying to the following equation

$$\frac{dP}{ds} = -\alpha P\ , \tag{E.22}$$

where here α is the absorption coefficient. This equation is obtained integrating Eq. (1.82) on a portion of flux tube of section $\delta S(s)$ around the considered ray, between s and $s + ds$, of volume $\delta S ds = \delta S |v_g| dt$, and putting $\alpha = \gamma/|v_g|$. The absorption coefficient is actually computed using the relativistic dispersion relation as

$$\alpha = 2\frac{\omega}{c}\left.\frac{\mathrm{Im}(H_w)}{|\partial H/\partial N|}\right|_{H=0} \simeq 4\frac{\omega}{c}\mathrm{Im}(N_{\perp w})\left.\frac{N_\perp}{|\partial H/\partial N|}\right|_{H=0} = 2\mathrm{Im}(k_{\perp w})\frac{v_{g\perp}}{|v_g|}\ , \tag{E.23}$$

being $N_{\perp w}$ (and $k_{\perp w}$) the perpendicular refractive index (and wave vector) solution of the relativistic dispersion relation for EC waves

$$H_w = N^2 - N_\parallel^2 - N_{\perp w}^2 = 0\ . \tag{E.24}$$

The (E.23) expressions follow from the fact that the absorption coefficient can be written in the form

$$\alpha = 2\mathrm{Im}(k)\cdot\frac{v_g}{|v_g|} \tag{E.25}$$

(cf. Bornatici et al. [25]), that is equivalent to Eq. (1.28), as it is demonstrated in section 4.3 of Akhiezer's book [26], and the following assumptions are made. First, the ratio $v_g/|v_g|$ is estimated using the cold dispersion relation. Secondly the $\mathrm{Im}(k)$ term is estimated using the relativistic dispersion relation, assuming that $k_\parallel$ is purely real. We refer to [27] for details on the relativistic dispersion relation solution.

Integrating Eq. (E.22), the power transmitted by the wave up to the archlength s can be obtained:

$$P(s) = P_0 e^{-\tau(s)} \,, \tag{E.26}$$

where

$$\tau(s) = \int_0^s \alpha(s^{'})\mathrm{d}s^{'} \tag{E.27}$$

is denoted "optical depth" and P_0 is the injected power. As a consequence, the power deposited up to archlength s is

$$P_{abs}(s) = P_0[1 - e^{-\tau(s)}] \,. \tag{E.28}$$

E.7 ECRH&CD location and profile characterization

Implementing an appropriate ECCD model (Cohen model or momentum-conservation model) the driven current and absorbed power density profiles, $J_{cd}(\rho)$, $p(\rho)$, is computed, where here ρ denotes the normalized toroidal radius defined as in section 0.2. This profiles can be characterized in term of suitable quantities. In GRAY, two approaches are followed. In the former case, the profiles are characterized in terms of three quantities: the peak value, the "radius" ρ corresponding to the peak, and the full profile width at 1/e of the peak value. In the latter case, two average quantities are computed for each profile, namely the averaged radius $\langle\rho\rangle_f$ with $f = p, J$

$$\langle\rho\rangle_p = \frac{\int dV\,\rho\, p(\rho)}{\int dV p(\rho)} \,, \qquad \langle\rho\rangle_J = \frac{\int dA\;\rho|J_{cd}(\rho)|}{\int dA|J_{cd}(\rho)|} \,, \tag{E.29}$$

and average profile width $\overline{\Delta\rho}_f$ defined in terms of the variance as

$$\overline{\Delta\rho}_f = 2\sqrt{2}\langle\Delta\rho\rangle_f \qquad \text{with} \qquad \langle\Delta\rho\rangle_f^2 = \langle\rho^2\rangle_f - (\langle\rho\rangle_f)^2 \,. \tag{E.30}$$

In the integral in $\langle\rho\rangle_p$ definition the volume element dV is given by the volume enclosed between the $\rho-$labeled and $(\rho + d\rho)-$labeled magnetic surfaces. Similarly, in $\langle\rho\rangle_j$ definition the surface element dA consists in the surface enclosed by the $\rho-$labeled and $(\rho + d\rho)-$labeled magnetic surfaces intersections with the poloidal plane. The above definitions (E.29), (E.30) apply also to the case of non monotonic profiles. Note that the average values coincide with the peak values in case of almost Gaussian profiles. Factor $\sqrt{8}$ is introduced to match with full profile width in case of Gaussian profile.

APPENDIX F

Numerical computation of the beam transversal spectrum

F.1 Routine description

The first part of the routine computes the values of the real and imaginary part of the eikonal function on the plane xy perpendicular to k_{11} according to Eqs. (3.34). Actually, instead of S, the difference $S - S_{11}$ is computed, where S_{11} is the S value on the reference ray. For the imaginary part of the eikonal this translation is not needed because $\phi_{11} = 0$.

It is possible to avoid this projection step properly choosing the integration variable of the hamiltonian equations. This alternative is not currently present in the GRAY routine, but it is presented in the second section of this Appendix.

The field can be written in the eikonal form

$$E(x, y) \propto e^{ik_0[S(x,y)+i\phi(x,y)]} \equiv E_{\text{num}}(x, y) \ , \tag{F.1}$$

where the subscript "num" stands for "numerical", in order to distinguish the values computed by this E field expression from those obtained by the local Gaussian model, that will be denoted E_{Gauss}.

In order to compute its numeric Fourier transform, it is needed to know the values of $E_{\text{num}}(x, y)$ on a regular grid $(x(i), y(j))$ with $i = 1, \ldots, N_x$ and $j = 1, \ldots, N_y$ (N_x and N_y odd integer numbers, in order to have a central point, needed by the Fourier transform algorithm). For simplicity we chose a square grid with $N_x = N_y \equiv N_g = 2N_r - 1$, where N_r is the number of rays in the radial direction and the subscript "g" stands for "grid". To obtain this result a spline fit with an external routine is performed and the spline function is evaluated on a regular grid with an another routine. The extension of the grid is tuned to cover the spot of the beam, with a little remainder, as follows:

$$\Delta x = \Delta y = (1 + \epsilon) \max \left[\sqrt{x_{jk}^2 + y_{jk}^2} \ ; \ j = 1, \ldots, N_r \ , \ k = 1, \ldots, N_\theta \right] \tag{F.2}$$

with $\epsilon \sim 1/10$. Here the notation x_{jk} indicates the x component of the vector $(x, y, z)_{jk}$, instead of the whole vector.

With the aim to get a best outcome from the Fourier transform routine, it is better to give as input a function that is vanishingly small at the border of the grid. Therefore we chose to give as input the difference between (F.1) and the Gaussian model field and in a second step to add to the result the analytic transform of the Gaussian model field.

The difference between (F.1) and the Gaussian model field on the grid is computed as follows:

$$\Delta E((x(i), y(j))) = E_{\rm num}(x(i), y(j)) - E_{\rm Gauss}(x(i), y(j)) \tag{F.3}$$

with

$$\begin{aligned} E_{num}(x(i), y(j)) &= \exp\{ik_0[S(x(i), y(j)) + i\phi(x(i), y(j))]\} \\ E_{Gauss}(x(i), y(j)) &= \exp\{i[Ax(i)^2 + By(j)^2 + Cx(i)y(j)]\}\ , \end{aligned} \tag{F.4}$$

where A, B, C are the components of the M matrix (3.21). In order to minimize the border effects on the transform, a window function is multiplied to $\Delta E(x, y)$ (cf. Fig. F.1):

$$f_w(x, y) = \frac{1}{2}\left\{1 + \cos\left[\pi\ \frac{\max\left(\rho_0, \min(\sqrt{x^2 + y^2}, \rho_{\max})\right) - \rho_0}{\rho_{\max} - \rho_0}\right]\right\}\ , \tag{F.5}$$

where $\rho_{\max}$ is the maximum between the two local beam sizes w_ξ, w_η (cf. Appendix E.2) and ρ_0 is chosen as $\rho_0 = \rho_{\max}/2$.

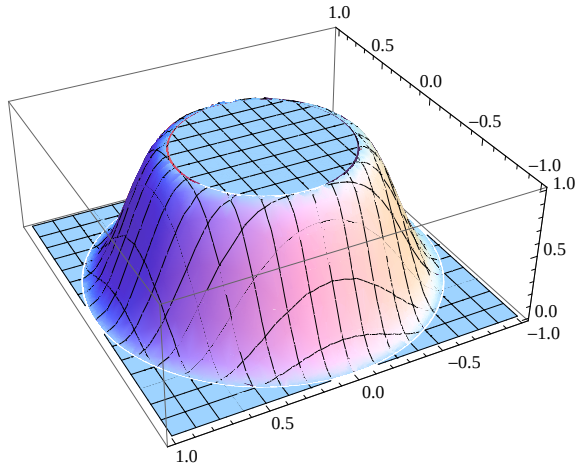

Figure F.1: $f_w(x, y)$ plot with $\rho_{\max} = 1$ and $\rho_0 = 0.5\rho_{max}$

In order to improve the resolution of the spectrum, $\Delta E_w(x, y) = \Delta E(x, y) f_w(x, y)$ is evaluated on a larger concentric square grid $\{(\bar{x}(i), \bar{y}(j))\ ,\ i, j = 1, \ldots, \bar{N}_g\}$ putting zero values on the nodes outside the original grid. In particular we chose a second grid with four times the surface of the first one ($\bar{N}_g = 2N_g - 1$). The $\Delta E_w(x, y)$ values on the new grid are computed in two steps: first of all the values on the new grid are put to zero, and then the center of the grid is filled as follows:

$$\Delta E_w\left[\bar{x}\left(i + \frac{N_g - 1}{2}\right), \bar{y}\left(i + \frac{N_g - 1}{2}\right)\right] = \Delta E_w\left(x(i), y(j)\right) \tag{F.6}$$

for $i, j = 1, \ldots, N_g$.

Now the $\{\Delta E_w(\bar{x}(i), \bar{y}(j)),\ i, j = 1, \ldots, \bar{N}_g\}$ values are given as input to an external 2D FFT routine. The output is given on a square grid $(\bar{k}_x(i), \bar{k}_y(j))$ with $i, j = 1, \ldots, \bar{N}_g$,

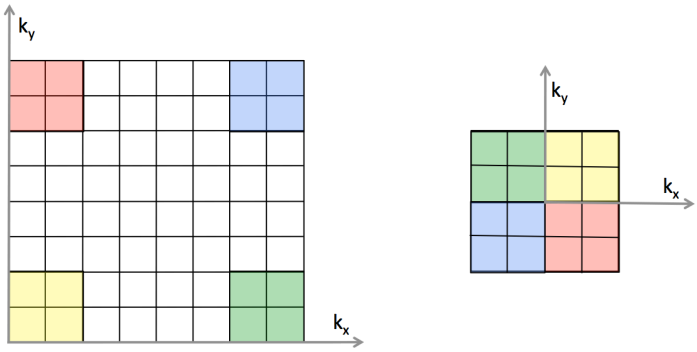

Figure F.2: The two k grids with $\bar{N} = 10$

and the k spacing between grid points is $\Delta k = 2\pi/(\Delta x\ \bar{N}_g)$, where Δx is the x spacing between the original grid points. The output points are referred to positive values of k_x and k_y ($0 < k_x < \bar{N}_g \Delta k\ ,\ 0 < k_y < \bar{N}_g \Delta k$) but the output function is periodic with period $\bar{N}_g \Delta k/2$ both in k_x and k_y directions. Since we are interested to center the peak of the transformed Gaussian at $k_x = k_y = 0$, we evaluate the FFT output on a smaller grid around the origin of the axes. In particular a square grid $\{(k_x(i), k_y(j))\ ,\ i, j = 1, N_g\}$ of a quarter of the original surface is considered, centered in $(k_x = 0\ ,\ k_y = 0)$. To do this we exploit the periodicity of the function (cf. Fig. F.2). If we call $\widetilde{\Delta E}_w(\bar{k}_x(i), \bar{k}_y(j))$ the output of the FFT, the part evaluated on the smaller grid can be computed as follows:

$$\widetilde{\Delta E}_w(k_x(i), k_y(j)) = \widetilde{\Delta E}_w \left[\bar{k}_x \left(\mod \left(i + 3\frac{N_g - 1}{2}, \bar{N} \right) + 1, \right), \right. \\ \left. \bar{k}_y \left(\mod \left(j + 3\frac{N_g - 1}{2}, \bar{N} \right) + 1 \right) \right] \tag{F.7}$$

for $i, j = 1, \ldots, N_g$.

At this point the analytic transform of the Gaussian model electric field is added to $\widetilde{\Delta E}_w$ and the obtained function is normalized by its peak value:

$$\tilde{E}'_{\mathrm{num}}(k_x(i), k_y(j)) = \widetilde{\Delta E}_w(k(i), k(j)) + \\ + \frac{i}{\sqrt{\Delta}} \exp\{i[Bk_x(i) + Ak_y(j) - Ck_x(i)k_y(j)]/\Delta\} \tag{F.8}$$

$$\tilde{E}_{\mathrm{num}}(k_x(i), k_y(j)) = \tilde{E}'_{\mathrm{num}}(k_x(i), k_y(j))/\tilde{E}'_{\mathrm{num}}(k_x(i_0), k_y(j_0)) \tag{F.9}$$

with Δ equal to -4 times the determinant of the M matrix (cf. 3.21). Moreover, $i_0 = i(k_x = 0)$ and $j_0 = j(k_y = 0)$.

Disregarding the phase, the routine computes

$$|\tilde{E}_{\mathrm{Gauss}}|(k_x(i), k_y(j)) = |\exp\{i[Bk_x(i) + Ak_y(j) - Ck_x(i)k_y(j)]/\Delta\}|\ , \\ |\tilde{E}_{\mathrm{num}}|(k_x(i), k_y(j)) = |\tilde{E}'_{num}(k_x(i), k_y(j))/\tilde{E}'_{num}(k_x(i_0), k_y(j_0))| \tag{F.10}$$

The mean squared error D between the modules $|\tilde{E}_{\text{Gauss}}|$ and $|\tilde{E}_{\text{num}}|$ is obtained considering only the central $(n+1)^2$ points (with $n < N_r$) to minimize the border effects eventually due to the spline interpolation, and it is computed as follows:

$$D = \sqrt{\frac{1}{(n+1)^2} \sum_{i,j=\frac{N_g+1}{2}-n}^{\frac{N_g+1}{2}+n} \left[|\tilde{E}_{\text{Gauss}}|(k_x(i), k_y(j)) - |\tilde{E}_{\text{num}}|(k_x(i), k_y(j)) \right]^2} . \tag{F.11}$$

F.2 An alternative way to integrate the extended ray equations

Let us consider the extended ray equations:

$$\begin{aligned} \frac{dx}{d\tau} &= \left. \frac{\partial H_\phi}{\partial N} \right|_{H_\phi = 0} , \\ \frac{dN}{d\tau} &= -\left. \frac{\partial H_\phi}{\partial N} \right|_{H_\phi = 0} , \\ \frac{d\phi}{d\tau} &= 0 . \end{aligned} \tag{F.12}$$

Differentiating the equation

$$(x - x_{11}) \cdot N_{11} = 0 \tag{F.13}$$

which states that x lies on the plane perpendicular to N_{11} passing through x_{11}, the position of the reference ray point, and recalling that $dS_{11} = dx_{11} \cdot N_{11}$, we obtain

$$\frac{dS_{11}}{d\tau} = N_{11} \cdot \frac{\partial H_\phi}{\partial N} - \left. \frac{\partial H_\phi}{\partial x} \right|_{11} \cdot (x - x_{11}) \tag{F.14}$$

From (F.12) and (F.14) the following equations hold

$$\begin{aligned} \frac{d\mathbf{x}}{dS_{11}} &= \left[N_{11} \cdot \frac{\partial H_\phi}{\partial N} - \left. \frac{\partial H_\phi}{\partial x} \right|_{11} \cdot (x - x_{11}) \right]^{-1} \left. \frac{\partial H_\phi}{\partial N} \right|_{H_\phi = 0} , \\ \frac{dN}{dS_{11}} &= -\left[N_{11} \cdot \frac{\partial H_\phi}{\partial N} - \left. \frac{\partial H_\phi}{\partial x} \right|_{11} \cdot (x - x_{11}) \right]^{-1} \left. \frac{\partial H_\phi}{\partial x} \right|_{H_\phi = 0} \\ \frac{d\phi}{dS_{11}} &= 0 . \end{aligned} \tag{F.15}$$

Equations (F.15), with initial conditions given on a plane, give rise to iterated points that lie on the plane perpendicular to the local N_{11} (that is perpendicular to the local k_{11}) passing through the local x_{11}, at each fixed value of the integration variable S_{11}.
These equations, together with

$$\frac{dS}{dS_{11}} = \left[N_{11} \cdot \frac{\partial H_\phi}{\partial N} - \left. \frac{\partial H_\phi}{\partial x} \right|_{11} \cdot (x - x_{11}) \right]^{-1} N \cdot \frac{\partial H_\phi}{\partial N} , \tag{F.16}$$

reconstruct the S function along the propagation.

I will now show as an example the integration of this system of equations in the simpler case of ray tracing $\phi = 0$, in a simple plasma configuration. In this section, from now on, for brevity I will mark with the symbol "$\sim$" the quantities relative to the reference ray instead of the subscript "11". Moreover, for clarity sake, the vectors will be written in bold character, in order to distinguish the x position vector from the x component.

Let us consider a weakly non-uniform cold plasma with density linearly varying in the x direction. The ray equations (F.15) (with $\phi = 0$ and therefore $H = H_\phi$) are written with the Hamiltonian :

$$H = N^2 - \left(1 - \frac{\omega_p^2}{\omega^2}\right) = N^2 - 1 + \frac{x}{L} \,, \tag{F.17}$$

with constant L, because ω is constant, $n \propto x$ and $\omega_p \propto \sqrt{n}$, n being the plasma density. Equations (F.15) become

$$\frac{d\mathbf{x}}{d\tilde{S}} = \left[2\tilde{N}_x N_x - \frac{x - \tilde{x}}{L}\right]^{-1} 2\mathbf{N}\bigg|_{H=0} \tag{F.18}$$

$$\frac{d\mathbf{N}}{d\tilde{S}} = \left[2\tilde{N}_x N_x - \frac{x - \tilde{x}}{L}\right]^{-1} \left(-\frac{1}{L}\right)\hat{x}\bigg|_{H=0} \tag{F.19}$$

and the corresponding equations relative to the reference ray are given by

$$\frac{d\tilde{\mathbf{x}}}{d\tilde{S}} = \frac{\tilde{\mathbf{N}}}{\tilde{N}_x^2}\bigg|_{H=0} \tag{F.20}$$

$$\frac{d\tilde{\mathbf{N}}}{d\tilde{S}} = -\frac{1}{2L\tilde{N}_x^2}\hat{x}\bigg|_{H=0} \tag{F.21}$$

Let us consider a beam propagating in the x direction with boundary conditions on the vacuum-plasma surface ($x = 0$). The boundary conditions for the reference ray are:

$$\tilde{x}(0) = \tilde{y}(0) = \tilde{z}(0) = 0 \,,\ \tilde{N}_x(0) = 1 \,,\ \tilde{N}_y(0) = \tilde{N}_z(0) = 0 \,. \tag{F.22}$$

The boundary conditions for the other rays are:

$$x(0) = 0 \,,\ y(0) = y_0 \,,\ z(0) = z_0 \,,\ N_x(0) = N_{0x} \,,\ N_y(0) = N_{0y} \,,\ N_z(0) = N_{0z} \,. \tag{F.23}$$

Before starting to solve the equations, it is possible to find out that the fact that $x(0) = \tilde{x}(0)$ implies that $x(\tilde{S}) = \tilde{x}(\tilde{S}) \,,\ \forall\ \tilde{S}$. It follows from $(F.18)$ and (F.20), which state that

$$\frac{d(x - \tilde{x})}{d\tilde{S}} = \left[\tilde{N}_x\left(2\tilde{N}_x N_x - \frac{x - \tilde{x}}{L}\right)\right]^{-1} \frac{x - \tilde{x}}{L} \,. \tag{F.24}$$

I will solve the equations in this order: $(F.21) \rightarrow (F.20) \rightarrow (F.19) \rightarrow (F.18)$.

Consider Eq. $(F.21)$. The y and z components have the trivial solution: $\tilde{N}_y(\tilde{S}) = \tilde{N}_z(\tilde{S}) = \tilde{N}_y(0) = \tilde{N}_z(0) = 0$. The x component is a separable ordinary differential equation, and it can be easily integrated to give

$$\tilde{N}_x(\tilde{S}) = \sqrt[3]{1 - \frac{3}{2}\frac{\tilde{S}}{L}} \,. \tag{F.25}$$

To solve $(F.19)$ and $(F.18)$ it is needed only to solve the x component of $(F.20)$. Substituting $(F.25)$ it can be easily integrated as follows (we recall that $\tilde{x}(0) = 0$):

$$\tilde{x}(\tilde{S}) = \int_0^{\tilde{S}} \frac{1}{\tilde{N}_x(\tau)} \mathrm{d}\tau = \int_0^{\tilde{S}} \sqrt[3]{1 - \frac{3}{2}\frac{\tau}{L}} \mathrm{d}\tau = \tag{F.26}$$
$$= L\left[1 - \left(1 - \frac{3}{2}\frac{\tilde{S}}{L}\right)^{\frac{2}{3}}\right] = L\left[1 - \tilde{N}_x^2(\tilde{S})\right] .$$

Now it is possible to go on and solve $(F.19)$. The y and z components have the trivial solutions $N_y = N_{0y}$ and $N_z = N_{0z}$ .The x component is given by

$$\frac{dN_x}{d\tilde{S}} = \left.\frac{1}{x - \tilde{x} - 2L\tilde{N}_x N_x}\right|_{H=0} . \tag{F.27}$$

The dispersion relation $H = 0$ is exploited in order to obtain $x(\mathbf{N})$:

$$x = L(1 - N_x^2 - N_y^2 - N_z^2) = L(1 - N_x^2 - N_{0y}^2 - N_{0z}^2) \equiv L(1 - N_x^2 - N_{0r}^2) . \tag{F.28}$$

Substituting $(F.28)$ into $(F.27)$ and changing variable from $\tilde{S}$ to $\tilde{N}_x$, the equation becomes:

$$(N_x^2 + 2\tilde{N}_x N_x - \tilde{N}_x^2 + N_{0r}^2)\frac{dN_x}{d\tilde{N}_x} = 2\tilde{N}_x^2 . \tag{F.29}$$

This equation can be put in the form:

$$[y(x)^2 + 2xy(x) - x^2 + c^2]y'(x) = 2x^2 , \tag{F.30}$$

with constant c. Let us solve it. Doing the change of variables $(x, y) \to (u = y + x\ ,\ v = y - x)$, the equation becomes:

$$du(2uv - v^2 + c^2) + dv(u^2 + c) = 0 . \tag{F.31}$$

With the restriction $0 \neq v = y - x = N_x - \tilde{N}_x$ (that is acceptable, because in the $v = 0$ case the solution is known, being the reference ray solution shifted by the initial position $(0, y_0, z_0)$) the further change of variables is done: $(u, v) \to (\alpha = u/c\ ,\ \beta = c/v)$. The equation becomes

$$\beta' + 1 = \frac{(\beta + \alpha)^2}{1 + \alpha^2} , \tag{F.32}$$

with $\beta' = d\beta/d\alpha$. Defining the function $g(\alpha) = \beta(\alpha) + \alpha$, the equation takes the form:

$$\frac{g'}{g^2} = \frac{1}{1 + \alpha^2} , \tag{F.33}$$

that is separable, with the solution:

$$-\frac{1}{g(\alpha)} = \arctan\alpha + \gamma \tag{F.34}$$

with γ being the integration constant. $\bar{\gamma} = \gamma^{-1}$ can be easily computed at the boundary by

$$\bar{\gamma} = \left.\frac{g(\alpha)}{g(\alpha)\arctan\alpha - 1}\right|_0 , \tag{F.35}$$

where, reminding that $y \equiv N_x$ and $x \equiv \tilde{N}_x$, we have

$$g(\alpha) = \frac{N_x^2 + N_{0r}^2 - \tilde{N}_x^2}{N_{0r} v(N_x, \tilde{N}_x)} \tag{F.36}$$
$$\arctan \alpha = \arctan\left(\frac{N_x + \tilde{N}_x}{N_{0r}}\right) .$$

In general $\arctan \alpha \neq 0$ but at the boundary (recalling that $v \neq 0$ for hypothesis) $g = 0$. As a consequence $\bar{\gamma} = 0$. From (F.36) it follows that

$$N_x(\tilde{N}_x) = \sqrt{\tilde{N}_x^2 - N_{0r}^2} \tag{F.37}$$

Finally it is possible to solve (F.18). To solve the x component it is sufficient to substitute (F.37) into $H = 0$, from which it follows that

$$x(\tilde{S}) = \tilde{x}(\tilde{S}) = L[1 - \tilde{N}_x(\tilde{S})^2] . \tag{F.38}$$

This is consistent with (F.24). Turning to y and z components, let us consider for example y. Substituting (F.37) and (F.38) into (F.18), we have

$$\frac{dy}{d\tilde{S}} = \frac{N_{0y}}{\tilde{N}_x(\tilde{S})\sqrt{\tilde{N}_x(\tilde{S})^2 - N_{0r}^2}} . \tag{F.39}$$

Changing variable from $\tilde{S}$ to $\tilde{N}_x$, the equation becomes

$$\frac{d\bar{y}}{d\tilde{N}_x} = -\frac{N_{0y}\tilde{N}_x}{\sqrt{\tilde{N}_x^2 - N_{0r}^2}} , \tag{F.40}$$

where $\bar{y} = y/2L$, that can be easily integrated obtaining:

$$\bar{y}(\tilde{N}_x) = \bar{y}_0 - N_{0y}\left[\sqrt{\tilde{N}_x^2 - N_{0r}^2} - \sqrt{1 - N_{0r}^2}\right] , \tag{F.41}$$

where $\bar{y}_0 = y_0/2L$.

The ray equations can be finally written in the following parametric form (recalling that $N_{0x}^2 = 1 - N_{0r}^2$):

$$x(\tilde{S}) = L\left[1 - \left(1 - \frac{3}{2}\frac{\tilde{S}}{L}\right)^{\frac{2}{3}}\right] , \tag{F.42}$$

$$y(\tilde{S}) = y_0 - 2LN_{0y}\left[\sqrt{\left(1 - \frac{3}{2}\frac{\tilde{S}}{L}\right)^{\frac{2}{3}} - N_{0y}^2 - N_{0z}^2} - N_{0x}\right] , \tag{F.43}$$

$$z(\tilde{S}) = z_0 - 2LN_{0z}\left[\sqrt{\left(1 - \frac{3}{2}\frac{\tilde{S}}{L}\right)^{\frac{2}{3}} - N_{0y}^2 - N_{0z}^2} - N_{0x}\right] , \tag{F.44}$$

or in the computationally faster form

$$x(\tilde{S}) = L\left[1 - \left(1 - \frac{3}{2}\frac{\tilde{S}}{L}\right)^{\frac{2}{3}}\right] , \tag{F.45}$$

$$y(\tilde{S}) = y_0 - 2LN_{0y}\left[\sqrt{N_{0x}^2 - \frac{x(\tilde{S})}{L}} - N_{0x}\right] , \tag{F.46}$$

$$z(\tilde{S}) = z_0 + \frac{N_{0z}}{N_{0y}}\left[y(\tilde{S}) - y_0\right] . \tag{F.47}$$

Now as a check I will derive the expression of the trajectory, that has to coincide with the well known parabolic form:

$$x(y,z) = \frac{N_{0x}}{\sqrt{N_{0y}^2 + N_{0z}^2}}\sqrt{(y-y_0)^2 + (z-z_0)^2} - \frac{1}{4L}\frac{(y-y_0)^2 + (z-z_0)^2}{N_{0y}^2 + N_{0z}^2} . \tag{F.48}$$

To obtain the trajectory, first of all from ($F.43$) and ($F.44$) it follows

$$\sqrt{N_{0x}^2 - 2\bar{x}} = N_{0x} - \frac{1}{2}\left(\frac{\bar{y} - \bar{y}_0}{N_{0y}} + \frac{\bar{z} - \bar{z}_0}{N_{0z}}\right) , \tag{F.49}$$

where the bar over the variable indicate the variable divided by $2L$ as before. From ($F.47$), defining $r = \sqrt{(y-y_0)^2 + (z-z_0)^2}$, the following expressions can be obtained:

$$\bar{y} - \bar{y}_0 = \frac{N_{0y}}{N_{0r}}\bar{r} , \tag{F.50}$$

$$\bar{z} - \bar{z}_0 = \frac{N_{0z}}{N_{0r}}\bar{r} . \tag{F.51}$$

Substituting ($F.50$) and ($F.51$) into ($F.49$), after a little algebra, we obtain

$$\bar{x}(\bar{r}) = \frac{N_{0x}}{N_{0r}}\bar{r} - \frac{1}{2N_{0r}^2}\bar{r}^2 , \tag{F.52}$$

that is equivalent to ($F.48$).
From ($F.43$) and ($F.44$) it follows that this solution exists only for $\tilde{S} < \tilde{S}_{\rm tp}$, with $\tilde{N}_x(\tilde{S}_{tp}) = N_{0r}$. The geometrical meaning of this fact is that $\tilde{S} = \tilde{S}_{\rm tp}$ is the turning point (with $\bar{x}_{\rm tp} = N_{0x}^2/2$) of the parabolic trajectory, and after that point do not exist values of $\tilde{S}$ which satisfy $x(\tilde{S}) = \tilde{x}(\tilde{S})$.

Finally, one example will be shown, obtained with a Fortran program that generates this trajectories starting from the initial conditions of a divergent non-astigmatic Gaussian beam propagating in the x direction. For a non-astigmatic Gaussian beam, the real part of the eikonal function is given by

$$S(x,y,z) = x\left(1 + \frac{1}{2}\frac{y^2 + z^2}{x^2 + x_R^2}\right) \tag{F.53}$$

where x_R is the Rayleigh length.

$$\begin{aligned} N_x &= \frac{\partial S}{\partial x} = 1 + \frac{1}{2}\frac{x_R^2 - x^2}{(x_R^2 + x^2)^2}(y^2 + z^2) \\ N_y &= \frac{\partial S}{\partial y} = \frac{yx}{x^2 + x_R^2} \\ N_z &= \frac{\partial S}{\partial z} = \frac{zx}{x^2 + x_R^2} \end{aligned} \tag{F.54}$$

The plane $x = 2x_R$ is chosen as initial surface at the vacuum-plasma interface, at which the beam is divergent. In this plane the index of refraction components are given by:

$$\begin{aligned} N_x &= 1 - \frac{3}{50}\frac{y^2 + z^2}{x_R^2} \\ N_y &= \frac{2}{5}\frac{y}{x_R} \\ N_y &= \frac{2}{5}\frac{z}{x_R} \end{aligned} \tag{F.55}$$

Moreover, the rays are intended as independent ones, and as a consequence the index of refraction has to be normalized to 1 in vacuum, after that the initial conditions of the refractive index are complete: $\mathbf{N}_0 = \mathbf{N}/|\mathbf{N}|$.

Figure F.3 shows some surfaces of trajectory points at equal step of integration (and therefore at equal $\tilde{S}$). These are perfectly perpendicular to the x direction as was expected.

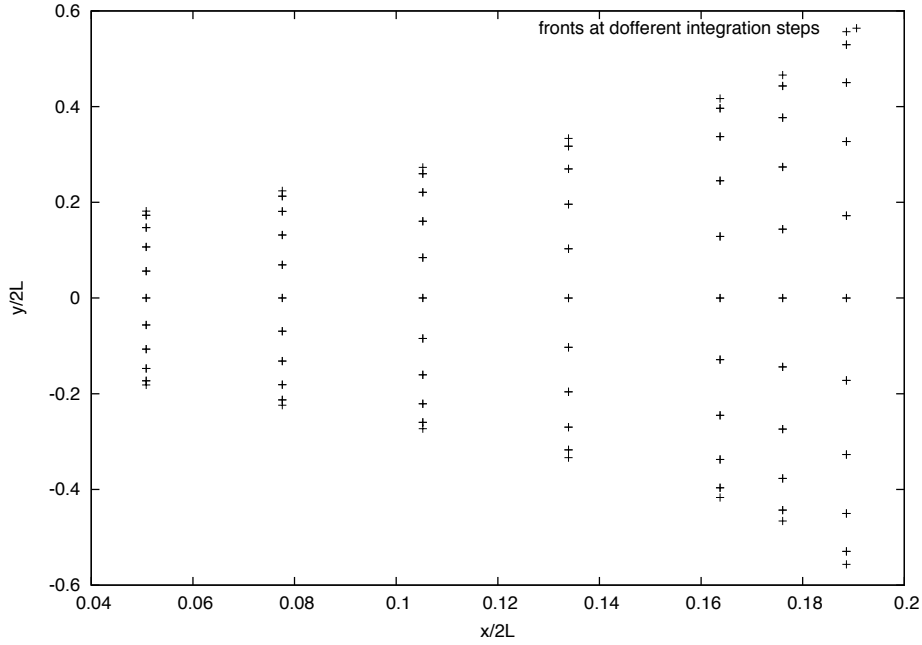

Figure F.3: Some $\tilde{S} = \text{constant}$ surfaces for $\tilde{S} = 1,\ 1.5,\ 2,\ 2.5,\ 3,\ 3.2,\ 3.4$.

Bibliography

[1] O. Maj, A. Mariani, E. Poli and D. Farina, "The wave energy flux of high frequency diffracting beams in complex geometrical optics," *Phys. Plasmas*, vol. 20, p. 042122, April 2013.

[2] W.D. D'haeseleer, W.N.G. Hitchon, J.D. Callen, J.L. Shohet, *Flux Coordinates and Magnetic Field Structure.* Springer-Verlag Berlin Heidelberg, 1991.

[3] R. Prater, "Heating and current drive by electron cyclotron waves," *Phys. Plasmas*, vol. 11, no. 5, p. 2349, 2004.

[4] M.A. Henderson et al., "Overview of the iter ec upper launcher," *Nuclear Fusion*, vol. 48, no. 5, p. 054013, 2008.

[5] E. Mazzucato, "Propagation of a gaussian beam in a nonhomogeneous plasma," *Physics of Fluids B*, vol. 1, p. 1855, September 1989.

[6] D. Farina, "A quasi-optical beam-tracing code for electron cyclotron absorption and current drive: Gray," *Fusion Science and Technology*, vol. 52, pp. 154–160, August 2007.

[7] E. Poli, A.G. Peeters, G.V. Pereverzev, "Torbeam, a beam tracing code for electron-cyclotron waves in tokamak plasmas," *Computer Physics Communications*, vol. 136, p. 90, May 2001.

[8] L. Demeio and F. Engelmann, "Velocity space diffusion of electrons induced by a beam of electron cyclotron waves of finite size i toroidal geometry," *Plasma Physics and Controlled Fusion*, vol. 28, no. 12A, p. 1866, 1986.

[9] G. V. Pereverzev, "Beam tracing in inhomogeneous anisotropic plasmas," *Phys. Plasmas*, vol. 5, p. 3529, October 1998.

[10] V. P. Maslov, *The Complex WKB Method for Nonlinear Equations I: Linear Theory*. Birkhauser, Basel, 1994.

[11] J. A. Arnaud and H. Kogelnik, "Gaussian light beams with general astigmatism," *Applied Optics Applied Optics Applied Optics*, vol. 8, p. 1687, 1969.

[12] G. Ramponi, D. Farina, M. A. Henderson, E. Poli, G. Saibene, and H. Zohm, "Iter ecrh-eccd system capabilities for extended physics applications," *Fusion Science and Technology*, vol. 52, no. 2, p. 193, 2007.

[13] G. Ramponi, D. Farina, M. Henderson, E. Poli, O. Sauter, G. Saibene, H. Zohm, and C. Zucca, "Physics analysis of the iter ecw system for optimized performance," *Nuclear Fusion*, vol. 48, no. 5, p. 054012, 2008.

[14] D. Farina and G. Ramponi, "Procedings of the fifteenth joint workshop on electron cyclotron emission and electron cyclotron resonance heating," p. 397, 2008.

[15] N. Bertelli, A.A. Balakin, E. Westerhof and M.N. Buyanova, "Eccd calculations in iter by means of the quasi-optical code," *Nuclear Fusion*, vol. 50, no. 11, p. 115008, 2010.

[16] A.A. Balakin, M.A. Balakina and E. Westerhof, "Ecrh power deposition from a quasi-optical point of view," *Nuclear Fusion*, vol. 48, no. 6, p. 065003, 2008.

[17] H. Zohm, G. Gantenbein, F. Leuterer, M. Maraschek, E. Poli, L. Urso and the ASDEX Upgrade Team, "Control of ntms by eccd on asdex upgrade in view of iter application," *Plasma Physics and Controlled Fusion*, vol. 49, no. 12B, p. B341, 2007.

[18] O. Sauter, M. A. Henderson, G. Ramponi, H. Zohm and C. Zucca, "On the requirements to control neoclassical tearing modes in burning plasmas," *Plasma Physics and Controlled Fusion*, vol. 52, no. 2, p. 025002, 2010.

[19] E. Poli, D. Farina, L. Figini, T. Goodman, O. Sauter, M. Cavinato, G. Saibene, M. Henderson, "Proceedings of the 40th eps conference on plasma physics (helsinki, finland)," vol. 37D, p. Paper P4.179, 2013.

[20] O. Svelto, *Principles of lasers*. Springer, 5th ed., 2010.

[21] S. N. Vlasov, V. I. Talanov, "The parabolic equation in the theory of wave propagation," *Radiophysics and Quantum Electronics*, vol. 38, no. 1-2, pp. 1–12, 1995.

[22] Littlejohn, Robert G. and Flynn, William G., "Geometric phases in the asymptotic theory of coupled wave equations," *Phys. Rev. A*, vol. 44, pp. 5239–5256, Oct 1991.

[23] J. D. Jackson, *Classical Electrodynamics*. John Wiley and Sons, Inc., New York, 3rd ed., 1999.

[24] L. Friedland and I. B. Bernstein, "Geometric optics in plasmas characterized by nonhermitian dielectric tensors," *Physical Review A*, vol. 22, p. 1680, October 1980.

[25] M. Bornatici, R. Cano, O. De Barbieri and F. Engelmann, "Electron cyclotron emission and absorption in fusion plasmas," *Nuclear Fusion*, vol. 23, no. 9, p. 1153, 1983.

[26] A.I. Akhiezer, I.A.Akhiezer, Polovin, Sitenko and Stepanov, *Plasma Electrodynamics Volume 1: Linear Theory*. Pergamon Press, 1975.

[27] D. Farina, "Relativistic dispersion relation of electron cyclotron waves," *Fusion Science and Technology*, vol. 53, p. 130, January 2008.

Acknowledgments

This thesis work has been carried out at the Istituto di Fisica del Plasma (IFP-CNR) in Milan, where I have been given the opportunity to participate to research activities of interest for the ITER project. I am grateful for this. I wish to thank my Supervisor Dott.ssa Daniela Farina (IFP-CNR), that followed my research path from master's thesis up to now, introducing me to fusion Plasma Physics and making me work within her research group, leaving me always enough time to continue my education. An acknowledgment goes to Dott. Omar Maj (Max-Planck-Institut für Plasmaphysik (IPP), Garching, Germany), without whom the major theoretical results of this thesis would not have been achieved, and whose friendly hospitality and useful discussions during the collaboration period spent at IPP made me make a leap in the understanding of a lot of aspects of the topics I was studying. I wish also to thank Prof. Emanuele Poli (IPP) for the hospitality and the time dedicated to my work. During all these four years spent at the IFP-CNR, I had precious support from Dott. Lorenzo Figini, who helped me constantly with his programming experience in dealing with the GRAY code and with everyday problems. I am also grateful to Prof. Roberto Pozzoli (Università degli Studi di Milano), my Supervisor during the master's thesis, that even after this role never stopped to be interested in my research activity, kindly helping me with useful advices in many cases. An acknowledgment goes also to my internal Supervisor Dott. Massimiliano Romé. Finally, I wish to thank my parents, my brother, Sara and all my friends, who shared with me these challenging years.